UNIVERSITY OF OKLAHOMA

GRADUATE COLLEGE

A DETAILED ANALYSIS OF RIFT RELATED STRUCTURES: INSIGHTS FROM LASER SCANNED CLAY MODELS AND 3-D SEISMIC INTERPRETATION

A DISSERTATION

SUBMITTED TO THE GRADUATE FACULTY

in partial fulfillment of the requirements for the

Degree of

DOCTOR OF PHILOSOPHY

By

DEBAPRIYA PAUL
Norman, Oklahoma
2014

A DETAILED ANALYSIS OF RIFT RELATED STRUCTURES: INSIGHTS FROM LASER SCANNED CLAY MODELS AND 3-D SEISMIC INTERPRETATION

A DISSERTATION APPROVED FOR THE
CONOCOPHILLIPS SCHOOL OF GEOLOGY AND GEOPHYSICS

BY

_____
Dr. Shankar Mitra, Chair

_____
Dr. Ze'ev Reches

_____
Dr. Kurt Marfurt

_____
Dr. May Yuan

_____
Dr. Raymon Brown

This work is dedicated to my family and closest friends

Preface

This dissertation presents the results of the original research work I have done in the Structural Geology laboratories at the ConocoPhillips School of Geology and Geophysics, University of Oklahoma. The focus of this research is to study the structural processes associated with extensional deformation especially rifting. The motivation for this research is mostly derived from the successful implementation of some novel experimental methodologies in basement-involved compressional and strike-slip deformation. The results of these earlier experimental models were published in American Association of Petroleum Geologist Bulletin in the years 2011 and 2013. The positive feedback from the reviewers and readers of these papers gave me the impetus to try similar methodologies for experimental models in extensional setting and compare the results with the findings from the studies of natural structures.

I am greatly indebted to my advisor, Dr. Shankar Mitra for providing the invaluable guidance, support and encouragement for this research. I am also thankful to Dr. Ze'ev Reches, Dr. Kurt Marfurt, Dr. May Yuan and Dr. Raymon Brown for their help and insights in improving the quality of the dissertation. I would like to thank Statoil and WesternGeco for the donation of the seismic data and also thank Bradley Wallet who made the availability of the data quicker. I am grateful to Landmark for providing the licenses of Lithotect, to Paradigm for providing the licenses for GoCAD and to Schlumberger for providing the licenses for Petrel. I would like to thank the staff at ConocoPhillips School of Geology and Geophysics, especially Donna Mullins, Nancy Leonard, Jocelyn Cook, Teresa Hackney and Adrianne Fox for the administrative support. A special thanks goes to Jody Bales Foote, librarian of the Youngblood Energy

Library for helping me with the references. I am also thankful to my fellow graduate students, Shamik Bose, Yuval Boneh, Supratik Sarkar, Jessica Treanton, Nabanita Gupta, Atish Roy, Preston Kerr, Roger Leavitt, Felipe Cardona, Roderick Perez, Thang Ha and David Tilghman for the numerous technical discussions that were valuable for this research.

My family is my greatest gift. I cannot thank enough my parents and my wife Paramita for providing me with the moral strength to go that extra mile for finishing my PhD. This dissertation would not have been possible for me to carry out without their constant emotional support and sacrifice.

Table of Contents

Topic **Page**

List of Figures

Chapter 3: Experimental models of transfer zones in rift systems

Chapter 4: Fault evolution and role of salt in decoupling extensional deformation in the Smørbukk area of the Halten Terrace, offshore Mid-Norway: Insights from 3-D seismic interpretation and structural restoration.

CHAPTER 1
INTRODUCTION

Rifting describes the process of crustal stretching through which the brittle upper crust is subjected to extensional deformation (Falvey, 1974; Bally and Snelson, 1980; Wernicke and Burchfiel, 1982; Steckler, 1985; McKenzie, 1987). It results in the development of basins associated with symmetric or asymmetric grabens or half grabens, bounded by listric or planar normal faults. Well known rift settings have been documented from the North Sea area, Gulf of Suez, East Africa, Basin and Range area etc. In a number of rift settings the normal faults are reactivated pre-existing weakness zones (ancient rifts or orogenic suture zones) within the crust. The crustal scale normal faults usually detach in a shear zone within the igneous/metamorphic basement or at the level of the brittle-ductile shear zone. The structural geometry and the shape of the extensional basins associated with these normal faults are influenced by mechanical stratigraphy, the spatial orientation of the faults with respect to the direction of extension and the interaction between two laterally propagating faults close to each other (Youssef, 1968; Stewart, 1971; Chapman et. al., 1978; Gibbs, 1984; Harding, 1984; Jackson and White, 1989; Bosworth, 1995). This study attempts to understand some of the structural features related to rift settings using analog clay experimental models and structural interpretation of a 3-D seismic dataset from the offshore Mid Norway area.

The analog experimental models focused on the geometries of faults and related fault-propagation (drape) folds, and their interference at different types of transfer zones. Detailed mapping and analysis of the orientations of secondary faults was conducted to investigate the structural controls of the resultant fault geometries and orientations. The

map geometries derived from the experimental models were compared with examples of natural structures from East Africa, the Gulf of Suez and the North Sea. The interpretation and detailed analysis of the 3-D seismic dataset from the offshore Mid Norway area helped in understanding the kinematic evolution of a rift related structure where a thick layer of mechanically weak salt is present between the basement and the cover sequence.

This dissertation is divided into three chapters, the first two of which focus on experimental models, whereas the third focuses on a seismic data set. The first chapter discusses experimental clay models to understand the evolution and nature of extensional fault propagation (drape) folds and secondary fault patterns associated with the movement on pre-existing basement faults. A suite of these basements faults (single fault and trapdoor structures) initially oriented at different angles with respect to the direction of extension was considered. A two layered model with stiff clay representing basement and soft clay representing cover sequence was used to take the rheological difference of basement and sedimentary units into consideration. In some setups, the basement fault initially terminated within the stiff clay to study the effect of lateral fault propagation. Relation between the fault density and width of the deformation zone within the drape folds and progressive evolution of the structural geometry was studied in detail. Natural examples from North Sea were considered to compare the results of the study.

The second chapter investigates the geometry, evolution and fault patterns associated with various kinds of basement fault interaction at transfer zones (convergent, divergent and synthetic). Basement faults with initial approaching, laterally offset and overlapping

geometries were also modeled. A similar two layered model with stiff clay and wet clay representing basement and cover sequence was used. The interference of fault-propagation folds associated with the faults was also studied. Analysis of fault orientation and 3-D surface modeling of clay was done in detail to study the progressive evolution of the secondary fault pattern and the structural geometry. The results of the study were compared with natural examples from East Africa and Gulf of Suez.

The third chapter involves a 3-D structural analysis of the Smørbukk area of the Halten Terrace, offshore Mid Norway using a 3-D seismic dataset and associated well tops donated by Statoil. The area has a thick sequence of Middle-Late Triassic evaporite interbedded with dolomite and anhydrite rich shale (collectively referred to as 'salt') that is stratigraphically located between the Permo-Triassic sedimentary basement and the Jurassic cover. The study includes 3-D seismic interpretation, displayed in both time and depth surfaces and time and depth sections. Restoration of units incorporating sequential restoration and decompaction on a series of depth sections was conducted to understand the evolution of the structures.

The present research involved several innovative approaches and techniques to produce original results that helped to improve the understanding of the broad field of basement involved extensional deformation. Some of these approaches and their advantages are discussed below.

a. Extensional structures involving drape folding on multiple basement-involved normal faults and complex fault transfer zones have been reported from several active rift settings. However experimental modeling of such structures in order to better understand their geometry and evolution was not attempted before. In

the present study a novel approach of choosing stiff clay over conventionally used steel ramps to model the basement helped to eliminate some of the mechanical limitations of the existing experimental models. The advantage of this setup was multifold. It helped to study the nature of extensional deformation both in the basement and cover units for single and multiple faults including the trapdoor structures. It also helped to understand the nature of extensional fault propagation folding and its effects on the lateral propagation of the basement faults and their mutual interactions.

b. Insights from previous experimental models were mostly restricted to the understanding of the sectional geometry of the extensional structures (Cloos, 1968; McClay and Ellis, 1987; Withjack et. al., 1990; Miller and Mitra, 2011). A relatively new 3-D laser scanning technology and surface modeling used in the present study helped to study the map geometry of the experimental structures and compare them easily with natural structures.

c. The case study from offshore Mid Norway involved faults detaching at different stratigraphic levels due to the presence of a weak salt layer. Similar structures were reported by previous workers in this area (Withjack et al, 1989; Pascoe et al., 1999; Richardson et al, 2005; Marsh et al., 2010). However decompaction and restoration of these structures were not attempted before. Such structural analyses used in the present study helped to provide insight about the fault evolution, the role of salt in partitioning the extensional deformation, and the conditions for the development of hard-linked or soft linked structures across the salt layer.

References

Bally, A.W. and S. Snelson, 1980, Realms of subsidence *in* Miall, A.D. eds. Facts and principles of world petroleum occurrence: Canadian Society of Petroleum Geologists Memoir.6, p.1-94.

Bosworth, W., 1995, A high-strain rift model for the southern Gulf of Suez (Egypt): Geological Society Special Publications, v. 80, p. 75-102.

Chapman, G. R., S. J. Lippard, and J.E. Martyn, 1978, The stratigraphy and structure of the Kamasia Range, Kenya Rift Valley: Journal of the Geological Society of London, v. 135, p. 265-281.

Cloos, E., 1968, Experimental analysis of Gulf Coast fracture patterns: American Association of Petroleum Geologists Bulletin, v.52, p. 420-444.

Emmons, W.H. and G.H. Garrey, 1910, General Geology *in* Ransome, F.L. et al. eds. Geology and Ore Deposits of the Bullfrog District: US Geological Survey Bulletin, v.407, p.19-89.

Falvey, D. A., 1974, The development of continental margins in plate tectonic theory: Australian Petroleum Exploration Association Journal, v.14, p.95-106.

Gibbs, A. D., 1983, Balanced cross-section from seismic sections in areas of extensional tectonics: Journal of Structural Geology, v. 5, no. 2, p. 153-160.

Harding, T. P., 1984, Graben hydrocarbon occurrences and structural style: American Association of Petroleum Geologists Bulletin, v. 68, no.3, p. 333-362.

Jackson, J. A., 1989, Normal faulting in upper continental crust: observations from regions of active extension: Journal of Structural Geology, v. 11, no. 1, p. 15-36.

Marsh, N., J. Imber, R. E. Holdsworth, P. Brockbank and P. Ringrose, 2010, The structural evolution of the Halten terrace, offshore Mid-Norway: extensional fault growth and strain localization in a multi-layer brittle-ductile system: Basin Research, v. 22, p. 195-214.

McClay, K., R. and P. G. Ellis, 1987, Geometries of extensional fault systems developed in model experiments: Geology, v. 15, p. 341-344.

McKenzie, D. P., 1978, Some remarks on the development of sedimentary basins: Earth and Planetary Science letters, v. 40, p. 25-32.

Miller J. F. and S. Mitra, 2011, Deformation and secondary faulting associated with basement-involved compressional and extensional structures: American Association of Petroleum Geologists Bulletin, v. 95. No.4, p. 675-689.

Pascoe, R., R. Hooper, K. Storhaug and H. Harper, 1999, Evolution of extensional styles at the southern termination of the Nordland Ridge, Mid-Norway: a response to variations in coupling above Triassic salt, *in* Fleet, A. J. and S. A. R. Boldy eds. Petroleum Geology of Northwestern Europe: Proceedings of the 5th Conference, v.5, p.83-90.

Richardson, N. J., J. R. Underhill and G. Lewis, 2005, The role of evaporite mobility in modifying subsidence patterns during normal fault growth and linkage, Halten Terrace, Mid-Norway: Basin Research, v.17, p.203-223.

Steckler, M. S., 1985, Uplift and extension at Gulf of Suez: indications of induced mantle convection: Nature, v. 317, no.12, p. 135-139.

Stewart, J. H., 1971, Basin and range Structure: A system of horsts and grabens produced by deep-seated extension: Geological Society of America Bulletin, v. 82, p. 1019-1044.

Thompson, G.A, 1960, Problem of late Cenozoic structure of the Basin Ranges: Proceedings 21st International Geological Congress, Copenhagen, v.18, p.62-68.

Wernicke, B. and B.C. Burchfiel, 1982, Modes of extensional tectonics: Journal of Structural Geology, v. 94, no. 2, p. 105-115.

Withjack, M. O., K. E. Meisling and L. R. Russel, 1989, Forced folding and basement-detached normal faulting in the Haltenbanken Area, Offshore Norway in Tankard. A. J. and H. R. Balkwill eds., American Association of Petroleum Geologists Memoir, v. 46, p. 567-575.

Withjack, M. O., J. Olson and E. Peterson, 1990, Experimental models of extensional forced folds: American Association of Petroleum Geologists Bulletin, v. 74, no. 7, p. 1038-1054.

Youssef, M. I., 1968, Structural pattern of Egypt and its interpretation: American Association of Petroleum Geologists Bulletin, v. 52, no. 4, p. 601-614.

CHAPTER 2
FAULT PATTERNS ASSOCIATED WITH EXTENSIONAL FAULT PROPAGATION (DRAPE) FOLDING

Abstract

Experimental models of extensional fault-propagation (drape) folds were used to study the evolution of the deformation zones and secondary fault patterns for single faults and trapdoor structures associated with two intersecting faults. Two-layer clay models, consisting of stiff and soft clay were used to model the deformation zones in the basement and sedimentary cover, respectively. Extension on single basement faults normal to the direction of extension results in the development of a deformation zone with expanding width, in which the fault density initially increases and then remains approximately constant. Extension on terminating faults results in conical drape folds with faults oblique to the fold axis along the propagating tip. Basement faults oblique to the direction of extension are characterized by oblique secondary faults along the boundaries of the deformation zone, which curve into a direction normal to the extension direction in the center.

Trapdoor fault geometries result in a triangular uplift with maximum relief at the apex. The difference in relief between the flanks and the apex is greatest in the case of propagating basement faults. En echelon secondary faults initiate on the flanks and extend into the apex area, curving into orientations that are closer to normal to the regional direction of extension. The width of the fault zone and the total fault length increase with increasing extension. The fault density initially increases and then remains approximately constant with increasing extension.

2.1 Introduction

Extensional fault–propagation folds, also known as drape folds, are recognized as a common type of structure in rift basins. The structures involve folding and secondary faulting within the sedimentary cover above basement-involved normal faults (Figure 2.1). The fault slip on the basement fault is dissipated within a triangular deformation zone, also referred to as a trishear zone (Erslev, 1991). Variations of the basic model have been developed and applied to both surface and subsurface structures. Numerous examples of drape folds have been documented from the North Sea, the Gulf of Suez, the Sirte basin, as well as from other basins. Deformation associated with drape folding has been modeled in cross-sectional view (Reches, 1978; Reches and Johnson, 1978; Withjack et al., 1990; Jin and Groshong, 2006; Miller and Mitra, 2011; Mitra and Miller, 2013).

Mapping of drape folds requires a better understanding of the three-dimensional geometry of drape folds and related secondary faults. The map patterns are dependent on the geometry of the faults associated with drape folds. Single faults are associated with plunging out of drape folds as the faults lose displacement along trend, and intersections of two sets of faults results in trapdoor structures. Both of these patterns are commonly observed in extensional terranes.

In this paper, the three-dimensional geometry and associated fault patterns for single faults and trap door structures using two-layer experimental models are studied. The results of the study provide insights on the geometry and fault patterns for surface and subsurface basement structures and can be used to analyze structures with limited data.

2.2 Previous Work on Experimental Fault Propagation Folds

A model of trishear fault-propagation folding for both contractional and extensional basement-involved structures was proposed by Erslev (1991), and applied primarily to Rocky Mountain foreland structures to explain the characteristic features of many structures in the area. According to the model, slip on basement faults is dissipated by oblique shear within an initially triangular zone in the sedimentary cover. The deformation occurs by folding and secondary faulting within the trishear zone. Reches and Johnson (1976) and Freund (1979) had earlier studied the dissipation of slip on a basement fault within a monoclonal flexure. Hardy and Ford (1997) and Allmendinger (1998) developed algorithms for the geometric and kinematic evolution of fault propagation folds, and also studied the variation in strain with structural position for these structures. Other models Erslev (1991) and Zehnder and Allmendinger (2000) suggested that in additional to homogeneous deformation, the trishear zone may be characterized by heterogeneous shear between fixed axial surfaces, resulting in the curved geometry of beds typically observed in trishear zones. Mitra and Mount (1998) and Mitra and Miller (2013) proposed that the heterogeneous shear may alternatively be explained by the expansion of the width of the trishear zone with progressive deformation, by incorporation of new material from the undeformed units on either side. Three dimensional models of fault-propagation folds have been proposed by Cristallini and Allmendinger (2001) and Cristallini et al (2004). A review of the geometry and kinematics of the trishear mechanism is provided in Hardy and Allmendinger (2011).

Broad folds related to normal faults, referred to as drape folds or forced folds (Stearns, 1978) had been documented previously, particularly in extensional provinces. For example, Harding (1984) showed a number of examples from the North Sea and Gulf of Suez. More recently, there have been a number of examples of drape folds described on the basis of both surface and subsurface data, particularly from the Gulf of Suez, the North Sea, and offshore mid Norway (Withjack et al., 1989; Sharp et al., 2000). Extensional fault-propagation folds have been modeled experimentally using clay models (Withjack et al., 1990; Mitra, 1993; Jin and Groshong, 2006; Miller and Mitra, 2011; Mitra and Miller, 2013). The models provide insight into the progressive evolution of the folds and related secondary faults. All of these models examined the evolution of the structures in profile view. However, additional information on the three-dimensional evolution and fault geometry for different basement fault geometries is necessary to interpret the structures.

This paper addresses the geometry and evolution of extensional fault-propagation folds (drape folds) using two-layer clay models, with stiff clay representing basement, and a soft clay representing the sedimentary cover. The evolution of the structures and secondary faults are studied for a variety of commonly observed fault geometries, including throughgoing or terminating faults and faults systems with trapdoor geometries.

2.3 Experimental Methodology

2.3.1 Experimental Setup

Experimental clay models were conducted using a motor driven apparatus consisting of two plexiglass backstops, one of which is fixed, while the other is

connected to two motors which control the rate of motion (Figure 2.2). The contrasting deformational behavior of the sedimentary cover and the basement was modeled by choosing stiff clay for the basement and soft clay for the cover units. The stiff clay has a density of 1.85 gm/cc and a thickness of 1.5 inch (3.8 cm) in the footwall block. The soft clay has a density of 1.6-1.65 gm/cc and a thickness of 1 inch (2.5cm). There is a significant contrast in strength between the stiff and soft clay which influences the nature of deformation of the structures, and results in drape folding.

This combination of materials for the basement/sedimentary cover package has been successfully applied to model strike-slip faults (Mitra and Paul, 2011), and basement-involved compressional and extensional structures (Paul and Mitra, 2012; 2013). The main advantages of using stiff clay instead of rigid metal or wooden blocks used in earlier models are: (1) the stiff clay can be cut to produce a variety of pre-existing fault geometries or discontinuities in the basement, including terminating faults; and (2) the stiff clay can deform in the vicinity of the main faults which is necessary to accommodate termination of faults and changes in fault geometry along trend and down dip.

Pre-existing cuts in the stiff clay were used to model basement normal faults which result in the propagation of faults through the stiff and wet clay to form drape folds. Basement faults were modeled with a dip of 60 degrees. Movement on the faults was initiated by movement of the movable plate, which caused the fault blocks to drop down along the preexisting fault cuts. The rate of extension was kept constant at about 0.0005cm/sec for all experiments.

2.3.2 Scaling of Experimental Models

The importance of using modeling materials that share geometric, kinematic and dynamic similarity with the natural analogs has been recognized and quantified by previous workers like Cloos (1929, 1930), Hubbert (1937) and Schilische and Withjack (2009). The strength of the upper crustal rocks usually increases with increasing depth and they obey the Mohr-Coulomb criterion for failure (Byerlee, 1978):

$$\sigma_s = C_0 + (\mu \sigma_n) = C_0 + [(\tan \varphi)\, \sigma_n] \quad (1)$$

where σ_s is the shear stress, σ_n is the normal stress, C_0 is the cohesive strength, μ is the coefficient of internal friction and φ is the angle of internal friction which controls the orientation of the fault planes with respect principal stresses. The Mohr-Coulomb criterion is also obeyed by wet clay (Richard and Krantz, 1991; Vendeville et al., 1995). Earlier workers like Handin (1966) and (Byerlee, 1978) have suggested that φ ranges from 29° to 40° in case of natural rocks and 30° in case of wet clay (Schilische and Withjack, 2009). C_0 for water based wet clay (40% water by weight) is approximately 50 Pa while C_0 for natural sedimentary rocks is approximately 5 MPa. Approximate density of the wet clay used in the experimental models is 1.6-1.65gm/cc while the average density of the sedimentary cover units is 2.6gm/cc. Geometric and dynamic similarity between the modeling materials and the natural analogs requires that

$$C_0^* = p^* g^* L^* \quad (2)$$

where C_0^*, p^*, g^* and L^* are the model-to-natural analog ratios for cohesive strength, density, gravitational acceleration and length. Putting appropriate values in Equation (2) ($g^* = 1$), L^* is approximately 10^{-5} which suggests that a centimeter on the model represents a kilometer in real world structures. The approximate cover rock-to-basement

rock ratio of densities is 0.89 (considering the average density of igneous/metamorphic rocks to be 2.9gm/cc; Attewell and Farmer, 1976) which is the same for wet clay-stiff clay pair and higher for wet clay-aluminum pair (0.6). Stiff clay also has a significantly less cohesive strength than aluminum blocks and can undergo some degree of penetrative deformation which is observed in the basement rocks under extensional deformation (Fossen, 1992). Stiff clay is thus chosen over steel ramps as a better candidate for modeling the basement.

It should be noted that for all the experimental models a uniform homogeneity of mechanical properties for both the basement and the cover units is assumed. The models are designed to represent structural geometries in a regional scale and heterogeneities induced by stratigraphic rheology or pre-existing complex structural fabric or changes in the stress direction have not been taken into account. In natural settings the cover sequence is expected to have multiple stratigraphic layers which will control the structural geometry. Small scale local structures may originate from such mechanical heterogeneities and these are not represented in the experimental models.

2.3.3 Experimental Configurations

Drape folds associated with a number of fault configurations were investigated. These included: (1) Single faults which were either throughgoing, or terminated at one or both ends (Figure 2.2a). Terminating faults were modeled to study development of folds and related faults at fault terminations. Faults orthogonal and oblique (75 and 60 degrees) to the direction of extension were studied; (2) Trap door geometries involving intersecting fault sets (Figure 2.2b). Fault with intersecting angles of 90, 120, and 140 degrees were modeled. The difference between terminating and through going faults

was also studied. A summary of all the basement configurations studied is summarized in Figure 2.3.

For all of experiments, pre-existing cuts in the stiff clay provided the discontinuities along which the faults propagated both laterally, as well as upward through the soft clay, where they developed secondary fault splays. The stiff clay representing the basement was cut thinner in the hanging wall blocks to allow these blocks to drop down along the faults (Figure 2.2).

2.4 Data Analysis

Data analysis was conducted on two datasets: (1) fault data that were digitized and extracted from photographs taken at regular intervals during the experiments, and (2) scanned elevations of the top of the soft clay, obtained as point clouds, which were used to develop 3-D models of the surface.

2.4.1 Fault Patterns and Orientations

Photographs taken at approximately two minute intervals during the experiment were used for the analysis of the variation of orientation of the faults. Fault patterns were analyzed for different stages of formation of the structures and displayed in Rose diagrams documenting the map trends (strikes) of the secondary faults.

2.4.2 Fault Densities and Trishear Width

Variations in fault densities and the width of the trishear zone with progressive deformation were analyzed for selected experiments of both single and trapdoor basement fault geometries to understand the evolution of secondary faults. The fault density (Di) was defined by the total length of all faults per unit area at each stage (Figure 2.4), so that

Di-= Total length of all faults in selected area/ Instantaneous Area (3)

To analyze the variation in density along the structure, an additional measurement was made by determining the moving average value of the total length of all faults within circles of constant radius of 0.3 cm with centers 0.02 cm apart. The mean of this moving average value (Dm) was determined to compare with the value of Di for each setting.

An additional parameter of fault density measured was the summed lengths of all faults divided by the faulted area in the final stage (Df). The purpose of using this parameter is to study the increase in fault densities for the final trishear zone during its evolution. The width of the fault zone (W) was measured at right angle to the trend of the major faults to compare with the fault density values.

2.4.3 3-D Surface Analysis

Laser-scanned point sets were used to build contoured and gridded surfaces. The horizontal and vertical resolution of the point sets was 75 DPI (~0.015 inches point density). This enabled mapping of faults with a minimum vertical separation of 0.2 mm. The modeled surfaces were compared with the photographs to incorporate the detailed geometry of the fault surfaces. Major faults and many minor faults were mapped and cut out on the surfaces, but some of the smaller faults were not mapped because of resolution limitations. The faults and faulted surfaces were then smoothed before contouring the surfaces to determine the final topology. This approach enabled the surfaces to be correctly contoured incorporating all major and many secondary faults. The contour interval used for all the surfaces was 2 mm. Changes in the surface geometry were used to study the evolution of the structures and related faults.

Because the original surface of the top clay had some relief for all experiments, all deformed surfaces were corrected to observe their geometry for an originally flat surface. This was accomplished by first developing a difference surface between the original surface topology and a horizontal surface the level of which was at the mean value of the elevations of all the points on the original surface. This difference was applied as a correction to all deformed surfaces, after stretching the difference surface to the length of the deformed surface in question (Figure 2.5). The operation applied to stretch the difference surface was (Figure 2.5a):

$$Yf = Yi + (Yi - Yo)*e, \quad (4)$$

Where the extensional strain $e = \Delta L/Lo$, Yi and Yf are the original and final Y-coordinate of any point, respectively, and Yo is the original y-coordinate for the fixed boundary.

All displayed figures representing the deformed surfaces for the top of the soft clay are the corrected surfaces.

2.5 Experimental Results: Single Faults

Drape folds associated with single faults were modeled for basement faults that were throughgoing, terminating at one end and terminating at both ends, and orthogonal to the direction of extension. The reference frame used to describe the structures and fault orientations for this and other structures is that north represents the top of the experimental setup.

2.5.1 Single Faults Normal to Extension Direction

Extension on a throughgoing fault resulted in a broad and slightly asymmetric drape fold and a series of secondary faults, a number of which cut the top surface of the

clay (Figure 2.6a). Increasing extension resulted in the lateral propagation of the faults, larger throws on individual faults, and the development of new faults, so that the zone of faulting widened (Figure 2.6b). This is consistent with a model of increasing width and shearing within the triangular or trishear zone (Erslev, 1991) with progressive deformation (Mitra and Mount, 1998; Mitra and Miller, 2013). Linkage of faults also resulted in concentration of slip on a few major faults (Figures 2.6c and 2.7a). The mean orientation of secondary faults was approximately parallel to the trend of the basement fault (Figure 2.6). The top of the soft clay exhibits a downwarp in the footwall, and an upturned hanging wall, resulting from the breakthrough of faults through the trishear zone.

A basement fault that terminated in the center of the model resulted in a plunging drape fold which terminated on the east side, and had larger displacement on the western end (Figure 2.8). The main fault also curved in the direction of dip near its termination. Secondary faults developed an echelon pattern, and were curved in the same direction as the contours around the plunging nose of the structure (Figure 2.8 and 2.9). This resulted from the local reorientation of the stresses due to the oblique dip of the deformed surface. The final rose diagram shows a mean orientation of the faults trending 104 degrees, oblique to the direction of extension. Some of the large displacement secondary faults were connected by cross faults oriented oblique to both the direction of extension and the main fault zone.

For a fault terminating in both directions, the experiment resulted in a more rapid propagation of the fault to the east resulting in an asymmetric drape fold plunging to the west. The faults were generally normal to the direction of the extension, but curved to

an oblique orientation around the plunging nose. The final rose diagram displayed a mean trend parallel to the fault cut, with a number of oblique faults symmetrically distributed on both sides (Figure 2.10a).

2.5.2 Single Faults Oblique to Extension Direction

Throughgoing basement faults oriented 75 and 60 degrees to the direction of extension were modeled. A gently plunging drape fold developed with the fold axis trending approximately parallel to the basement fault cut (Figure 2.11). The fold plunged out on the edge that was located further from the moving plate. The zone of secondary faults was generally parallel to the pre-existing fault cut. However, the orientations of the individual faults exhibited a more complex pattern. The bounding faults formed above the footwall and hanging wall cutoffs of basement were approximately parallel to the pre-existing fault cut. On the other hand, the faults formed between these two boundaries curved into a direction that was approximately normal to the direction of extension (Figures 2.11b and 2.7b). Because of the obliquity of the direction of extension to the basement fault, many of these faults were significantly rotated with surface dips opposite to the direction of the main fault. This effect was most prominent in the faults with a 60 degree orientation to the direction of extension (Figure 2.11). Furthermore, although the faults with significant displacement were synthetic, many of the secondary faults were antithetic to the main fault, with the percentage of antithetic faults increasing from the 90 degree to the 60 degree case (Figure 2.12). The final rose diagram showed a mean trend that was intermediate between the original trend of the basement fault and the normal to the direction of

extension. For the 75 degree fault cut, the mean trend was 83 degrees, whereas for the 60 degree fault cut, the mean trend was 77 degrees (Figure 2.12).

For basement faults terminating in the center of the model (Figure 2.13), an oblique drape fold trending approximately parallel to the fault and plunging out to the east developed for both the 75 degree and 60 degree cases. Secondary faults formed along the flank of the drape fold curved strongly in the direction of the fault dip. For the 75 degree case the mean trend of the secondary faults was 102 degrees or 27 degrees from the basement fault trend whereas for the 60 degree case the mean trend of the secondary faults was 93 degrees, 33 degrees from the basement fault trend.

Fault cuts in the middle of the section (Figure 2.10 b and c) showed a similar pattern of secondary faults as that for the throughgoing faults (Figure 2.10a), except that the fault zones terminated in both directions along trend and that the faults curved in the direction of the fault dip close to the original fault termination in the basement. The bounding faults were again approximately parallel to the original fault cut, whereas the remaining faults were approximately normal to the direction of extension.

2.5.3 Fault Densities for Single Faults

Density and width plots for different stages of extension provide some insight on the evolution of secondary faults within the deformation zone. Continuous density plots for a throughgoing fault orthogonal to the direction of extension showed that the mean density (Dm) increased sharply in the initial stages and then remained approximately constant or showed a small decrease in the late stages (Figure 2.14a). A similar pattern was observed for the density measured per unit instantaneous area for the entire fault zone (Di). The sharp increase in density in the early stages occurred by an increase in

the lengths of individual faults as well as by the formation of new faults. The constant density or decrease in the late stage is related to the fact that the width of the deformation zone also increased, sometimes at a higher rate than the total fault length. The density measured relative to the final fault width (Df) increased through all the stages (Figure 2.14a). The continuous density plots showed areas of local high densities (Figure 2.15a), typically located in the center of the fault zone. A major basement fault trending at an angle of 60 degrees to the direction of extension showed a fairly similar pattern of fault densities and widths (Figures 2.14 c and d), except that the continuous density plots showed bands of high densities oblique to the trend of the fault zone (Figure 2.15b).

Major faults that propagate from an initially terminating fault in the stiff clay involve the propagation of the fault zone both normal to and in the direction of propagation of the major fault. Hence the fault densities Di and Dm drop significantly after an initial rise and then rise again (Figure 2.14e). The drop in the fault density probably represents a significant rise in the rate of lateral propagation, so that the increase in the fault length does not keep pace with the rate of area increase. The width of the fault zone and the density measured with respect to the final areas (Df) both increase with increasing extension (Figure 2.14e and f). The continuous density plot (Figure 2.15c) shows bands of high densities oblique to the main fault. These bands probably represent distinct episodes of lateral fault propagation.

2.6 Experimental Results: Trapdoor Fault Geometries

Trapdoor geometries result from intersections between two or more fault sets, which may either have formed simultaneously under a three-dimensional strain field

(Sagy et al., 2003), or at different times, with a change in the orientation of the maximum extension direction over time. The Heather and Ninian structures (Figure 2.16) from the Viking graben (Gray and Barnes, 1981; Harding, 1984) show that the angle between two intersections can vary considerably, resulting in structures ranging between angular trapdoors and broad warps. Therefore, models for trapdoor geometries included through going fault sets with intersecting angles of 90, 120, and 140 degrees, to cover a wide range of observed structural geometries. In addition, terminating fault sets were also modeled to study the effects of lateral fault propagation on trapdoor geometries.

2.6.1 120 degree Fault Intersections

Two faults with dips of 60 degrees and a map intersection angle of 120 degrees were cut in the stiff clay representing basement, with the cuts distributed symmetrically with respect to the direction of extension. The two faults dipped away from each other, so that the hanging wall block contained the larger angle between the faults. The modeled 3-D surfaces were tilted by 5 degrees in a direction opposite to the fault dip so that the final structures resembled the trapdoor geometries found in tilt-blocks.

Two experimental set ups were used: the first with two connecting faults in the stiff clay, and the second with the both preexisting faults terminating towards the center so that the central one-third of the area does not have any initial fault cuts. The purpose of the second experiment was to study the difference in geometry of the drape fold and the related secondary faults when the basement faults propagate and eventually intersect. For two connected basement faults, initial extension resulted in a triangular horst block in the tilted footwall block. The contours on the flanks of the structures are at a low

angle to the normal to the direction of extension (Figure 2.17a). Two sets of incipient faults with mean trends of 70 and 101 degrees develop on the flanks, but few faults initially developed in the apex area.

With increasing extension, the faults propagated laterally as en echelon and overlapping segments with relay ramps sloping away from the apex separating them (Figure 2.17b and c). The throw on the individual faults as well as the number of faults increased with increasing extension.

Furthermore, the width of the fault zone on the flanks expanded from 1 cm at an extension of 0.27 cm to 2.2 cm at an extension of 0.97 cm (Figure 2.18). The density of the faults (Di and Dm) first increased and then decreased, whereas Df increased with extension. Generally, the densities were a little lower in the apex compared to the flanks in the early stages of extension. The expansion of the fault zone on the flanks results from both the lateral propagation of pre-existing faults, as well as the nucleation of new faults. The lower fault densities in the apex in the early stages result from the fact that the faults initiate on both flanks and then propagate and connect near the apex area.

The final mean trends of the faults on the flanks were 74 and 103 degrees, so that the faults make a higher angle to the direction of extension than the original major fault cuts. There was a progressive transfer of slip to the frontal en echelon faults from the flanks to the apex. In the apex area, the faults curved into an orientation approximately normal to the direction of extension, with a mean trend of 79 degrees.

The throw on the major fault in the stiff clay and the cumulative throw of the secondary faults in the soft clay is greatest on the flanks and decreases in the apex area, so that the maximum turn up of hanging wall block is in the apex area (Figure 2.17c).

120 degree trapdoor structures involving propagating faults show some important differences (Figure 2.19). First, the deformation zone is wider and has a shallower dip. The upturn in the hanging wall is also more prominent. Second, the faults in the apex are less influenced by the pre-existing cuts, so that there is a broader zone of faults trending perpendicular to the direction of extension. The faults in the flanks curve gradually into the trend of the faults in the apex zone. As a result, the trapdoor configuration of the basement fault is not as visible in the overlying units, which shows a broad convex structural geometry. The final mean trends of faults in the flanks are 71 and 104 degrees, whereas the apex area shows a mean trend of 83 degrees. Density plots (Figure 2.20) show distinct plots for the flanks and apex. The flanks show an initial sharp increase in density followed by a later period of small density increase or decrease, whereas the apex area show a larger change in density in the later stages as the basement faults propagate and connect up.

2.6.2 90 degree and 140 degree Fault Intersections

The experiments were repeated with 90 degree and 140 degree fault intersections (Figure 2.21). The results of the 90 degree experiment with the connecting faults (Figure 2.21a) was very similar to the 120 degree experiment (Figure 2.21b), the main differences being in the geometry of the structure, and the orientations of the fault zones and individual faults. The drape fold shows a more angular geometry, with a smaller interlimb angle than in the 120 degree case. The hanging wall shows a larger turn up at the apex of the structure than on the flanks. Also the fault zone and the individual faults on the flanks are at a larger angle to the extension direction and curve more sharply into an orientation close to perpendicular to the direction of extension.

The final mean trends of the faults on the flanks are 59 and 125 degrees, whereas the apical area shows a mean trend of 85 degrees.

The en echelon geometry of the faults is more apparent for this configuration, with the progressive transfer of slip to the frontal part of the fault zone in the apex area. Overlapping segments are marked by relay ramps sloping away from the apex (Figure 2.22). Some transfer faults with large strike-slope components connect some of the en echelon faults.

Throughgoing faults with a 140 degree intersection show an even broader structure than the 120 degree trapdoor, with a gradual trend in strike, so that the trapdoor geometry is not readily apparent from the map geometry (Figure 2.21c). The footwall elevation shows very little variation in relief compared to the 90 degree and 120 degree intersections, and the overall relief of the footwall block is less. At the maximum extension of 1.0 cm, the secondary faults on the two flanks have mean trends at 79 and 102 degrees so that the angle between them is 157 degrees. The apical area has a mean fault trend of 88 degrees.

Fault densities for the (Di) and the mean fault densities (Dm) show a rapid initial increase followed by a constant or decreasing density for the 90-degree trapdoor structures (Figure 2.23). The pattern is quite similar to the 120 degree case. The density relative to the final deformation zone (Df) and the width of the deformation zone both increase progressively over time.

Comparison of the two flanks of the trapdoor and the apex for the 90 degree trapdoor shows that the densities Di and Dm both increase more rapidly on the flanks than in the apex in the initial stages. However, in the later stages the apex area shows about the

same density as the flanks. This is consistent with the observation that the faults initially develop on the flanks and propagate and connect in the apex area in the later stages of deformation.

2.7 Discussions and Conclusions

Extension on single basement faults results in the development of a trishear zone made up of secondary normal faults. If the basement fault is normal to the direction of extension, the secondary fault zone and the individual faults are also normal to the direction of extension. With increasing extension, the faults propagate laterally and many of them connect to form anastomosing fault zones, and new faults also develop. The total fault length increase with time, but this is accompanied by an increase in the width of the deformation zone. As a result, the fault density initially increases with increasing extension, but remains constant or even decreases in the late stages, when the deformation is focused on fewer faults which breakthrough the entire cover. These observations are consistent with the model of an expanding trishear zone, with maximum deformation in the center of the deformation zone (Mitra and Mount, 1998; Mitra and Miller, 2013). Basement faults oblique to the direction of extension show a similar pattern as the above, except that the trend of the secondary faults are similar to that of the main fault at the boundaries of the deformation zone, but curve into an orientation that is close to perpendicular to the direction of extension in the center. Therefore the amount of curvature of these oblique secondary faults is dependent on the obliquity of the underlying basement fault with respect to the direction of extension. Conversely, more tightly curved secondary faults reflect a greater degree of obliquity of

the underlying basement fault. Oblique faults are also characterized by a significant number of antithetic faults and rotated faults.

Terminating basement faults exhibit a variation in fault slip along trend, resulting in rotational deformation on the fault. The main fault curves in the dip direction and the drape fold exhibits a conical termination along trend. The area of secondary faulting increases both normal to the fault and in the direction of propagation with increasing extension. Secondary faults are generally oblique to main fault on the steep limb of the drape fold. The fault density shows discrete highs along trend suggesting episodic lateral propagation on the fault.

Triangular uplift zones within cover units with maximum relief at the apex are indicative of underlying basement faults that have a trapdoor geometry. The hanging wall is also typically higher in the apex compared to the flanks, especially for fault systems with lower intersecting angles, and in the case of propagating basement faults. The secondary faults initiate on the flanks and extend into the apex area, curving into orientations that are closer to normal to the regional direction of extension. On the flanks, the faults exhibit an en echelon pattern with a transfer of slip to frontal faults from the flanks to the apex. Transfer zones between en echelon faults are sometimes marked by strike-slip faults, which transfer slip to the frontal faults.

The trends of the secondary faults broadly mimic that of the basement faults. However they always trend intermediate between the trend of the basement faults and the normal to the direction of the extension. This is partly due to the fact that the faults originally develop slightly oblique to the basement faults because of the oblique extension, and partly due to their rotation with progressive deformation. The obliquity of the secondary

faults is indicative of the angle of intersection of the underlying basement faults. The secondary faults also curve into the apex zone where they are close to normal to the direction of extension. Fault intersections at high angles (140 degrees) result in only a broad curvature in the trend of the secondary faults, so that the presence of an underlying trapdoor geometry is not readily apparent from the shape of the surface structure.

As in the case of single faults, the width of the fault zone and the total fault length increase with progressive deformation. The fault densities initially increase and then remain approximately constant with increasing extension, although the density measured with respect to the final area of the deformation zone increases. Because of the progressive transfer of deformation from the flanks to the apex, the fault density and the width of the transfer zone are both lower near the apex than on the flanks in the initial stages of deformation.

Figures

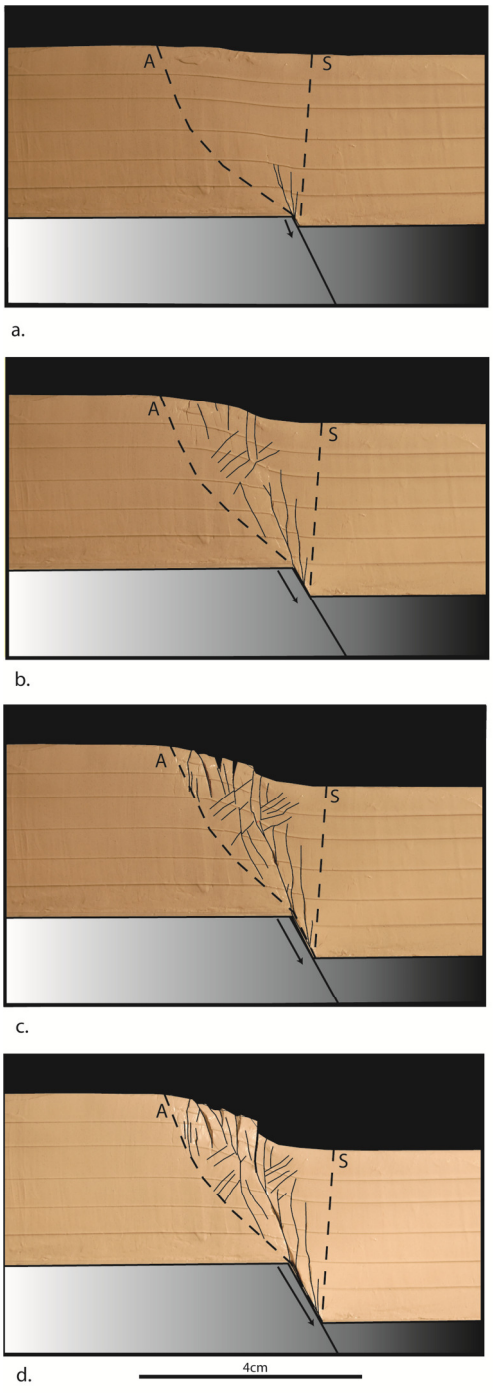

Figure 2.1 Experimental model of the progressive evolution of an extensional fault-propagation fold (drape fold) related to a basement fault dipping 60 degrees in profile view. The basement slip is dissipated within the trishear zone bounded by the anticlinal (A) and synclinal (S) axial surfaces. The positions of A and S shown are the final positions at the end of the experiment. Modified from Miller and Mitra (2011).

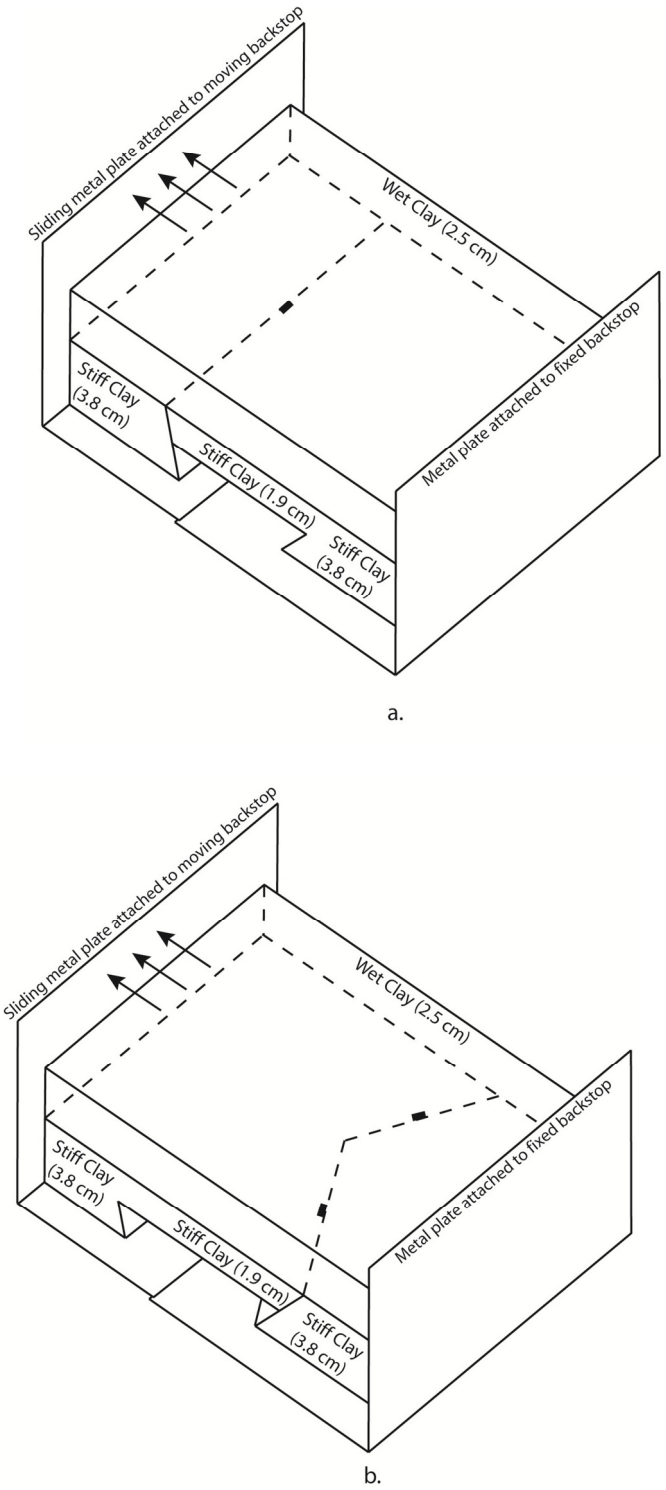

Figure 2.2 Experimental setup showing the configuration of the base plates, the moving and fixed backstops, and the stiff and soft clay, which represent the basement and overlying sedimentary cover. Pre-existing cuts in the stiff clay represent preexisting basement faults which propagate both laterally and upwards through the soft clay with extension. a. Single faults. b. Trapdoors consisting of two intersecting faults.

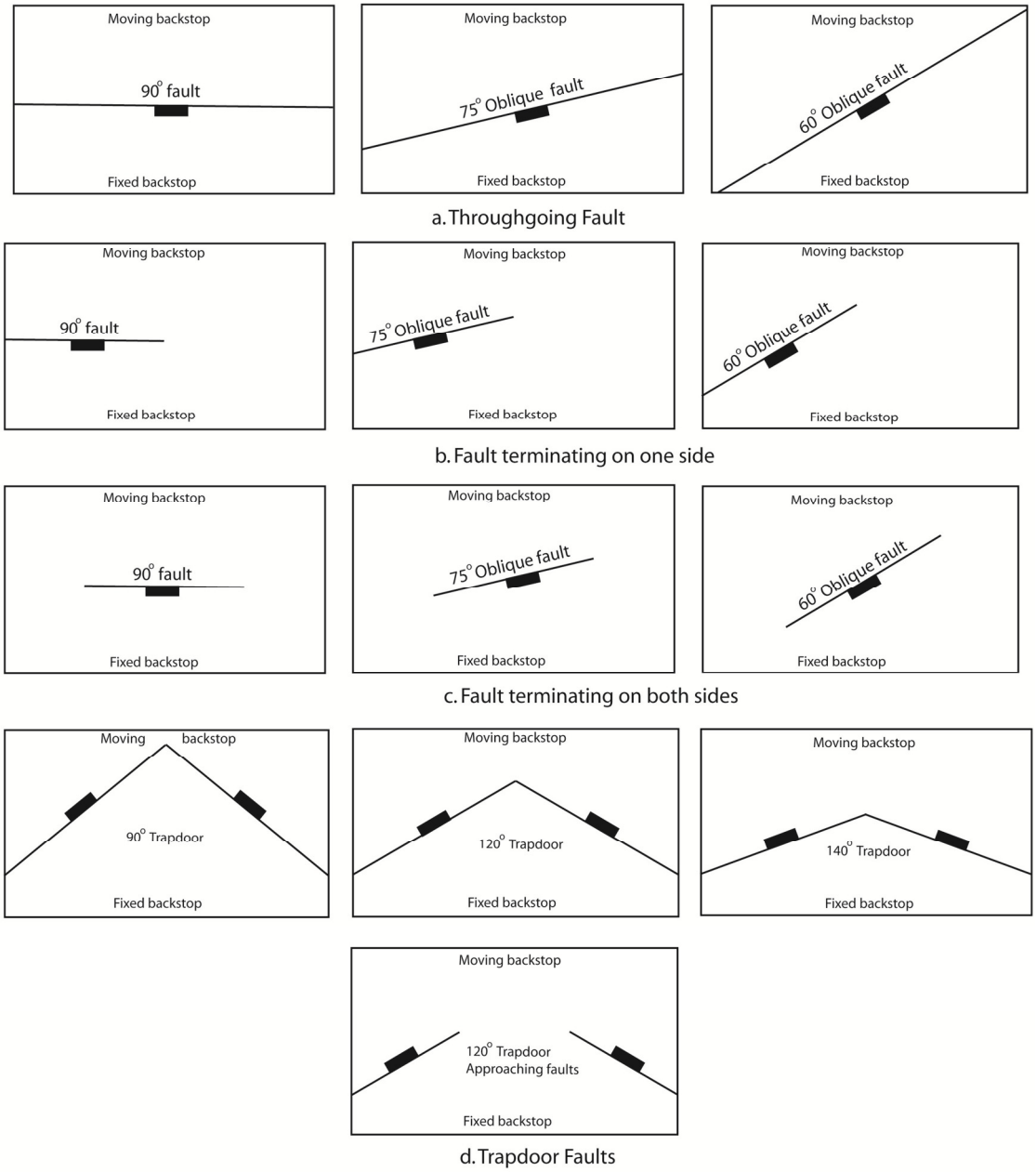

Figure 2.3 Summary of map views of experiments with initial basement fault configurations. Single faults modeled included through going and terminating faults, and faults orthogonal and oblique to the direction of extension. Trapdoor geometries with different intersecting angles, and with connecting or propagating faults were modeled.

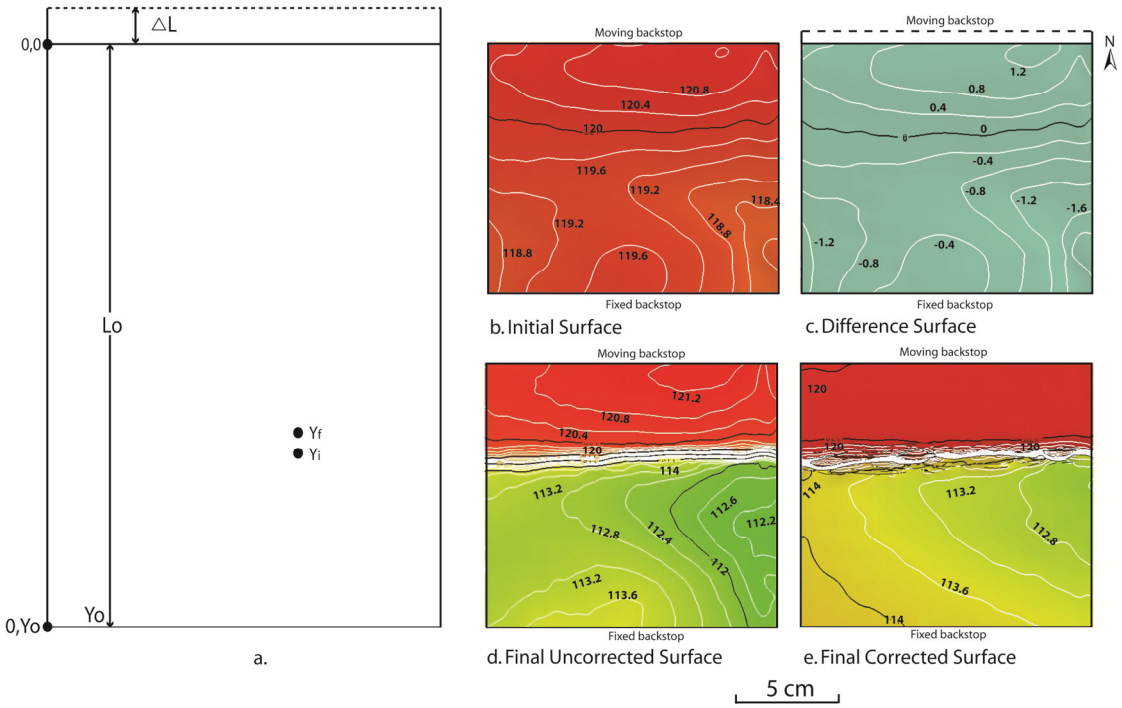

Figure 2.4 Method of surface correction to eliminate initial topography of top surface. a. Basic method (see text for explanation). b. Initial uncorrected surface. c. Difference surface used to flatten final surface. d. Uncorrected deformed surface. e. Corrected deformed surface.

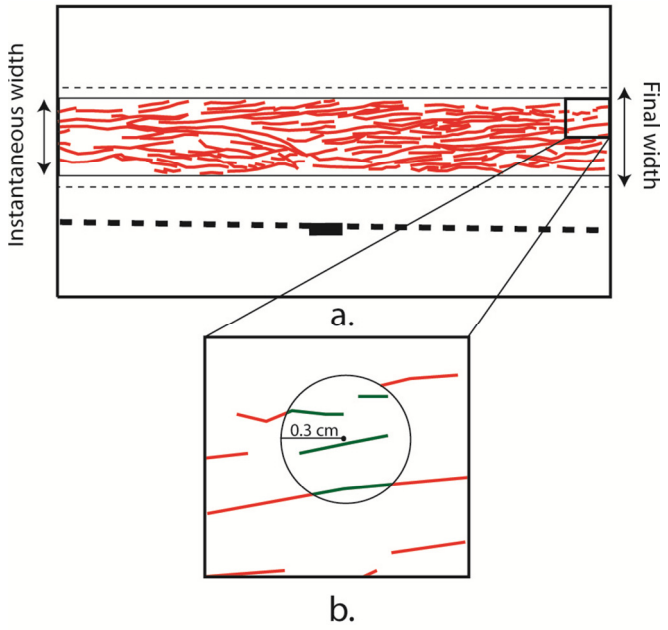

Figure 2.5 Parameters used to calculated different density types (Di, Df, and Dm) and width of the fault zones.

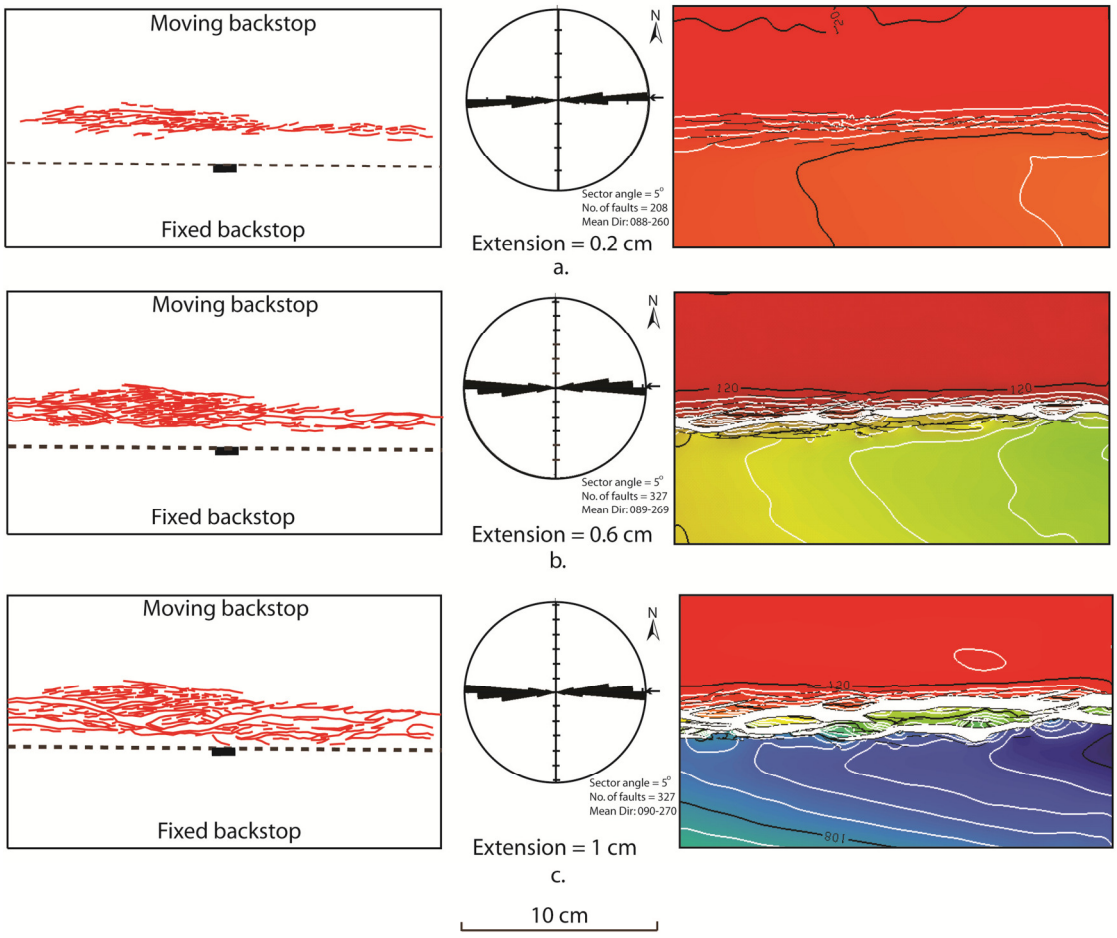

Figure 2.6 Evolution of structural geometries and fault patterns in map view for a trishear zone associated with a throughgoing basement fault normal to the extension direction. Moving plate is towards the north. The contoured and gridded structure map, fault patterns and fault orientations for the top of the soft clay, are shown for each stage of deformation. Extension is 0.2 cm (a), 0.6 cm (b), and 1.0cm (c). Rose diagrams show main orientations of faults measured. Bars show percentage of total length of faults for each orientation. For this and other similar figures showing experimental results, an arbitrary north arrow is assigned as a reference to describe orientations of faults. On the contoured structure map, red and yellow indicate high elevations and blue and green represent low elevations. Synthetic faults are shown in red, and antithetic faults and rotated synthetic faults which dip opposite to the main fault are shown in blue.

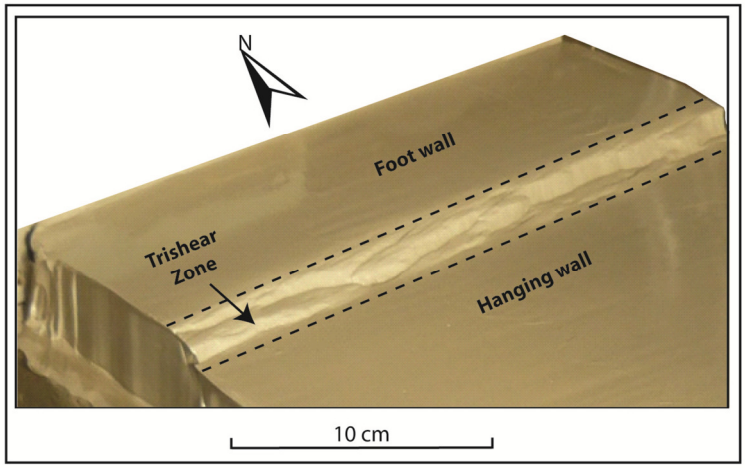

a. 90° Throughgoing Fault

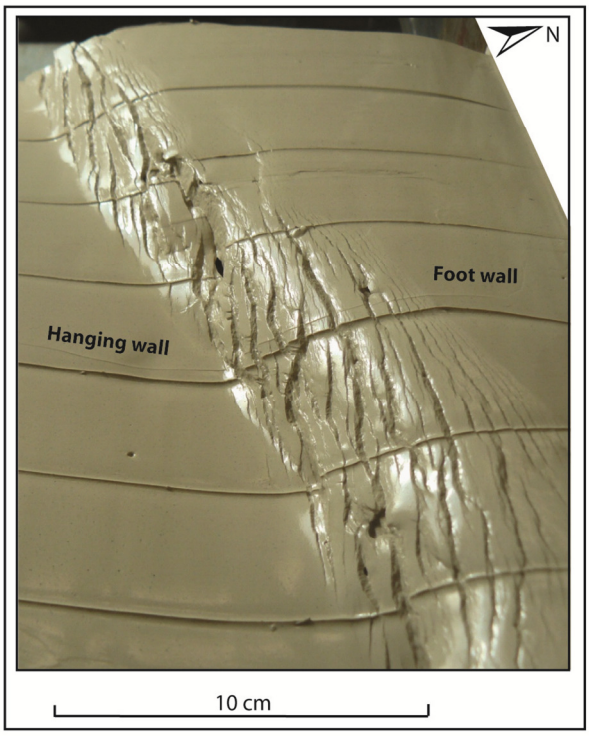

b. 60° Oblique Throughgoing Fault

Figure 2.7 Oblique photographs showing secondary faults at the top of the soft clay for a throughgoing basement fault. a. Basement fault at 90 degrees to the direction of extension. Fault zone is made up of approximately parallel, overlapping and anastomosing individual faults. b. Basement fault at 60 degrees to the extension direction. Faults curve into an orientation normal to the direction of extension and many of them curve significantly to dip opposite to the main fault.

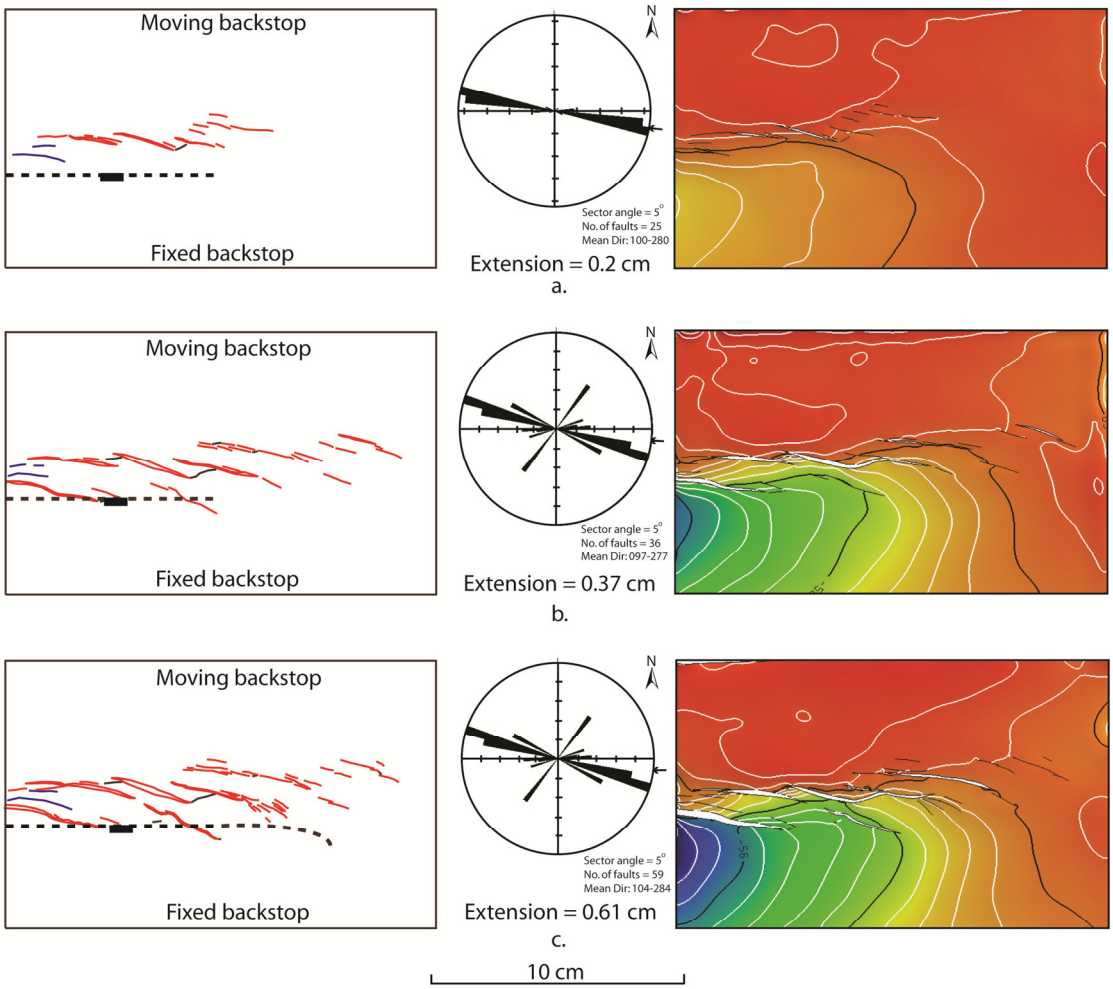

Figure 2.8 Evolution of structural geometries and fault patterns in map view for a basement fault normal to the extension direction, and terminating in the middle. The contoured and gridded structure map, fault patterns and fault orientations for the top of the soft clay, are shown for each stage of deformation. Extension is 0.2 cm (a), 0.37 cm (b), and 0. 61 cm (c). Rose diagrams show main orientations of faults measured. Bars show percentage of total length of faults for each orientation. Initial basement fault geometry is shown in a and b, and the final curved final geometry is shown in c.

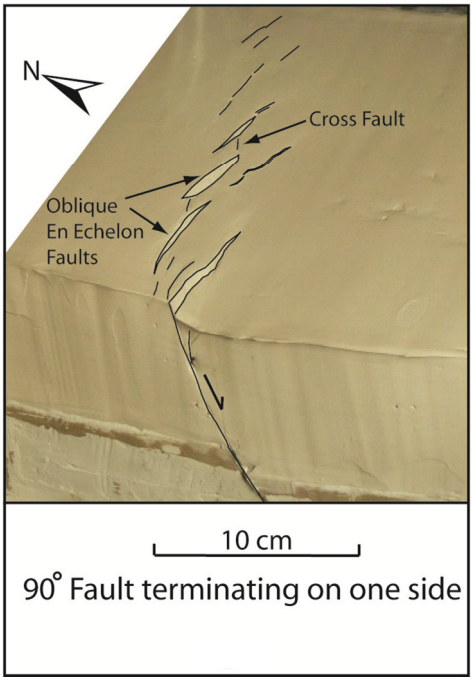

Figure 2.9 Oblique photograph showing secondary faults at the top of the soft clay for a terminating basement fault. Faults show an echelon pattern with trends that are oblique to the main fault.

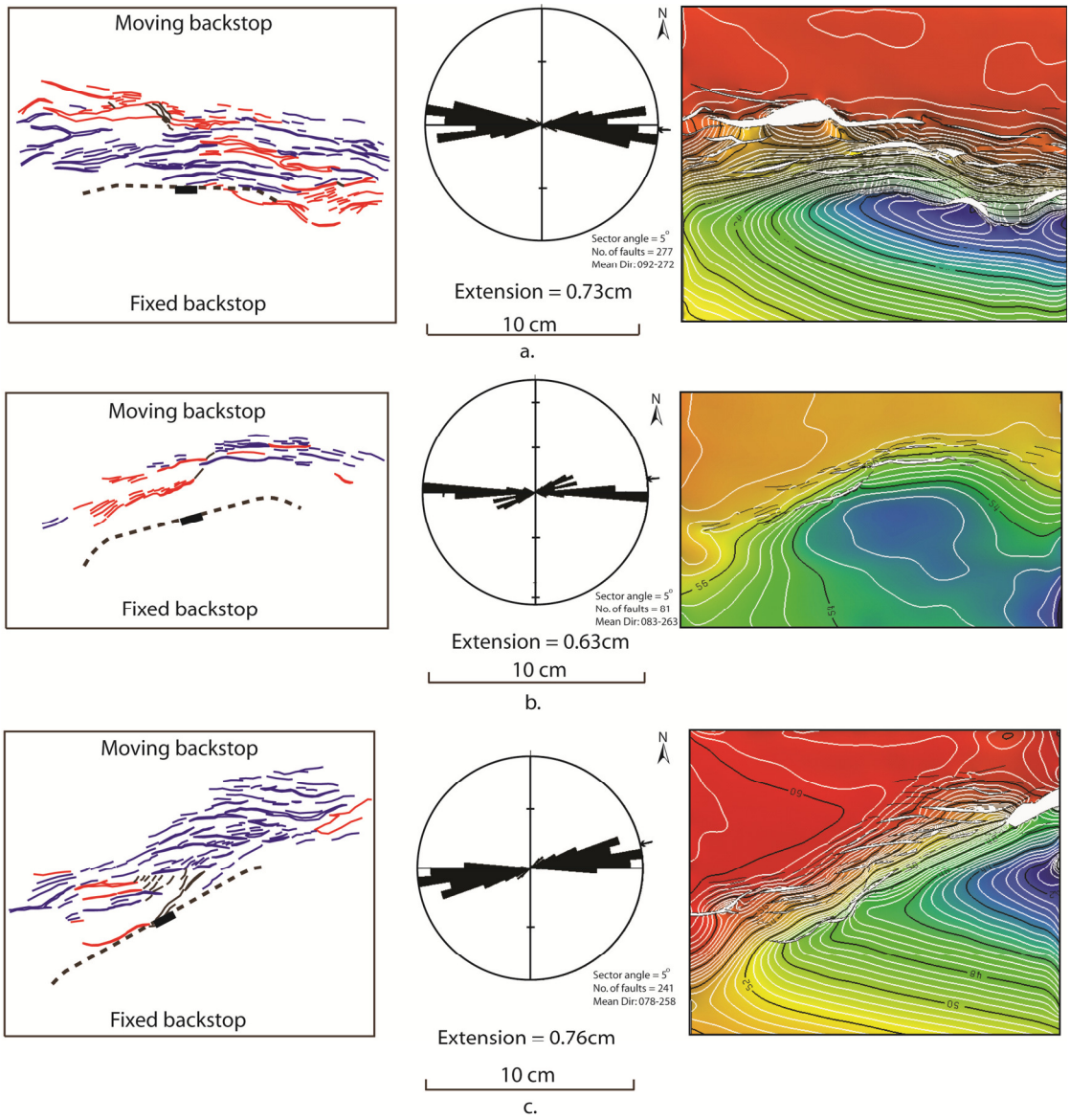

Figure 2.10 Comparison of final structural geometries and fault patterns in map view for a basement fault terminating in both directions. The contoured and gridded structure map, fault patterns and fault orientations for the top of the soft clay, are shown. a, b, and c, show patterns of basement faults that are at angles of 90, 75 and 60 degrees to the direction of extension, respectively. Basement fault geometries are shown for the final deformed state.

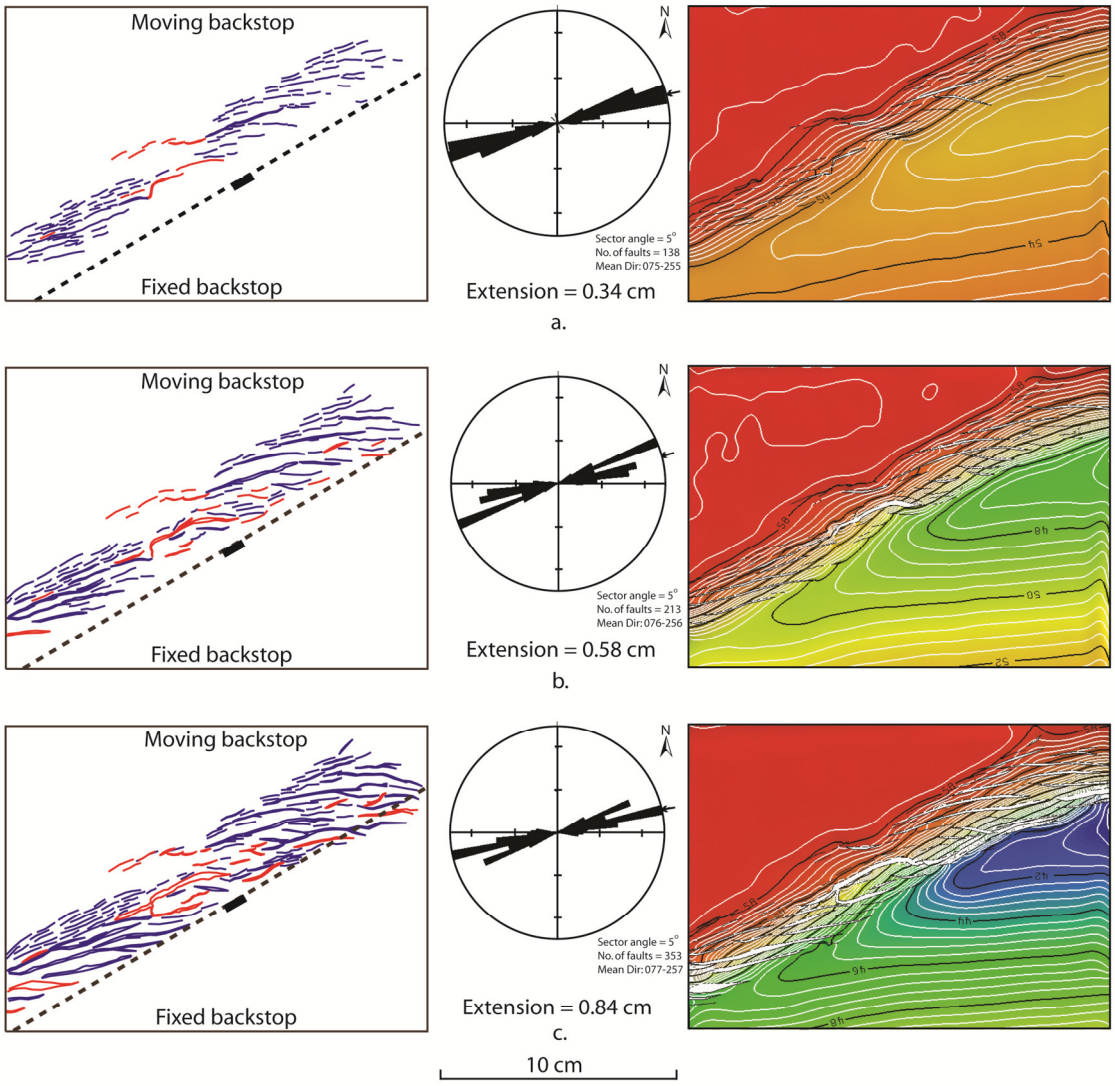

Figure 2.11 Evolution of structural geometries and fault patterns in map view for a throughgoing basement fault at 60 degrees to the extension direction. The contoured and gridded structure map, fault patterns and fault orientations for the top of the soft clay, are shown for each stage of deformation. . Rose diagrams show main orientations of faults measured. Bars show percentage of total length of faults for each orientation.

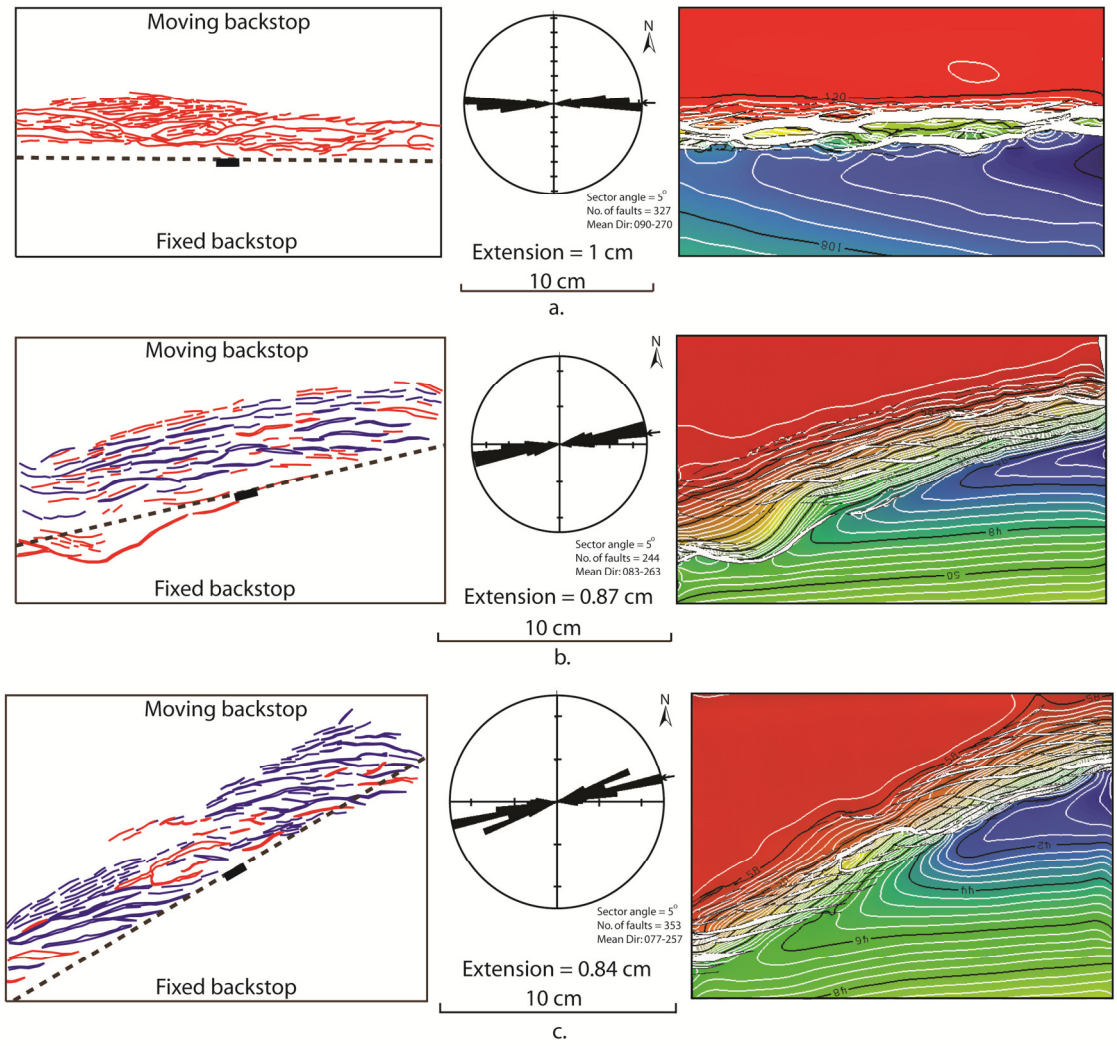

Figure 2.12 Comparison of final structural geometries and fault patterns in map view for a throughgoing basement fault at different angles to the extension direction. The contoured and gridded structure map, fault patterns and fault orientations for the top of the soft clay, are shown. a, b, and c show patterns of basement faults that are at angles of 90, 75 and 60 degrees to the direction of extension, respectively. Note the increased curvature of secondary faults from the boundaries to the center of the fault zone, and the larger number of rotated and antithetic faults (blue) for the 75 and 60 degree cases.

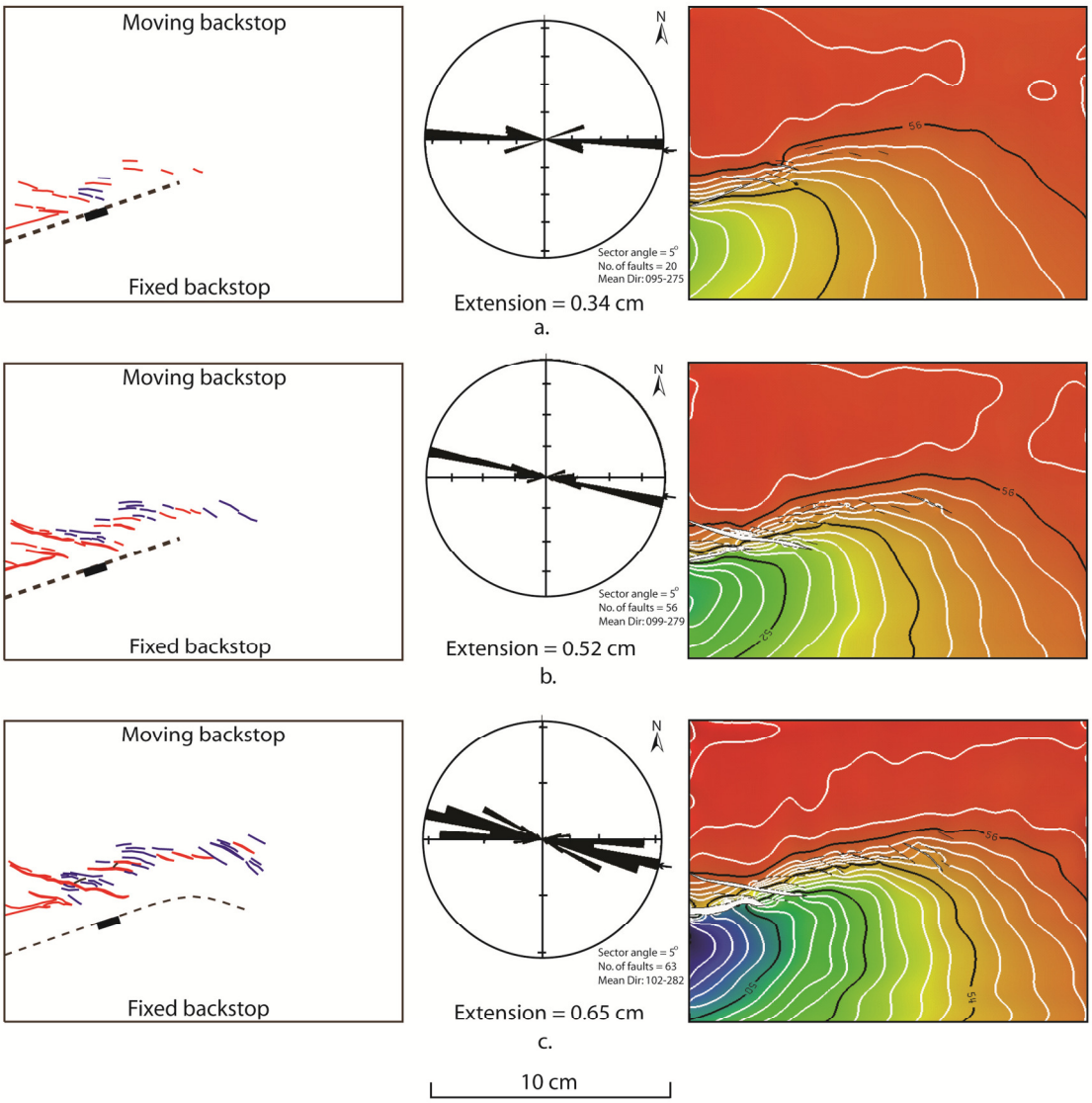

Figure 2.13 Evolution of structural geometries and fault patterns in map view for a terminating basement fault at 75 degrees to the extension direction. The contoured and gridded structure map, fault patterns and fault orientations for the top of the soft clay, are shown for each stage of deformation. Rose diagrams show main orientations of faults measured. Bars show percentage of total length of faults for each orientation. Initial basement fault geometry is shown in a and b, and the final curved final geometry is shown in c.

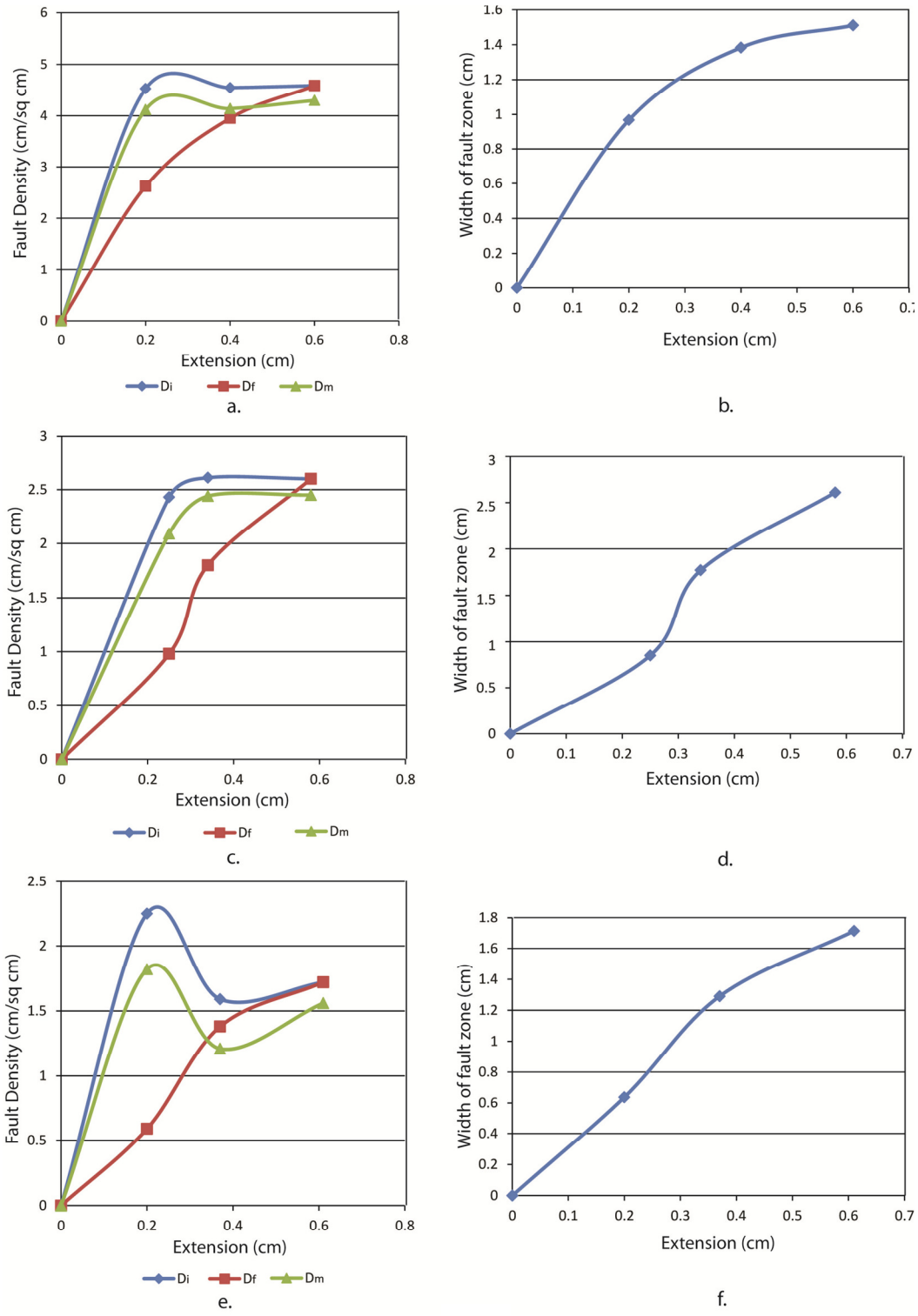

Figure 2.14 Plots of density (Di, Dm, and Df) and the width of the fault zone for different stages of deformation for basement faults with different configurations. a and b. Through going fault at 90 degrees to direction of extension. c and d. Through going fault at 60 degrees to direction of extension. e and f. Terminating fault at 90 degrees to direction of extension.

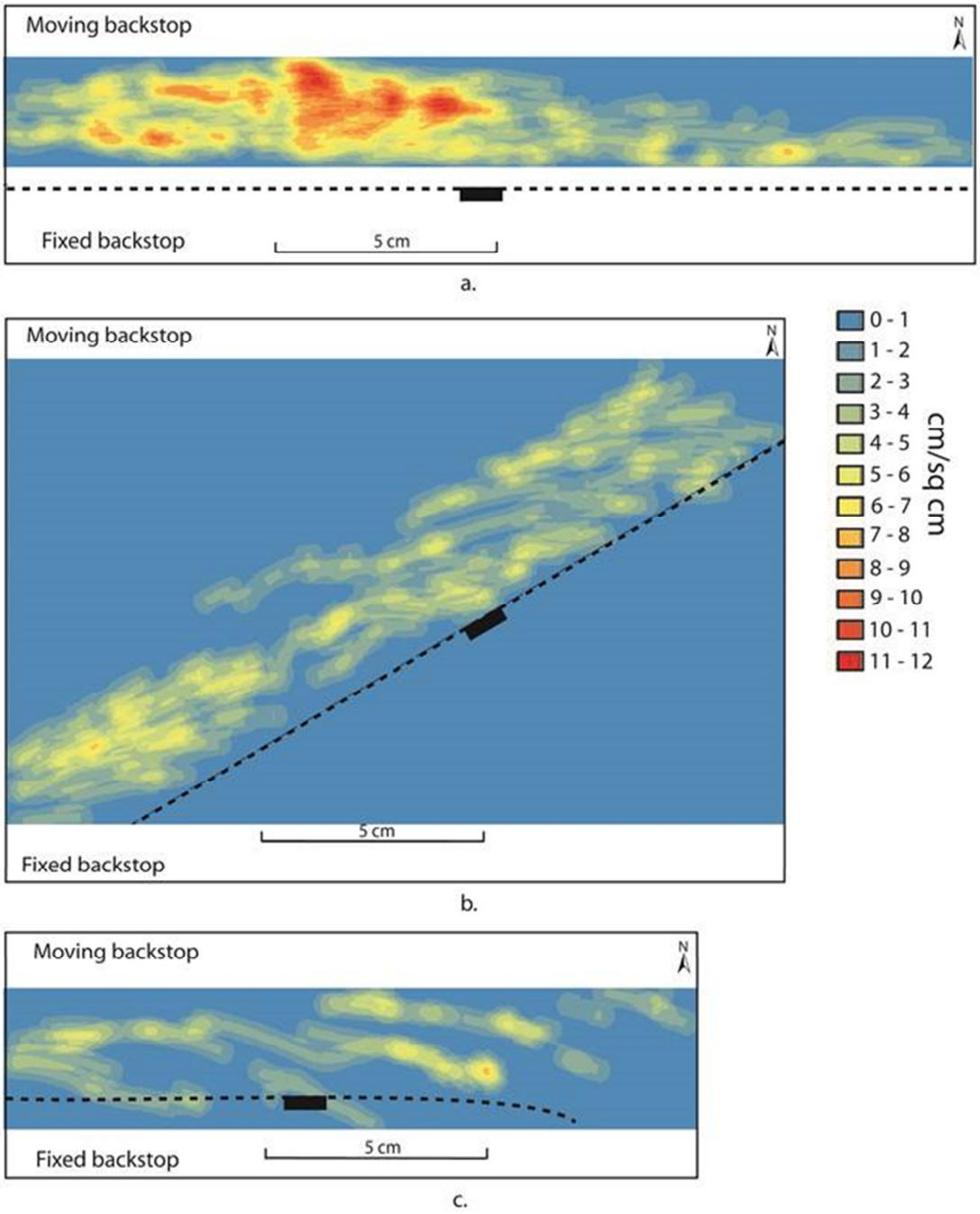

Figure 2.15 Continuous density plots for the deformation zone for different fault configurations. a. Throughgoing fault at 90 degrees to direction of extension. b. Through going fault at 60 degrees to direction of extension. c. Terminating fault at 90 degrees to direction of extension.

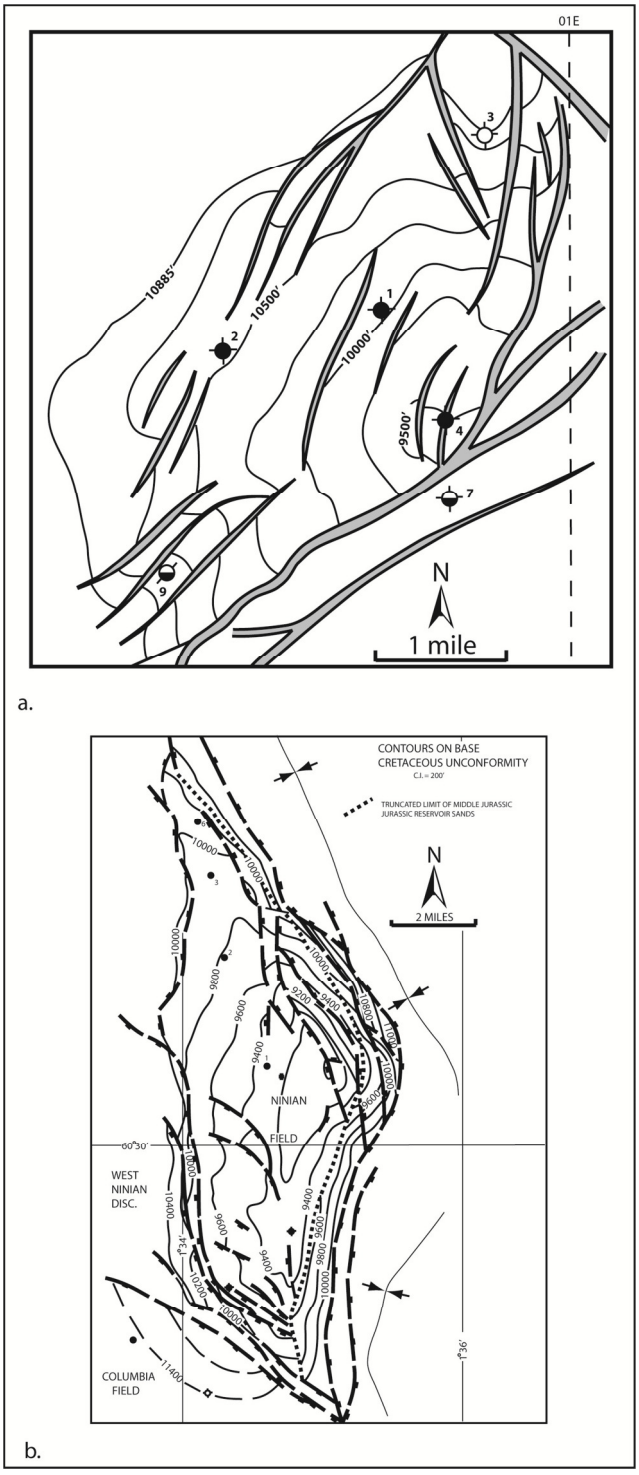

Figure 2.16 Maps for the (a) top Brent sandstone in the Heather structure and (b) the base Cretaceous unconformity in the Ninian structure in the Viking graben, North Sea. The trapdoor geometry of the structures is evident from the change in the trends of the faults and the structure along trend. For the Ninian structure the updip edge of the footwall block is eroded by the base Cretaceous unconformity. Modified from Gray and Barnes (1981) and Harding (1984).

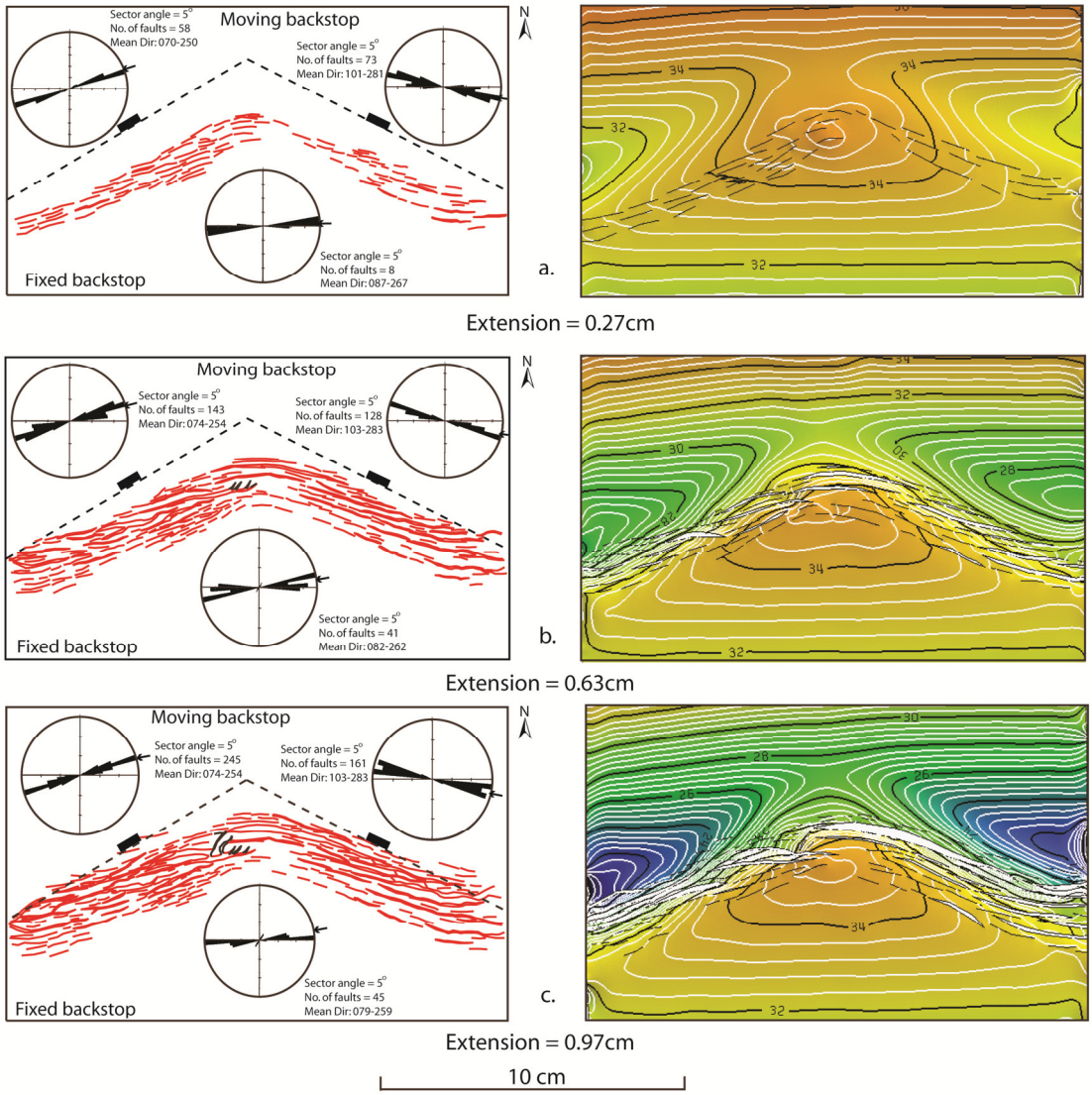

Figure 2.17 Evolution of structural geometries and fault patterns in map view for a trapdoor structure related to two faults dipping 60 degrees and intersecting at an angle of 120 degrees. The contoured and gridded structure map, fault patterns and fault orientations for the top of the soft clay, are shown for each stage of deformation. Rose diagrams show main orientations of faults measured. Bars show percentage of total length of faults for each orientation. Initial basement fault geometry is shown with dashed lines.

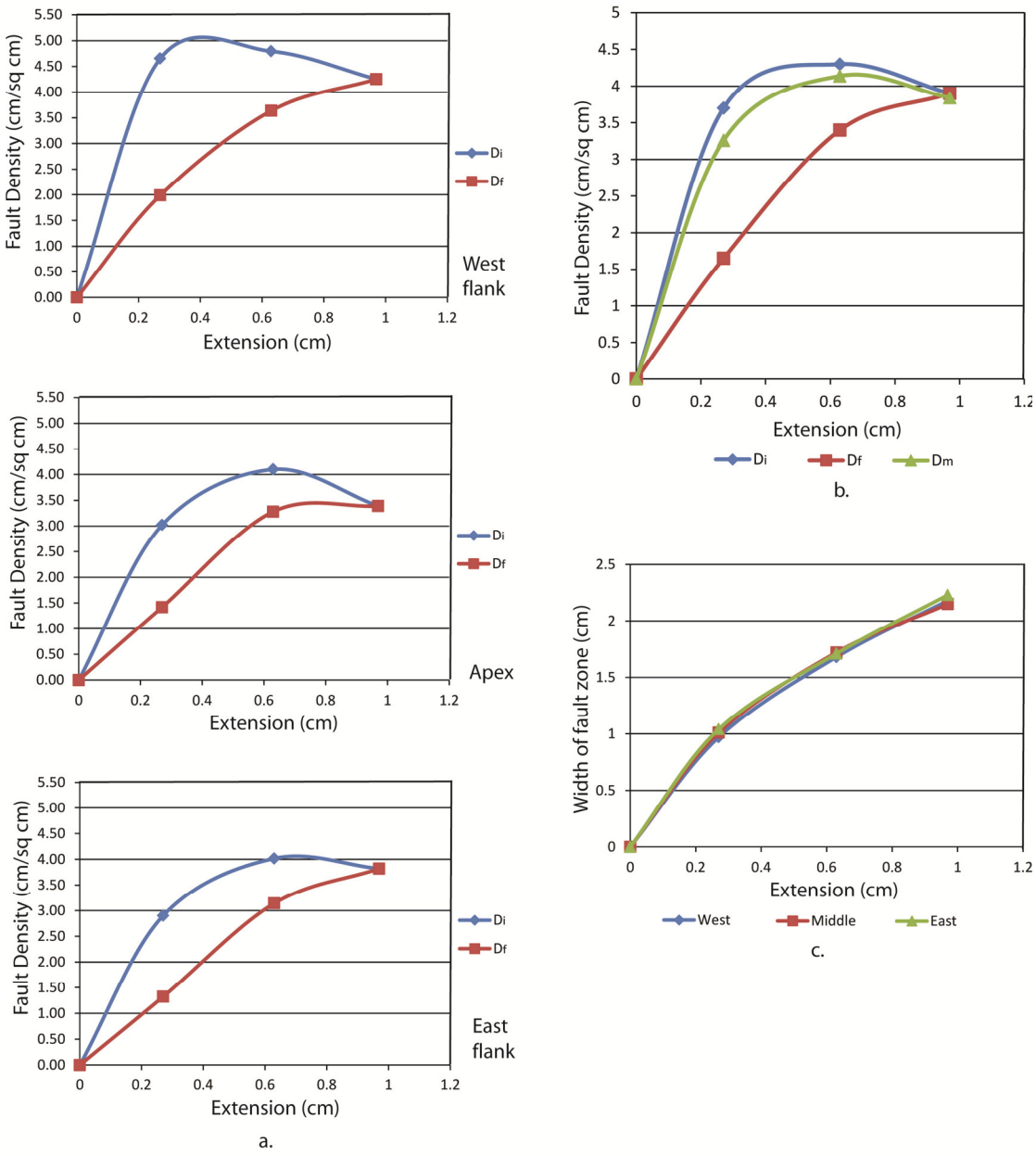

Figure 2.18 Plots of density (Di, Dm, and Df) and the width of the fault zone for different stages of deformation for basement faults associated with trapdoor structures with 120 degree intersections between faults. a. Variation in density for the different parts of the structure. b. Density variations for the entire structure. c. Width of the fault zone for different parts of the structure.

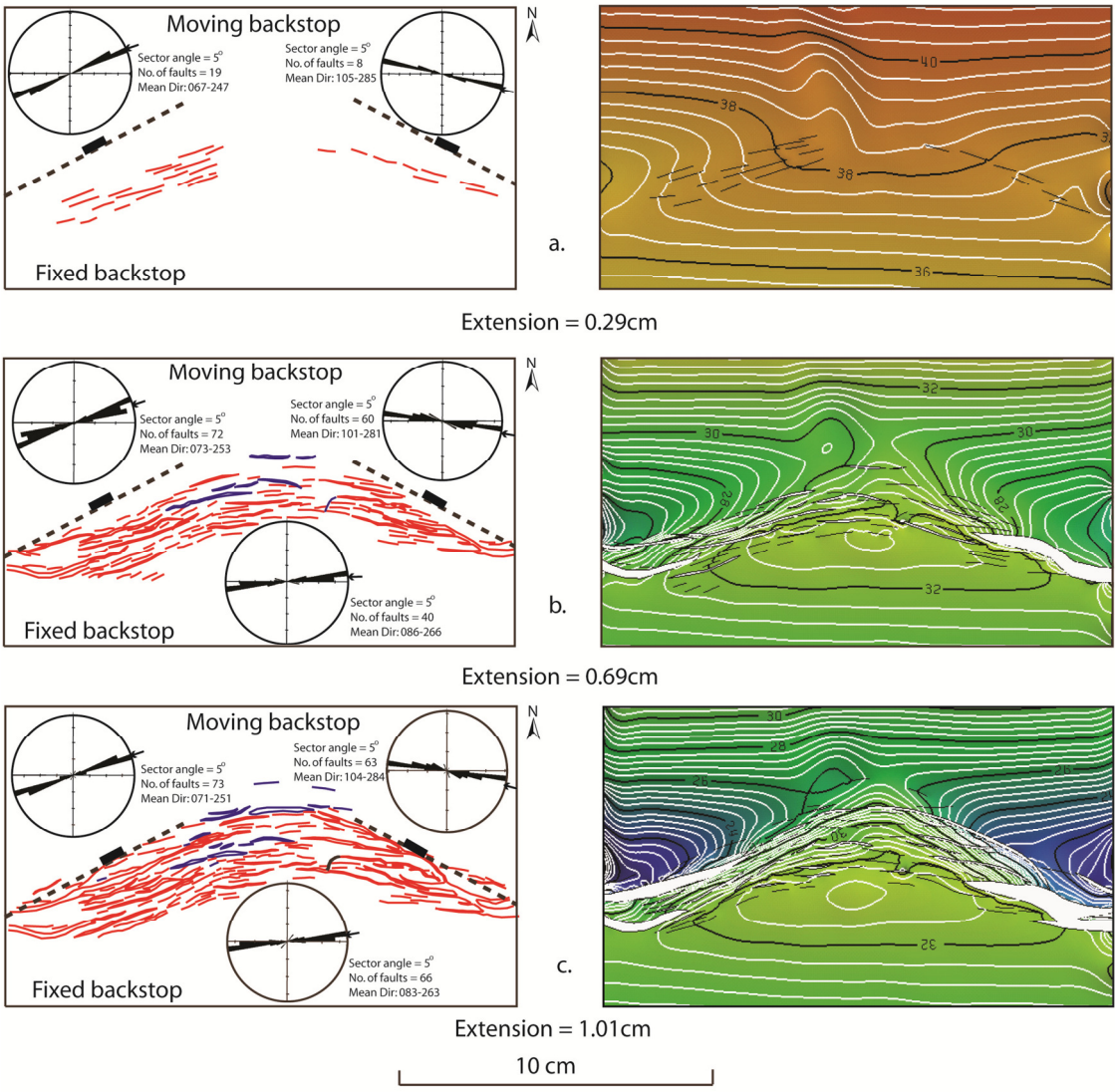

Figure 2.19 Evolution of structural geometries and fault patterns in map view for a trapdoor structure related to two terminating faults dipping 60 degrees with the projected trends intersecting at an angle of 120 degrees. The trapdoor structure results from the propagation of the two faults to the apical area. The contoured and gridded structure map, fault patterns and fault orientations for the top of the soft clay are shown for each stage of deformation. Rose diagrams show main orientations of faults measured. Bars show percentage of total length of faults for each orientation. Initial basement fault geometry is shown with dashed lines.

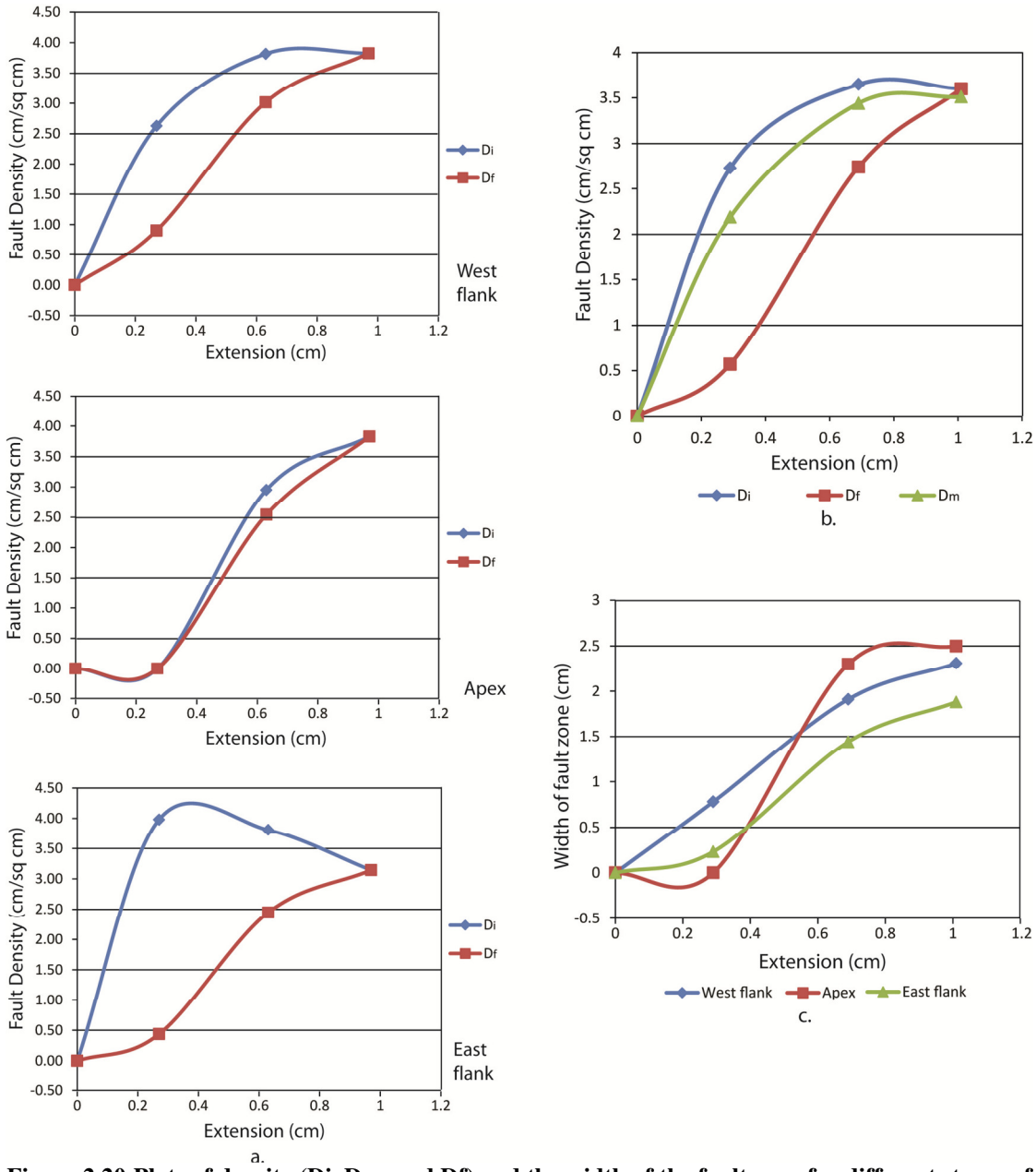

Figure 2.20 Plots of density (Di, Dm, and Df) and the width of the fault zone for different stages of deformation for basement faults associated with trapdoor structures with propagating faults. The projections of the two faults intersect at 120 degree intersections. a. Variation in density for the different parts of the structure. b. Density variations for the entire structure. c. Width of the fault zone for different parts of the structure.

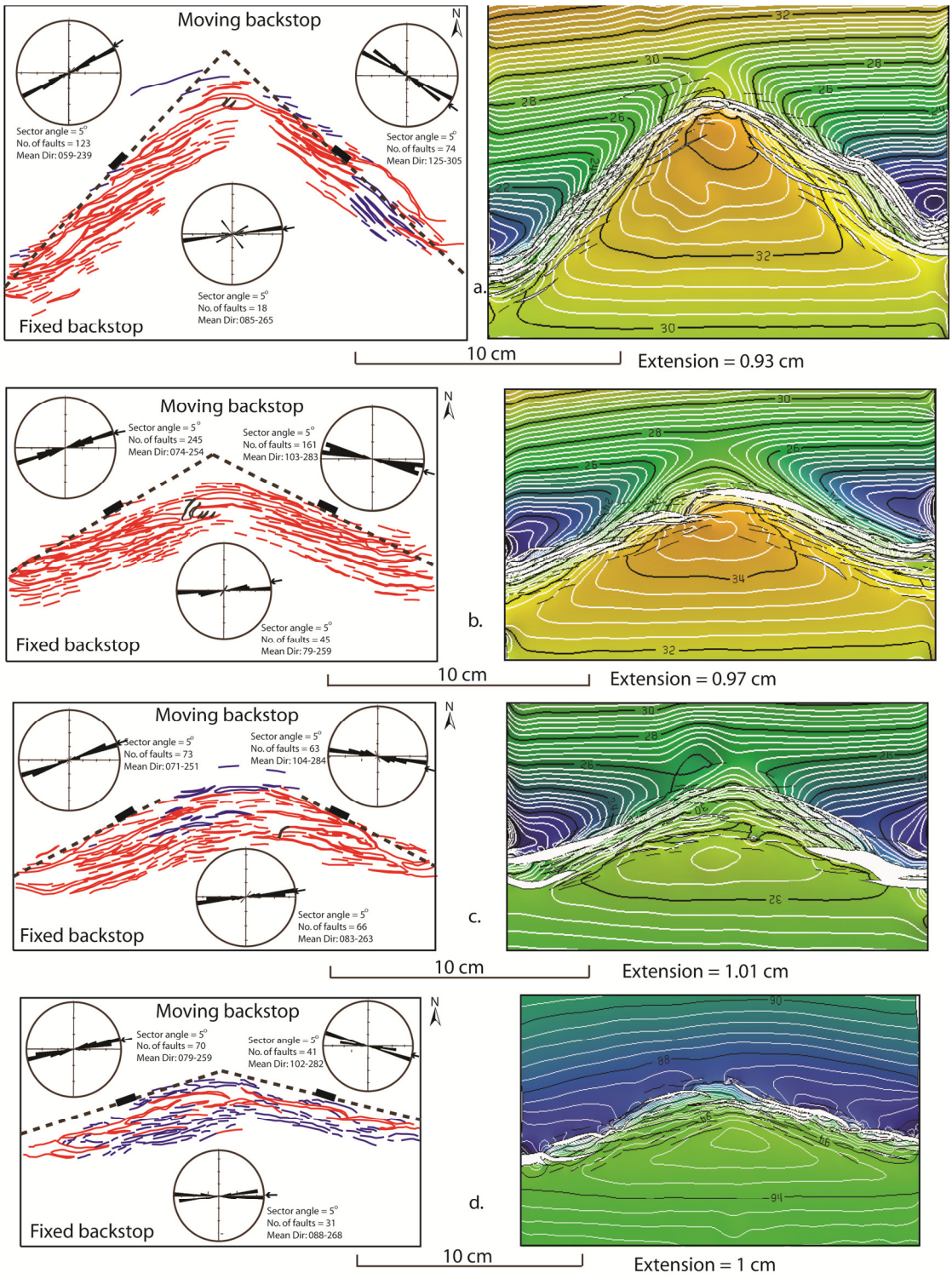

Figure 2.21 Comparison of final structural geometries and fault patterns in map view for trapdoor structures with different interesting angles. a. 90 degree intersection. b. 120 degree intersection. c. Terminating basement faults with a 120 degree intersection. d. 140 degree intersection. The contoured and gridded structure map, fault patterns and fault orientations for the top of the soft clay, are shown. See text for major differences.

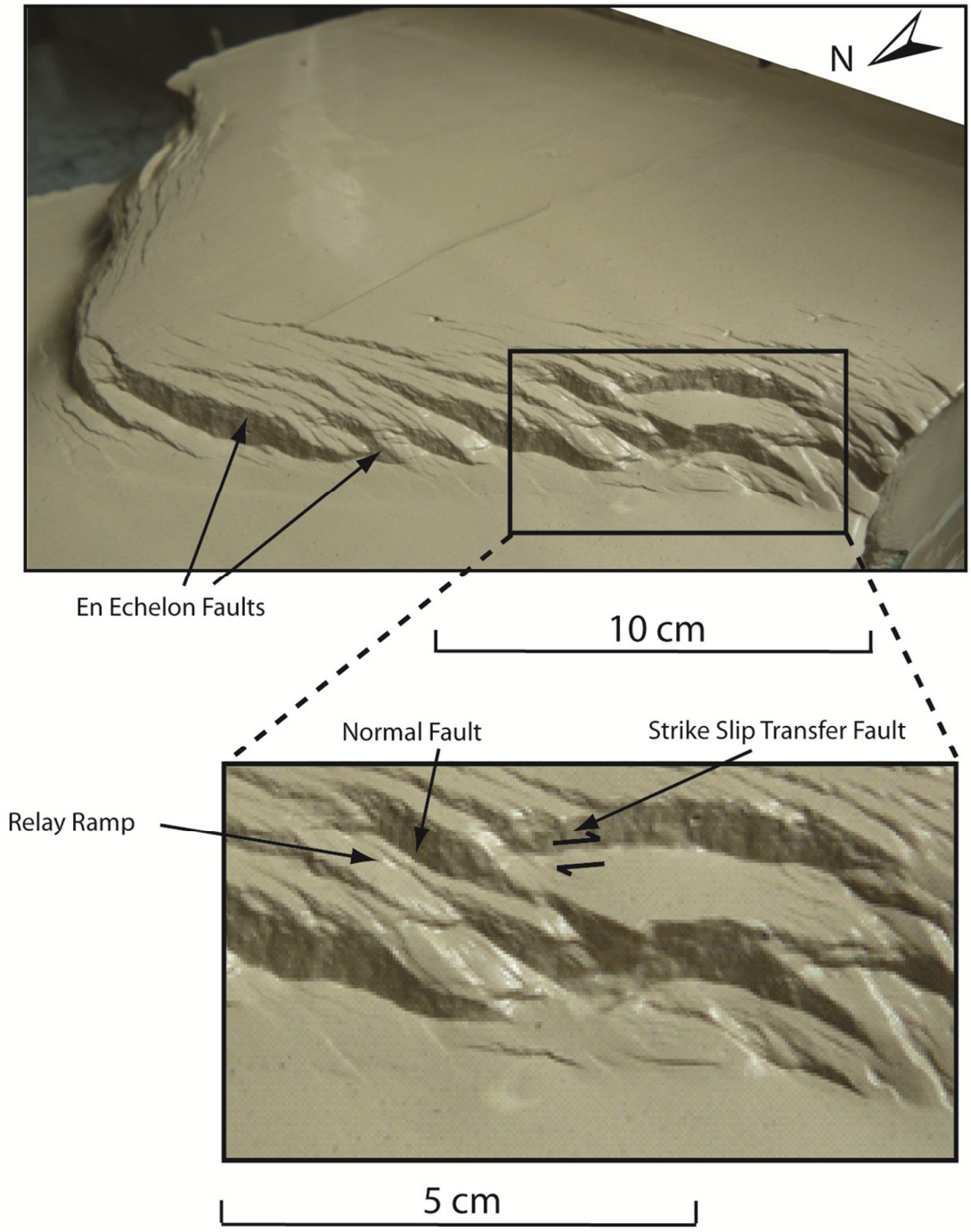

Figure 2.22 Photograph of the frontal limb of a drape fold formed on a trapdoor structure formed by two faults intersecting at 90 degrees. Note the progressive transfer of slip towards the apex from the back to the front along en echelon faults connected by relay ramps. Strike-slip faults transfer slip between some of the normal faults (inset shows details).

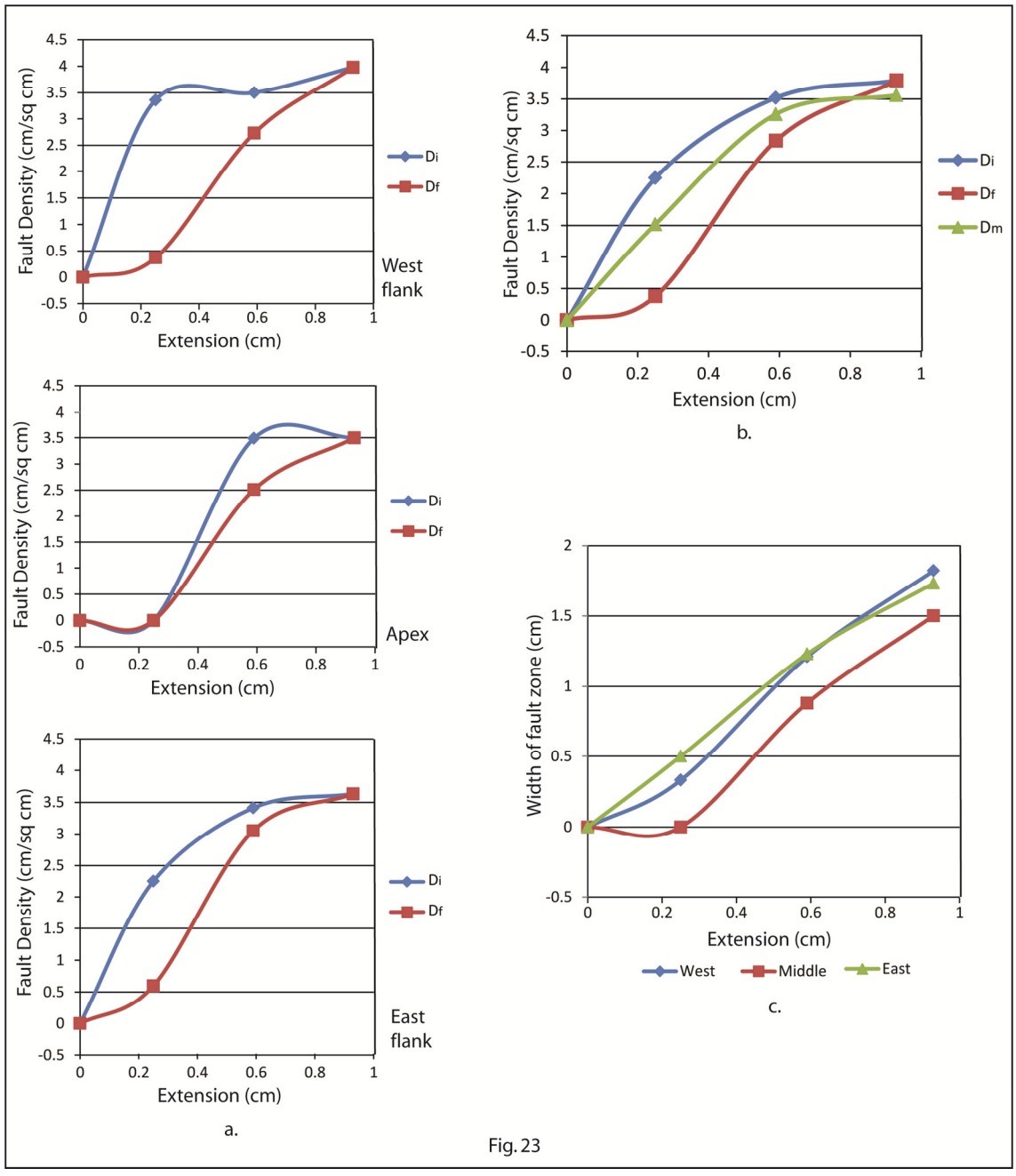

Figure 2.23 Plots of density (Di, Dm, and Df) and the width of the fault zone for different stages of deformation for basement faults associated with trapdoor structures formed by intersecting faults with a 90 degree angle. a. Variation in density for the different parts of the structure. b. Density variations for the entire structure. c. Width of the fault zone for different parts of the structure.

References

Allmendinger, R.W., 1998, Inverse and forward numerical modeling of trishear fault-propagation folds: Tectonics, v. 17. no.4, p.640-656.

Attewell, P. B., and I.W. Farmer, 1976, Principles of engineering geology: Chapman and Hall: London.

Byerlee, J., 1978, Friction of rocks: Pure and Applied Geophysics, v.116, p.615-626.

Cloos, H., 1929, Experimente zur inneren tektonik: Centralblatt für Mineralogie B, p.609-621.

Cloos, H., 1930, Künstliche Gebirge: Natur und Museum, v.59, p.225-243,

Cristallini, E.O. and R.W. Allmendinger, 2001, Pseudo-3D modeling of trishear fault-propagation folding: Journal of Structural Geology, v.23, p.1883-1899.

Cristallini, E.O., L. Giambiagi and R.W. Allmendinger, 2004, True three-dimensional trishear: A kinematic model for strike-slip and oblique-slip deformation: Geological Society of America Bulletin, v.116, p.938-952.

Erslev, E.A.,1991, Trishear fault-propagation folding: Geology, v.19, p.617-620.

Fossen, H., 1992, The role of extensional tectonic in the Caledonies of south Norway: Journal of Structural Geology, v.14, p.1033-1046.

Freund, R., 1979, Progressive strain in beds of monoclinal flexures: Geology, v.7, p.269-271.

Gray, W.D.T. and G. Barnes,1981, The Heather oil field *in* Illing, L.V and G.D. Hobson eds, Petroleum Geology of the Continental Shelf of North-West Europe: Institute of Petroleum, Hayden and Son, London, p. 335-341.

Handin, J., 1966, Strength and ductility *in* Clark Jr., S.P ed. Handbook of Physical Constants: Geological Society of America Memoir, v.97, p.223-289.

Hardy, S. and M. Ford,1997, Numerical modeling of trishear fault propagation folding: Tectonics, v. 16, no.5, p.841-854.

Harding, T. P.,1984, Graben hydrocarbon occurrence and structural style: American Association of Petroleum Geologists Bulletin: v.68, p.333-362.

Hardy, S. and R.W. Allmendinger, 2011, Trishear: A review of kinematics, mechanics and applications *in* McClay, K., J.H. Shaw and J. Suppe eds, Thrust Fault Related Folding: A.A.P.G Memoir, v.94, p.95-121.

Hubbert, M.K., 1937, Theory of scale models as applied to the study of geologic structures: Geological Society of America Bulletin,v.48, p.1459-1519.

Jin, G., and R.H. Groshong Jr, 2006, Trishear kinematic modeling of extensional fault-propagation folding: Journal of Structural Geology, v.28, p.170-183.

Miller, J.F. and S. Mitra, 2011, Deformation and secondary faulting associated with basement-involved compressional and extensional structures: American Association of Petroleum Geologists Bulletin, v.95, no.4, p.675-689.

Mitra, S.,1990, Geometry and kinematic evolution of inversion structures: American Association of Petroleum Geologists Bulletin, v.77, p.1159-1191.

Mitra, S. and J.F. Miller, 2013, Strain variation with progressive deformation in basement-involved trishear structures: Journal of Structural Geology, v.53, p.70-79.

Mitra, S. and V.S. Mount, 1998, Foreland Basement-Involved Structures: American Association of Petroleum Geologists Bulletin, v.82, no.1, p.70-109.

Mitra, S. and D. Paul, 2011, Structural geometry and evolution of releasing and restraining bends: Insights from laser-scanned experimental models: American Association of Petroleum Geologists Bulletin, v.95, no.7, p.1147-1180.

Paul, D. and S. Mitra, 2012, Controls of basement faults on the geometry and evolution of compressional basement-involved structures: American Association of Petroleum Geologists Bulletin, v.96, no.10, p.1899-1930.

Paul, D. and S. Mitra, 2013, Experimental models of transfer zones in rift systems: American Association of Petroleum Geologists Bulletin, v.97, p.759-780.

Reches, Z. and A.M. Johnson, 1976, A theory of concentric, kink and sinusoidal folding and of monoclonal flexuring of compressible, elastic multilayers: VI. Asymmetric folding and monoclonal kinking: Tectonophysics, v.35, p.295-334.

Reches, Z., 1978, Development of monoclines: Part I. Structure of the Palisades Creek branch of the East Kaibab monocline, Grand Canyon, Arizona *in* Matthews III V. ed. Laramide Folding Associated with Basement Block Faulting in the Western United States: Geological Society of America 151, p.235-271.

Reches, Z. and A.M. Johnson, 1978, Development of monoclines: Part II. Theoretical analysis of monoclines *in* Matthews III V. ed. Laramide Folding Associated with Basement Block Faulting in the Western United States: Geological Society of America 151, p.273-311.

Richard, P. and R.W. Krantz, 1991, Experiments on fault reactivation in strike-slip mode: Tectonophysics, v.188, p.117-131.

Sharp, I.R., R.L. Gawthorpe, J.R. Underhill and S. Gupta, 2000, Fault propagation folding in extensional settings: Examples of structural style and synrift sedimentary

response from the Suez rift, Sinai, Egypt: Geological Society of America Bulletin, v.112, p.1877-1899.

Sagy A., Z. Reches and A. Agnon, 2003, Hierarchic three-dimensional structure and slip partitioning in the Western Dead Sea pull-apart: Tectonics, v.22, no.1, p.1-17.

Schlische, R.W. and M.O. Withjack, 2009, Origin of fault domains and fault-domain boundaries (transfer zones and accommodation zones) in extensional provinces: Result of random nucleation and self-organized fault growth: Journal of Structural Geology, v.31, p.910-925.

Stearns, D. W.,1978, Faulting and forced folding in the Rocky Mountain foreland in Mathews, V., III eds, Laramide folding associated with block faulting in the western United States: Geological Society of America Memoir, v.151, p.1-37.

Vendeville, B., M.O. Withjack and G. Eisenstadt, 1995, Introduction to Experimental Modeling of Tectonic Processes: Short Course Notes, 1995 National Meeting, Geological Society of America.

Withjack, M. O., K.E. Meisling, and L.R. Russel, 1989, Forced folding and basement-detached normal faulting in the Haltenbanken area, offshore Norway in Tankard, A.J. and H.R. Balkwill eds, Extensional Tectonics and Stratigraphy of the North Atlantic Margins: AAPG Memoir, v.46. p.567-575.

Withjack, M.O., J. Olson and E. Peterson, 1990, Experimental models of extensional forced folds: American Association of Petroleum Geologists Bulletin, v.74, no.7, p.1038-1054.

Zehnder, A.T. and R.W. Allmendinger, 2000, Velocity field for the trishear model: Journal of Structural Geology, v.22, p.1009-1014.

CHAPTER 3
EXPERIMENTAL MODELS OF TRANSFER ZONES IN RIFT SYSTEMS

Abstract

Transfer zones in rift basins are classified into convergent, divergent, and synthetic, based on the relative dip directions of adjacent faults within the transfer zone. Experimental models were constructed to determine the geometry, evolution and fault patterns associated with each of these transfer zones. In addition, basement faults with initial approaching, lateral offset and overlapping geometries were modeled. The models consisted of two layers, with stiff clay representing basement and soft clay representing the sedimentary cover. Laser scanning and three-dimensional surface modeling were used to determine the map geometry to compare the models with examples of natural structures. The experimental models showed many similarities with conceptual models, but also showed more details and a few significant differences. Typically, divergent transfer zones are narrower than convergent transfer zones, for the same initial spacing between basement faults. The differences between the different initial fault configurations (approaching, laterally offset, or overlapping) are the degree of interaction of the secondary faults, the amount of overlap between the fault zones, and in some cases, the width of the transfer zone. The main faults propagate laterally and upward and curve in the direction of dip of the faults, so that the faults curve towards each other in convergent transfer zones, away from each other in divergent transfer zones, and in the same direction in synthetic transfer zones. A primary difference with schematic models is the significant component of extensional fault propagation folding (drape folding), accompanied by secondary faulting within the

sedimentary cover, especially in the early stages of fault propagation. Therefore, all three types of transfer zones are characterized by significant folding and related variations in the shapes of structures. The transfer zones are marked by a progressive change in relief from the footwall to the hanging wall, resulting in a saddle-shaped geometry. The hanging walls of the faults are marked by a gentle flexure or rollover into the fault, with the amount of flexure increasing with fault throw away from the fault tip. The geometries and fault patterns of the experimental structures match some of the observations in natural structures, and also provide predictive analogs for interpretation of surface and subsurface structures and the delineation of structural traps in rift basins.

3.1 Introduction

Transfer zones are common features in rift basins, where deformation between normal faults is accommodated by the formation of oblique structures and complex secondary fault systems. The transfer zones result from the interference between adjacent laterally propagating normal faults. Three common types of transfer zones are: (1) Convergent, with the main faults dipping towards each other (2) Divergent, with the main faults dipping away from each other, and (3) Synthetic, with the faults dipping in the same direction (Figure 3.1). Schematic models of the map geometries of primary and secondary faults in the transfer zone, and the resulting structural geometries were described by Rosendahl (1987), and subsequently by Morley et al (1990) and Faulds and Varga (1998). Rosendahl (1987) classified the transfer zones into high relief and low relief accommodation zones, and also described similar polarity half grabens. Morley et al (1990) classified the transfer zones into convergent, divergent, and synthetic based on their relative attitude and dip directions of major faults, and into approaching, partially overlapping, overlapping (collateral), and collinear, depending on the relative positions of the tips of the adjacent faults. Some of the terms coined by Morley et al (1990) are commonly used to describe transfer zone geometries.
Detailed studies of transfer zones in rift systems have been conducted by many authors, who have addressed fault linkages and displacement transfer between faults (Peacock and Sanderson, 1991; Trudgill and Cartwright, 1994; Huggins et al., 1995; Childs et al., 1995; Crider and Pollard, 1998; Gupta et al, 1998; Moore and Schultz, 1999; Gupta and Scholz, 2000; Crider, 2001; Younes and McClay, 2002; Fossen et al, 2010), structural variations within different transfer zones (Rosendahl, 1987; Larsen, 1988; Morley et al,

1990; Younes and McClay ,2002; Nelson et al, 1992; Moustafa, 2002), controls of sedimentation patterns by relay ramps (Gawthorpe and Hurst, 1993; Athmer and Luthi, 2011) and hydrocarbon traps related to the transfer zones (Rosendahl, 1987; Morley et al., 1990; Fossen et al, 2010).

Rosendahl (1987) and Morley et al (1990) documented the detailed structures in transfer zones in the East African rift systems. Scott and Rosendahl (1989) compared the transfer zones in the East African rift system with those in the Viking graben. Ebinger (1989), Morley et al (1990), Younes and McClay (2002) and Moustafa (2002) mapped transfer zones in the Gulf of Suez- Red Sea area, with particular emphasis of the formation of secondary fault arrays in these areas. Larsen (1988) documented different transfer zone configurations in East Greenland. These and other studies have significantly added to the understanding of transfer zone geometries and their evolution.

In this paper, some experimental models of transfer zones were developed to better understand their geometry and evolution, and to compare with observations in surface and subsurface structures. Two- layer models with stiff clay representing basement and soft clay representing the sedimentary cover were used in the experiments. Convergent, divergent and synthetic structures are modeled, and for each case, basement faults with approaching, laterally offset, and overlapping geometries are considered.

Documentation of both the fault patterns and the three-dimensional topologies of the surfaces with progressive evolution enable an understanding of the nature of secondary faults and structural geometry.

One of the key differences in the model results is a significant component of drape folding within the soft clay, accompanied by the distribution of slip along a number of

secondary faults. This also results in a characteristic saddle shape of the transfer zones, which has not been previously documented.

Transfer zones have been identified as important locations for the development of structural traps (Morley et al, 1990). Therefore the details of the saddle-shaped geometry of transfer zones resulting from drape folding will be important in the interpretation of structures and delineation of traps in rift basins.

3.2 Previous Experimental Studies

Experimental models have been used to understand the geometry and evolution of macroscopic extensional structures. Rift structures involving planar basement normal faults have been investigated using both clay and sand models (Sanford, 1959; Horsfield, 1977; Withjack et al., 1990; Withjack and Calloway, 2000; Jin and Groshong, 2006; Miller and Mitra, 2011). Withjack et al. (1990) studied the propagation of faults from the basement to the sedimentary cover and the resulting formation of drape or forced folds and secondary faults. Similar experiments were also conducted by Jin and Groshong (2006) and Miller and Mitra (2011), who also found similar results. Withjack and Calloway (2000) further investigated the role of salt layers in the evolution of the structures and related faults.

Three-dimensional models investigating the effects of oblique slip on normal faults and their controls on the component of strike-slip deformation have also been conducted (Withjack and Jamison, 1986; Serra and Nelson, 1988). McClay and White (1995) and McClay et al (2002) also used sand models to examine the orientations and patterns of secondary faults for pure and oblique extension. Analog experimental sand models have also been conducted in order to understand the role of salt in the formation of transfer

zones (Le Calvez and Vendeville, 2002). Most of these studies have examined the cross sectional geometry and evolution of faults and related folds. However, experimental approaches have not been applied to study the map geometry and evolution of transfer zones.

Previous experimental models mostly used rigid blocks to represent basement, and soft materials (sand or clay) to represent the overlying sedimentary rocks. Although these configurations were appropriate for the study of the cross sectional geometries of structures, or oblique slip on through going faults, they are not suitable for modeling transfer zones, which involve the lateral propagation of faults, and variable slip along strike on the main faults. Precut faults in rigid blocks cannot propagate with increasing extension, and need to be replaced by material which enables fault propagation. Furthermore, variable fault slip along trend involves flexure, which must be accommodated by internal strain in the vicinity of the faults to prevent gaps from opening up.

3.3 Experimental Methodology

3.3.1 Experimental Setup

Clay experiments were conducted using a motor driven apparatus for convergent, divergent and synthetic transfer zones. For each of these transfer zones, models were conducted for approaching, overlapping and laterally offset faults. Each experiment was repeated at least twice to ensure repeatability.

The apparatus is made up of two plexiglass backstops, one of which is fixed, while the other is connected to two motors which control the rate of motion (Figure 3.2). The competency contrast between the weaker cover units and the rigid basement was

modeled by choosing stiff clay for the basement and soft clay for the cover units. Cuts in the stiff clay were used to model pre-existing basement normal faults which resulted in the propagation of faults through the stiff and wet clay. This combination of materials for the basement/sedimentary cover package has been successfully applied to model both strike-slip faults (Mitra and Paul, 2011) and basement involved compressive structures (Paul and Mitra, 2012). The stiff clay has a density of 1.85 gm/cc and a thickness of 1 inch (2.5 cm). The soft clay has a density of 1.6-1.65 gm/cc and a thickness of 1inch (2.5 cm). There is a significant contrast in strength between the stiff and soft clay that influences the nature of deformation of the structures.

There are a number of advantages of using stiff clay over the rigid metal or wooden blocks used in most of the earlier work on experimental analog modeling. The stiff clay can be cut to produce specific pre-existing fault geometries or discontinuities in the basement, including terminating faults. Moreover, the stiff clay can deform in the vicinity of the main faults and also develop secondary faults. These factors are critical in modeling transfer zones, which involve laterally propagating faults with variable slip, so that basement must deform, at least locally, adjacent to the faults. The main advantage of using wet clay is that it allows a good definition of geometry and evolution of faults.

Major faults were modeled with a dip of 60 degrees. Movement on the faults was initiated by movement of the movable plate, which caused the fault blocks to drop down along the preexisting fault cuts. The rates of shortening were kept constant at about 0.0005 cm/sec for all experiments. For scaling and limitation of the experimental models refer to Chapter 2 Section 2.3.2.

3.3.2 Experimental Configurations

Three main experimental configurations were used, representing divergent, convergent, and synthetic transfer zones. Pre-existing cuts in the stiff clay provided the discontinuities along which the faults propagated both laterally within the stiff clay, as well as upward through the soft clay. The pre-existing cuts dipped away from each other for divergent, towards each other for convergent, and in the same direction for synthetic transfer zones. The stiff clay representing the basement was always thinner in the hanging wall blocks to allow these blocks to drop down along planar faults. However, there was sufficient thickness of the stiff clay in the hanging wall to prevent deformation by body forces.

For each of these types of transfer zones, initially approaching, lateral offset, and overlapping fault pairs were investigated (Figure 3.3). In contrast to these terms being applied to final configurations of basement faults (Morley et al, 1990), these precut geometries represent different configurations of discontinuities in the basement prior to the propagation of the faults, resulting in different transfer zone geometries. All of these configurations result in overlapping fault geometries in the final stages of deformation, but the degree of overlap and the nature of fault interactions vary.

3.4 Analysis of Data

The models were used to study the three-dimensional and map geometry of the structures and related faults, as well as the patterns and orientations of secondary faults. Therefore, data analysis was conducted on two datasets: (1) fault data that were digitized and extracted from the photographs, and (2) scanner data, obtained as point clouds, which were used to develop 3-D models of the surface.

3.4.1 Fault Patterns and Orientations

Photographs taken at approximately two minute intervals during the experiment were used for the analysis of the variation of orientation of the faults. Fault patterns were analyzed for different stages of formation of the structures to document their evolution with time. Rose diagrams were used to document the map trends (strikes) of the secondary faults.

3.4.2 3-D Surface Analysis

The surface of the soft clay was modeled to study the three-dimensional geometry of the structure. Point sets obtained from laser-scanning were used to build the surfaces and to develop grids and contours. The horizontal and vertical resolution of the point sets was75 DPI (~0.015 inches
point density). This enabled mapping of faults with a minimum vertical separation of approximately 0.4 mm. The details of the method of laser-scanning and modeling of surfaces are discussed by Bose and Mitra (2010). The modeled surfaces were compared with the photographs to incorporate the detailed geometry of the fault surfaces (Figure 3.4). Major faults and many minor faults were mapped and cut out on the unsmoothed surfaces (Figure 3.4b). Some of the smallest faults were not mapped because of resolution limitations. A number of closely-spaced minor faults were sometimes mapped as a single fault, if they could not be mapped separately because of resolution problems. The faults and faulted surfaces were then smoothed before contouring the surfaces to determine the final topology (Figure 3.4c). This approach enabled the surfaces to be correctly contoured incorporating all major and many secondary faults.

The contour interval used for all the surfaces was 0.4 mm. Changes in the surface geometry were used to study the evolution of the structures and related faults.

3.5 Experimental Results:

In this section, the progressive evolution of structures and faults for convergent, divergent and synthetic transfer zones are discussed. Orientations of all features are described relative to an arbitrarily chosen north direction, which coincides with the direction of the moving backstop.

3.5.1 Convergent Transfer Zones

The structural and fault geometries were studied for three separate experimental setups, representing initial basement fault geometries which were approaching, laterally offset and overlapping. A special case of the lateral offset, in which the two major faults are connected by a cross fault in the stiff clay was also conducted.

Laterally Offset Faults

For the laterally offset basement faults dipping towards each other (Figure 3.5a), initial extension (0.13 cm displacement) resulted in the propagation of the fault closest to the moving backstop (Figure 3.5b). The fault propagated to the top of the soft clay and developed an extensional fault propagation (drape) fold and related secondary faults. The secondary faults were mostly synthetic to the main fault and formed an anastomosing network, curving slightly towards the south at their eastern termination, so that the fault strikes varied from E-W to ENE-WSW.

With increasing displacement the fault zone continued to spread eastward, and deformation progressed to the southeastern basement fault, where a similar drape fold and related fault zone developed at 0.23 cm of displacement (Figure 3.5c).

Subsequently, two well defined overlapping fault zones developed (0.33 cm displacement- Figure 3.5d), separated by a transfer zone connecting the points of termination of the two fault zones. The secondary faults connected to form major faults in the northern area.

As the transfer zone matured, each fault zone developed a major drape fold immediately above the basement fault and a gentle rollover structure with decreasing elevation in the vicinity of the fault zones (Figures 3.5e and f). In the very late stages (0.53 cm displacement), major faults developed at the top of the soft clay above each of the basement faults. The footwalls of the two fault zones were connected by an ENE-WNW trending low relief transfer zone (LRAZ of Rosendahl, 1987). The width of the transfer zone decreased in the middle, primarily as a result of significant drape folding along each major fault zone. The width also decreased with progressive evolution but the acute angle between the long axis of the LRAZ at its center and the strike of the fault zones (approximately 34˚) remained approximately constant. A system of south dipping antithetic faults formed on the rollover above the southern fault. These faults also extended into the transfer zone, where the faults swung into more ENE-WNW trends, as documented in the rose diagrams. A series of horst-graben structures developed due to the interaction of the north-and south dipping faults.

A separate experiment was conducted in which the tips of the two faults in the basement were connected by a lateral discontinuity in the basement (Figure 3.6). In this case, extension resulted in the basement forming two separate half graben, separated by a lateral fault with a scissor geometry (see also Moustafa, 2002). The overlying soft clay was not cut by the lateral fault, but exhibited a through-going half graben marked by a

bend located above the basement transfer fault, and with opposite polarities on opposite sides. In this case, there was no ridge marking the transfer zone.

Comparison of Approaching, Laterally Offset and Overlapping Faults

Basement faults with approaching and overlapping relationships exhibited a fairly similar evolution and final geometry (Figure 3.7).All cases resulted in a final overlapping geometry of the fault zones, and saddle –shaped LRAZ's which made an acute angle with the fault zones in the center and curved into the footwall areas of each fault zone. This observation is in contrast to the elongate dome-shaped geometry of the transfer zone resulting from pure faulting in the models proposed by Rosendahl (1987) and Morley et al (1990). The saddle-shaped transfer zones are the result of significant drape folding immediately above master faults, which is common in all types of transfer zones.

An example of drape folding above a basement master fault was documented by Moustafa (2002) from the east central part of the Suez rift. In this area the Sinai massif fault branches into two splays, the Wadi Sidri and Hadahid faults, near its termination (Figure 3.8). These two splays delineate the boundaries of the drape folding. If drape folding is more common than previously documented in rift settings, the saddle shape of transfer zones exhibited in the models should also be expected. In addition to drape folding a gentle flexure or rollover developed in the hanging walls of the main faults. This resulted in the formation of antithetic faults in the hanging wall. Documented examples of flexure, such as from the Rusizi basin in the East African rift system (Ebinger, 1989) exhibit the formation of antithetic faults (Figure 3.9b).

The primary differences between the approaching, laterally offset, and overlapping initial geometries of basement faults were as follows. The width of the accommodation zone connecting the footwalls of the major faults was greatest in the case of approaching faults, and least for overlapping faults. The angle between the major faults and the axis of the LRAZ also decreases from approximately 45 degrees for the approaching faults to 34 degrees for the laterally offset faults, and 24 degrees for the overlapping faults. Also, interaction between the two fault zones initiated earliest in the case of overlapping faults and latest for the approaching faults.

3.5.2 Divergent Transfer Zone

Divergent transfer zones formed above basement faults with approximately the same spacing as those in convergent zones are much narrower, because the fault zones propagate towards each other during upward fault propagation (Figure 3.10). As in the case of the convergent transfer zone, the basement fault to the northwest, or closer to the moving plate, is the first to propagate upward.

Laterally Offset Faults

For laterally offset basement faults (Figure 3.11 a), initial movement results in the progressive development of a fault zone above the basement fault and the formation of a drape fold (Figures 3.12b and c). A linear trough forms at the base of the drape fold. Movement on the southern fault, results in the formation of a fault zone at the top of the soft clay when the displacement reaches 0.39 cm. A broad ridge oriented approximately ENE-WSW develops between the two fault zones. This ridge corresponds to the high-relief accommodation zone of Rosendahl (1987). The ridge is narrowest in the middle, because of the effects of drape folding.

Some of the secondary faults above the north-dipping basement fault coalesce to form a major east west fault as the displacement approaches 0.47 cm (Figure 3.11d). As the two sets of faults approach, they curve away from each other, resulting in the development of ENE-WSW trends which are displayed on the rose diagram (Figure 3.10; Figures 3.11 e and f). The curvature of faults away from each other in divergent transfer zones has been documented by Morley et al (1990) from the Lake Turkana area, in the East African rift system (Figure 3.9c). Additional displacement results in increasing displacement on both sets of faults, the development of two overlapping systems of major faults, and the progressive narrowing of the transfer zone (Figures 3.11e and f).

Comparisons of Approaching, Laterally Offset and Overlapping Faults

Initially approaching or overlapping geometries of basement faults resulted in relatively similar geometries of the transfer zones. In all cases, the transfer zone was very narrow, because for any given lateral spacing of basement faults, upward propagation of faults results in a narrower transfer zone for the divergent case (Figure 3.12). However both the approaching and laterally offset cases result in more interference between curved secondary faults which eventually propagate into the transfer zone (Figures 3.12 a and b and 3.10). On the other hand, initially overlapping basement faults exhibit more linear fault propagation defining a less faulted transfer zone connecting the two footwalls (Figures 3.12c and 3.13).There was also not a discernible change in the width or the orientation of the transfer zones among the three cases, as in the case of the convergent transfer zones, perhaps due to the very narrow transfer zone.

Many natural examples of divergent transfer zones are narrow, and approach the collinear geometry described by Morley et al (1990). In the Kivu and Rusizi basins in the East African rift system (Figures 3.9a and b), a convergent transfer zone forming the Kivu basin is immediately adjacent to a divergent transfer zone, separating the Kivu and Rusizi basin (Figure 3.9a). The convergent transfer zone is wide compared to the narrow sinuous ridge forming the divergent transfer zone.

3.5.3 Synthetic Transfer Zones

Synthetic transfer zones were modeled for basement fault cuts dipping in the same direction, with approaching, laterally offset, and overlapping initial geometries. The moving plate was pulled away in the dip direction of the faults as might be expected in a rift setting. The geometry, evolution, and the fault patterns for the initial laterally offset geometry of basement faults are presented, and the final geometries are compared for the approaching, and overlapping initial geometries.

Laterally Offset Faults

For an initially laterally offset pair of faults (Figure 3.14a), initial extension (0.14 cm displacement; Figure 3.14b) results in regions of drape folding above the basement faults, followed by the development of a zone of secondary normal faults approximately parallel to the basement faults (0.29 cm displacement; Figure 3.14c). Each fault is marked by a decrease in the fault throw towards the fault tip, resulting in synclines in the hanging wall blocks which plunge away from each other. The top of the soft clay returns to its regional position towards the moving plate so that the broad flexure that forms the syncline in the hanging wall of each fault returns to a horizontal geometry

towards the northern edge. The fault zone closer to the moving plate propagated further laterally than the more distant fault.

Increasing displacement (0.42 cm; Figure 3.14d) results in the coalescence of the secondary normal faults to form one or more laterally continuous faults. These larger faults show significant changes in trend, suggesting that they formed by the coalescence of a number of secondary en echelon faults. The major faults curve towards their dip direction near their termination. A few antithetic faults form due to the well-developed flexure in the hanging walls of both major faults. A well-defined oblique ramp trending approximately 20 degrees to the trend of the major faults connects the undeformed parts of the hanging walls of adjacent faults. Although this ramp generally slopes to the ENE, it reverses slope in the undeformed zone of the northern fault, forming an asymmetric saddle. In the final stages (0.53 cm and 0.67 cm displacement; Figure 3.14e-f), lateral propagation of the northern main fault zone forms a series of short subparallel faults, breaching the oblique ramp across its lowest area and separating the southern rollover structure from the northern one. Also, additional faults propagate into the hanging walls of previously developed major faults.

Fault patterns in the rose diagrams exhibit a dominant east west trend in the early stages of extension, but the progressive development of more WNW and ENE trends with ongoing deformation (Figure 3.14). This is primarily due to the curvature of the faults with lateral propagation along plunging synclines. The ENE trend is more dominant than the WNW trend because of the larger number and greater lengths of fault strands along the northern fault, which curve towards an ENE trend.

Comparisons of Approaching, Laterally Offset and Overlapping Faults

Initially approaching, laterally offset and overlapping basement fault geometries result in some small differences in the geometry and trend of the faults, and the transfer zone (Figure 3.15). For both overlapping and laterally offset initial basement faults, the fault closer to the moving plate exhibited greater lateral propagation, and therefore a larger overlap of the major faults (Figure 3.15). In the approaching case, the fault closer to the moving plate also propagated farther, but the degree of overlap was less. The fault tips also showed significant curvature closer to the transfer zone.

All cases showed fault patterns with both WNW and ENE trends due to the curvature of the faults in the direction of propagation. Because of the greater propagation of the northern fault the ENE trend was more dominant than the WNW trend. The transfer zones showed a reversal in slope and were generally narrower at their lowest point. A number of south dipping antithetic faults developed during the formation of the rollover flexure in the hanging walls of all structures.

The basement configuration of the faults in the stiff clay (Figure 3.16a) is very similar in geometry to the model documented by Morley et al (1990), and to many of the surface and subsurface examples cited in the literature. This is because the stiff clay does not develop any drape folding or secondary faults. The primary differences for the geometry of the top of the soft clay are the additional component of drape folding and secondary faulting that results in a progressive, rather than abrupt change in the slope of the ramp (Figure 3.16b), and the reversal in slope of the oblique ramp. The hanging walls of the faults return to their regional positions both laterally and longitudinally from the major faults. Therefore, the northern block is at approximately the same regional level as the footwall of the southern block. Most conceptual models and natural

examples of synthetic transfer zones show a progressive downward drop of the blocks in the dip direction resulting in relay ramps with a single slope (Morley et al, 1990; Larsen, 1988). This results if there is a progressive downward drop of structures into the basin, or if there is a regional slope that is in the same direction as the dip direction of the faults, both of which are common in many basins.

3.6 Discussion and Conclusions

The experiments provide some important insights regarding the geometry of transfer zones and the evolution and interference of the faults with progressive evolution. Many of the features of the models closely resemble previous classifications of transfer zones (Rosendahl, 1987; Morley et al, 1990). However, more details regarding the structural geometries and fault patterns were obtained from the mapping and fault analysis. The experimental models also show some significant differences with the conceptual models. Some of the key similarities and differences are discussed below.

For any given lateral spacing of basement faults, the transfer zones in the overlying sedimentary cover are narrower for divergent than for convergent transfer zones. Because the faults dip away from each other in divergent zones, the upward propagation of the basement faults into the overlying sedimentary units results in narrowing of the area between the two faults, whereas convergent transfer zones show an increase in the spacing between the faults. Therefore, many divergent transfer zones are narrow, and approach the collinear geometry described by Morley et al (1990). This effect is observed in the Kivu and Rusizi basins in the East African rift system, where a convergent transfer zone forming the Kivu basin is immediately adjacent to a divergent

transfer zone, separating the Kivu and Rusizi basin. The convergent transfer zone is wide compared to the narrow sinuous ridge forming the divergent transfer zone. The spacing is approximately constant for synthetic transfer zones.

In convergent, divergent, and synthetic transfer zones, initial configurations of approaching, laterally offset, and overlapping all result in overlap of the fault zones in the cover. The difference is in the degree of overlap, and in some cases, the resulting width of the transfer zone. Typically, broader and narrower transfer zones are indicative of initially approaching and overlapping geometry of the underlying basement faults, respectively. The effects are most apparent in convergent transfer zones, for which both the width and the orientation of the transfer zone indicate the initial basement fault configurations. Secondary faults on the cover units show more of linear lateral fault propagation for initially overlapping basement faults. Lateral propagation of the secondary faults in a curved path is indicative of an initially approaching geometry of the basement faults.

The lateral propagation of the major faults results in interference of the secondary faults. Typically, the faults curve in their direction of dip where they terminate. Therefore the curvatures of the secondary faults towards each other, away from each other or in the same direction are indicative of convergent, divergent and synthetic transfer zone geometry of the underlying basement faults, respectively. These observations are in agreement with conceptualized models and related examples of real transfer zones (Morley et al, 1990). With continued displacement, new faults propagate laterally and also curve inward, resulting in a series of en echelon faults with curved geometries.

The hanging walls of the faults are marked by a gentle flexure or rollover into the fault, with the amount of flexure increasing with fault throw away from the fault tip. The propagation of the faults from the stiff to the soft clay results in upward steepening of the fault. Downward movement of the hanging wall through the downward shallowing fault is the primary cause of the flexure in the hanging wall. Significant rollover also results in the formation of antithetic faults which accommodate the formation of the flexure. This is apparent in the experimental models and has also been documented in natural examples, such as in the Kivu and Rusizi basins (Ebinger, 1989).

A primary difference with schematic models is the significant component of extensional fault propagation folding (drape folding), accompanied by a zone of secondary faulting within the sedimentary cover in the early stages of fault propagation. Eventually one or more of the faults break through the entire cover as major faults. Therefore, all three types of transfer zones are characterized by significant folding and related variations in the shapes of structures. The transfer zones are marked by a progressive change in relief from the footwall to the hanging wall. Although the effects of drape folding have been documented both in experiment and conceptual models (Withjack et al, 1995; Schlische, 1995), as well as in subsurface examples (Scott and Rosendahl, 1989), its effects have not been incorporated in conceptual models of transfer zones. The experimental models demonstrate the difference in geometry resulting from the effects of drape folding. Transfer zones are believed to be important location for the development of hydrocarbon traps in rift basins. Therefore, the differences in geometry would be important in subsurface interpretation in areas with poor data quality, and in mapping potential prospects involving structural traps in rift basins.

Figures

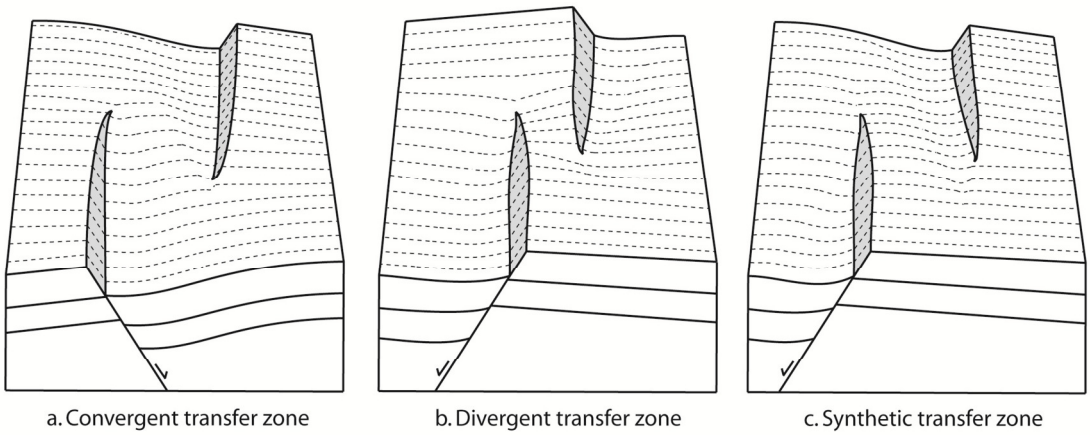

Figure 3.1 Common transfer zone geometries in rift systems. a. Convergent transfer zone. b. Divergent transfer zone. c. Synthetic transfer zone (based on Morley et al., 1990 and Bose and Mitra, 2010).

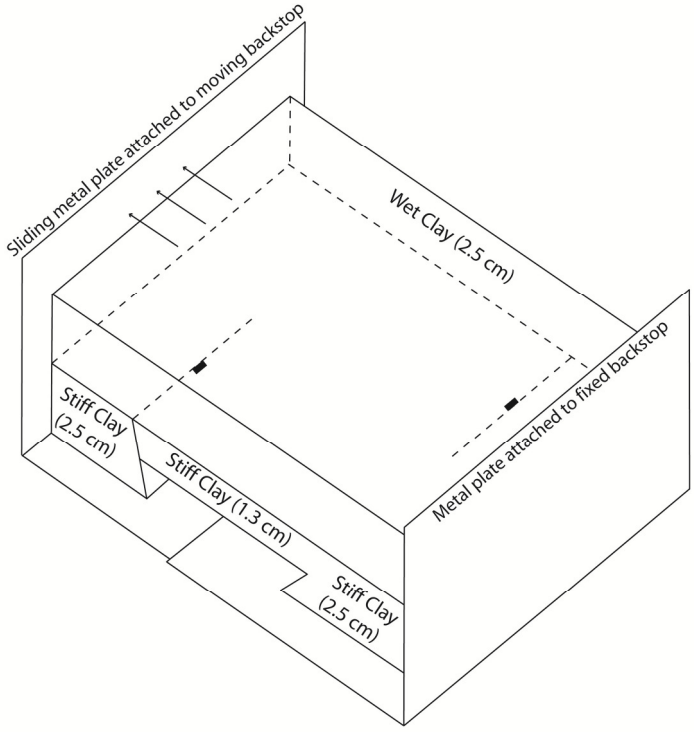

Figure 3.2 Oblique view of the experimental setup showing the configuration of the base plates, the moving and fixed backstops, and the stiff and soft clay, which represent the basement and overlying sedimentary cover. Pre-existing cuts in the stiff clay represent preexisting basement faults which propagate both laterally and upwards through the soft clay with extension.

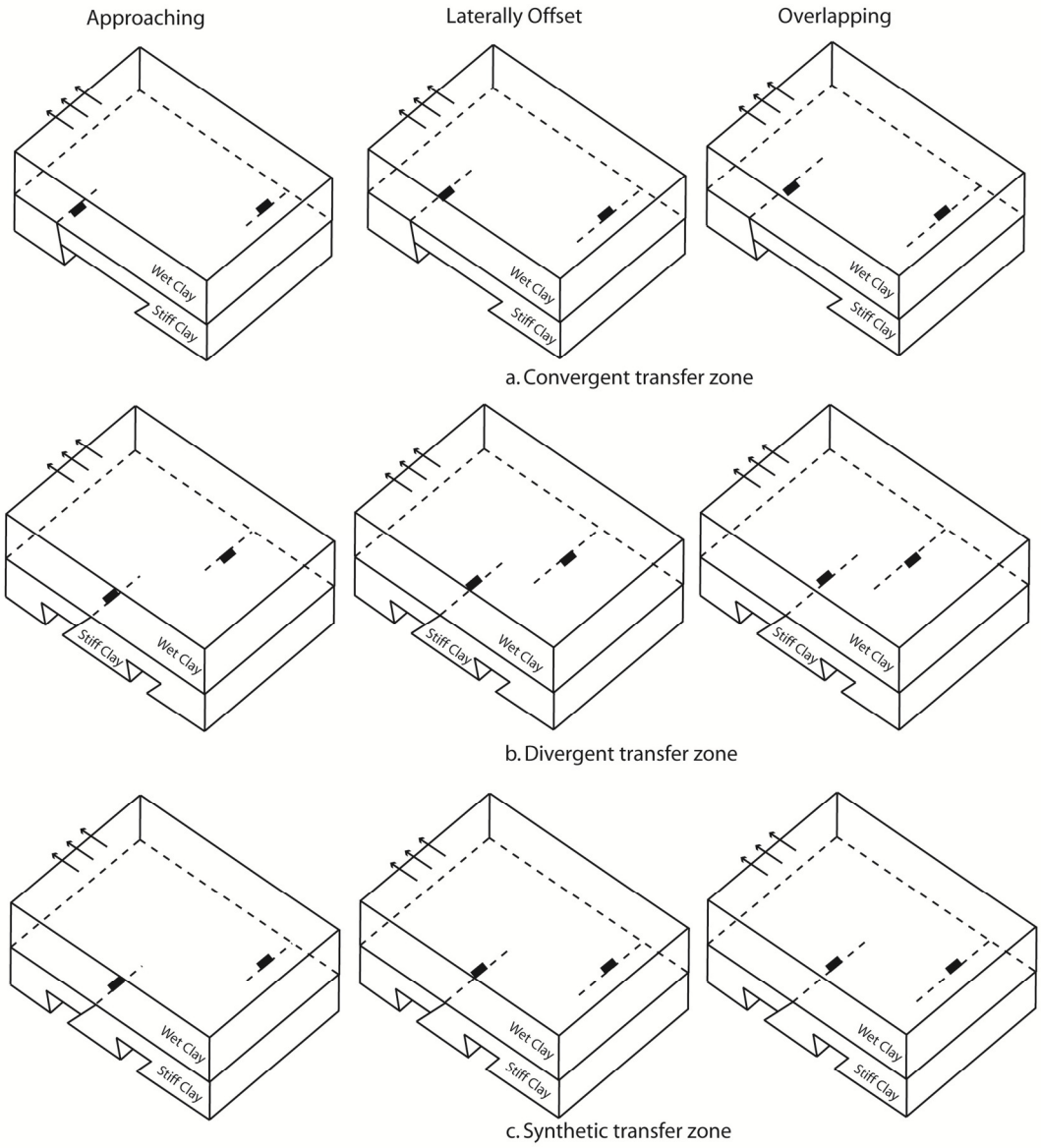

Figure 3.3 Oblique view of the experimental configurations used to model (a) convergent, (b) divergent, and (c) synthetic transfer zones. For each type of transfer zone, cuts in the stiff clay representing initially approaching, laterally offset, and overlapping geometries were modeled. The overlying soft clay, representing the sedimentary cover, did not have any pre-existing faults.

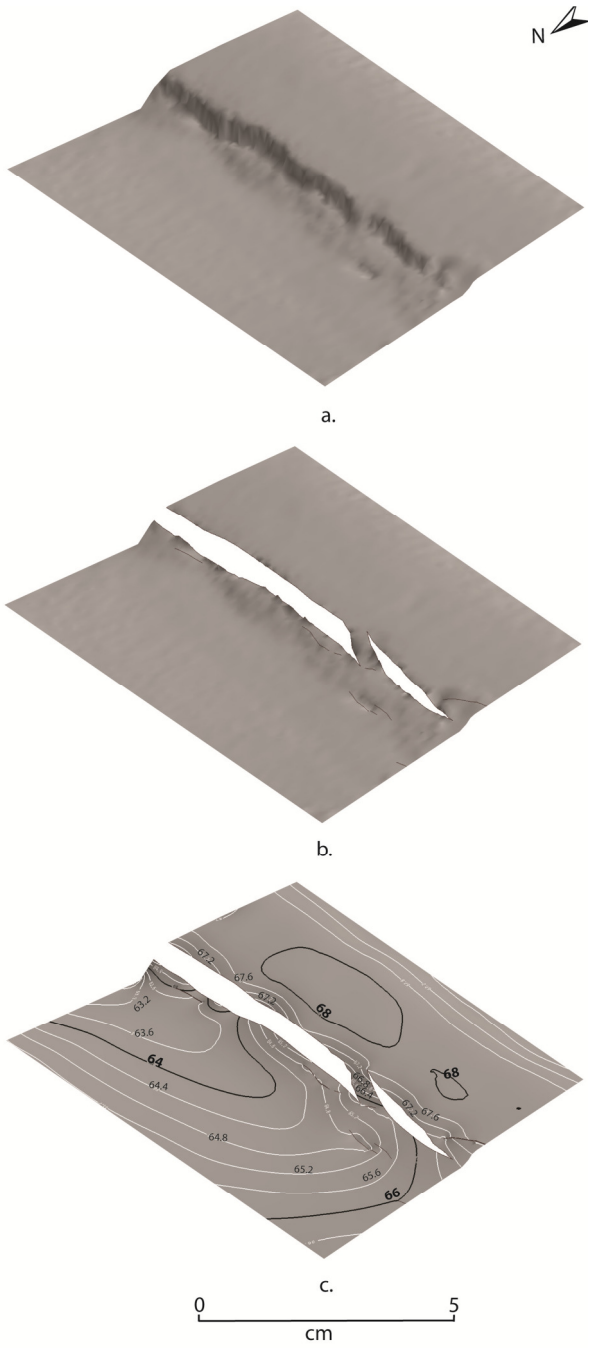

Figure 3.4 Method of incorporating faults in mapped 3-D surfaces. a. Unsmoothed surface modeled from point cloud obtained by laser scanning showing fault escarpment. b. Fault cuts based on sharp changes in relief on the modeled surface and comparison with digitized faults on photographs. c. Final smoothed faults and contoured surface incorporating fault cuts. Contour interval for this display is 0.4 mm.

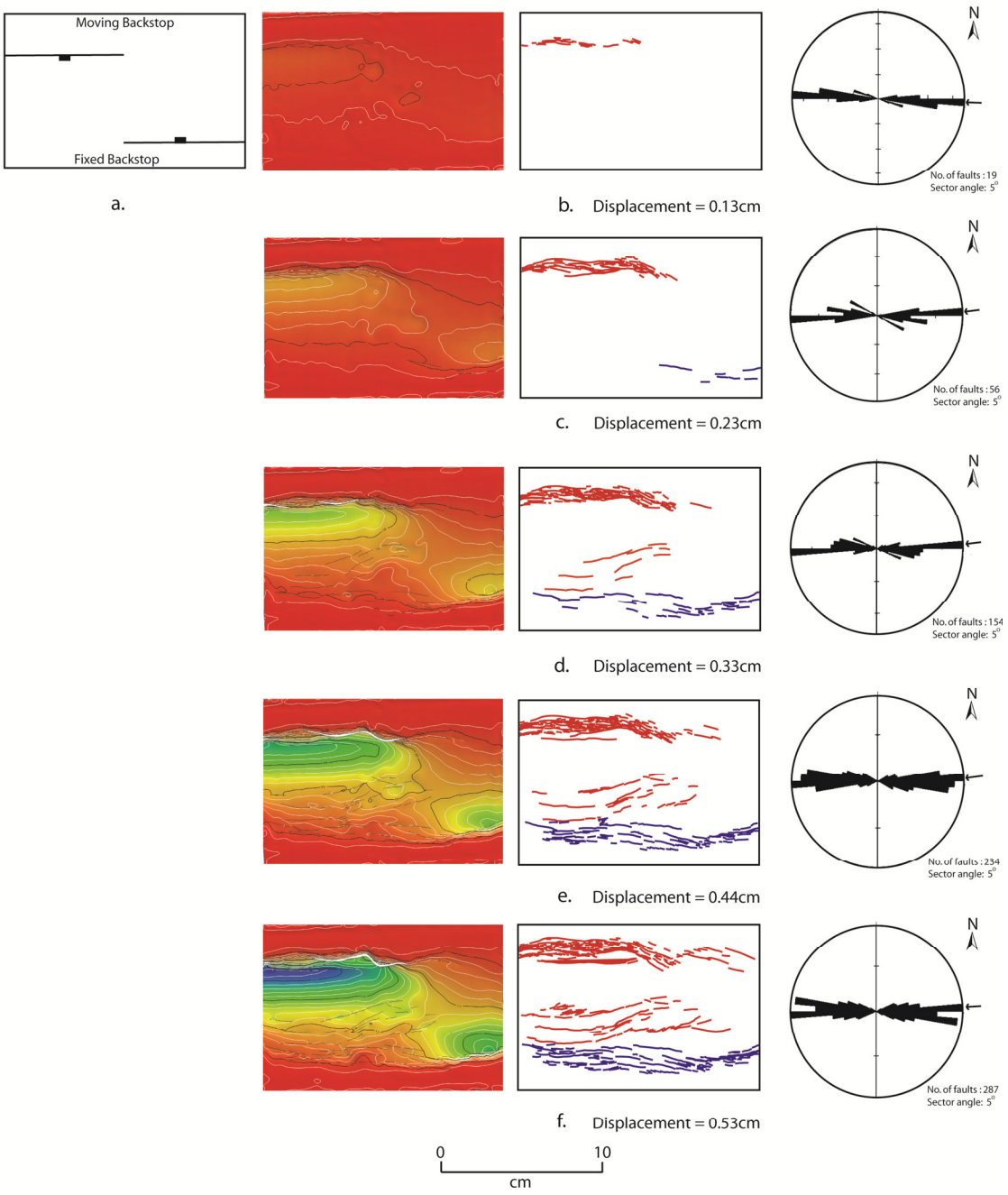

Figure 3.5 Progressive evolution of structural geometries and fault patterns in map view for a convergent transfer zone, with two pre-existing laterally offset faults dipping towards each other. Moving plate is towards the north. a. Initial fault geometry in stiff clay. b-f. Contoured structure map, fault patterns and fault orientations for the top of the soft clay, with progressive evolution. On the contoured structure map, red and yellow indicate high elevations and blue and green represent low elevations. North dipping faults are shown in blue and south dipping faults are shown in red on the fault map. Displacements of moving plate are 0.13 cm (b), 0.23 cm (c), 0.33 cm (d), 0.44 cm (e), and 0.53 cm (f). Rose diagrams show main orientations of faults measured. Bars show percentage of total length of faults for each orientation. An arbitrary North arrow is assigned as a reference to describe orientations of faults.

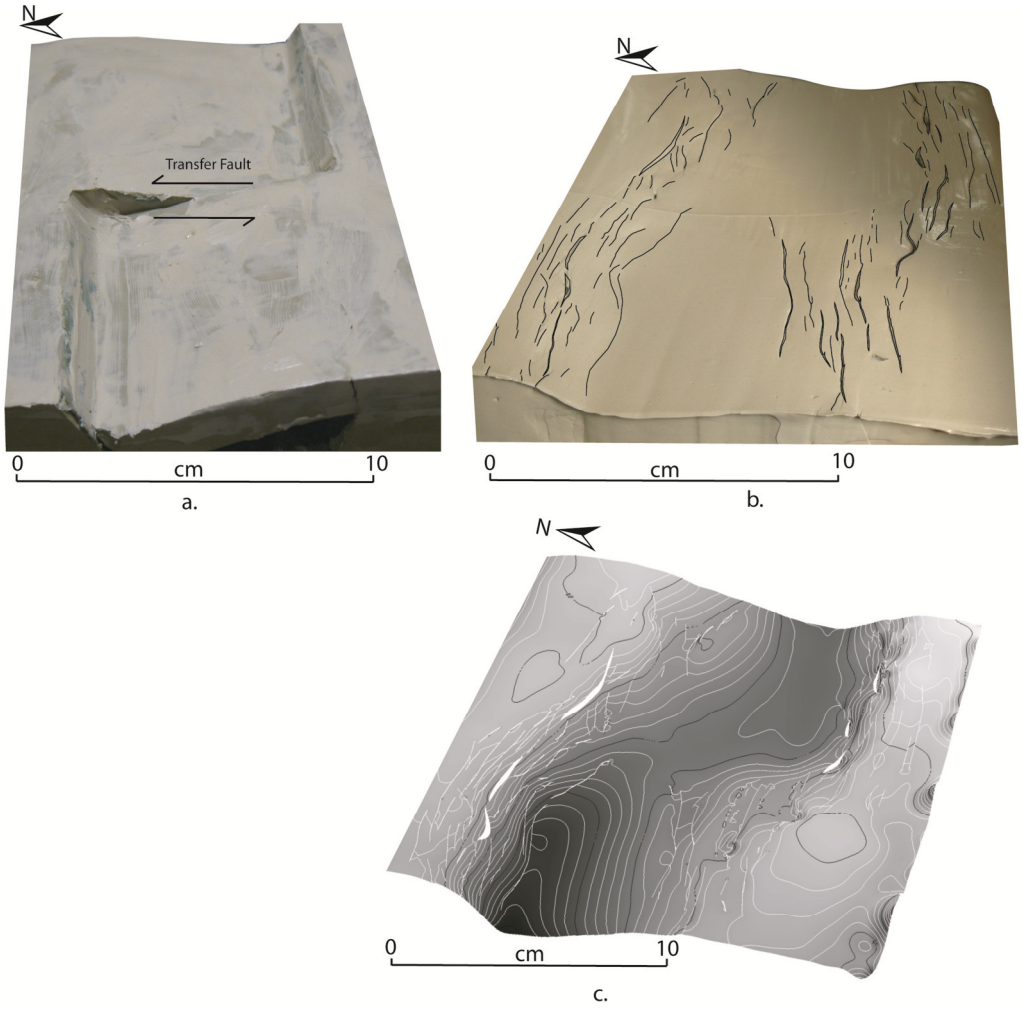

Figure 3.6 Oblique view of top of stiff clay with two major faults dipping towards each other, forming a convergent transfer zone, and connected by a lateral transfer fault. Photograph taken at end of experiment after removal of soft clay. b. Oblique photograph of the top of soft clay for the same stage as (a) showing a through-going graben without any expression of the lateral fault at the surface. c. Oblique view of the modeled surface of the top of the soft clay showing the opposite polarity of the half graben on either side of the lateral transfer fault. Vertical exaggeration is 2:1.

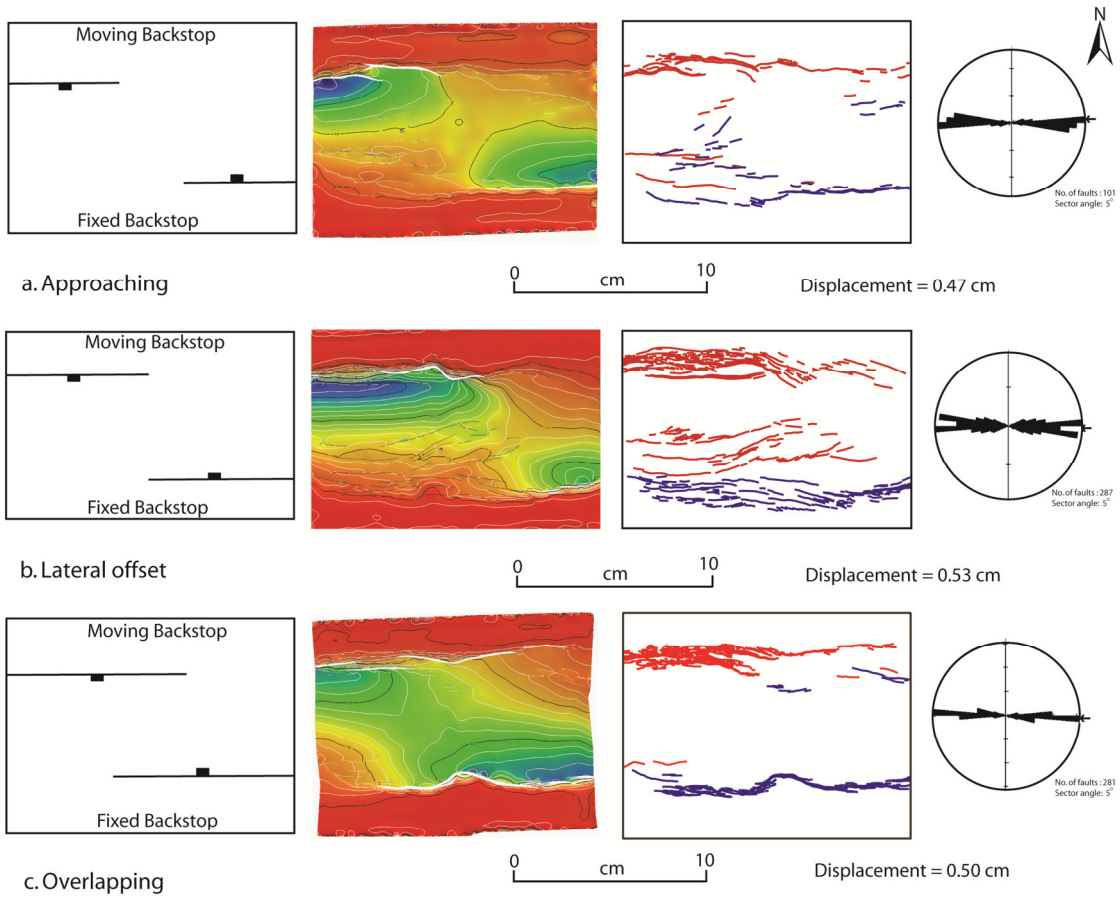

Figure 3.7 Comparison of final structural geometries, fault patterns and fault orientations for the top of the soft clay for convergent transfer zones with initially (a) approaching, (b) laterally offset, and (c) overlapping fault geometries in the stiff clay. The stages of deformation compared all have approximately the same total displacement. On the contoured structure map, red and yellow indicate high elevations and blue and green represent low elevations. North-dipping faults are shown in blue and south dipping faults are shown in red on the fault map. Rose diagrams show main orientations of faults measured. Bars show percentage of total length of faults for each orientation. An arbitrary North arrow is assigned as a reference to describe orientations of faults.

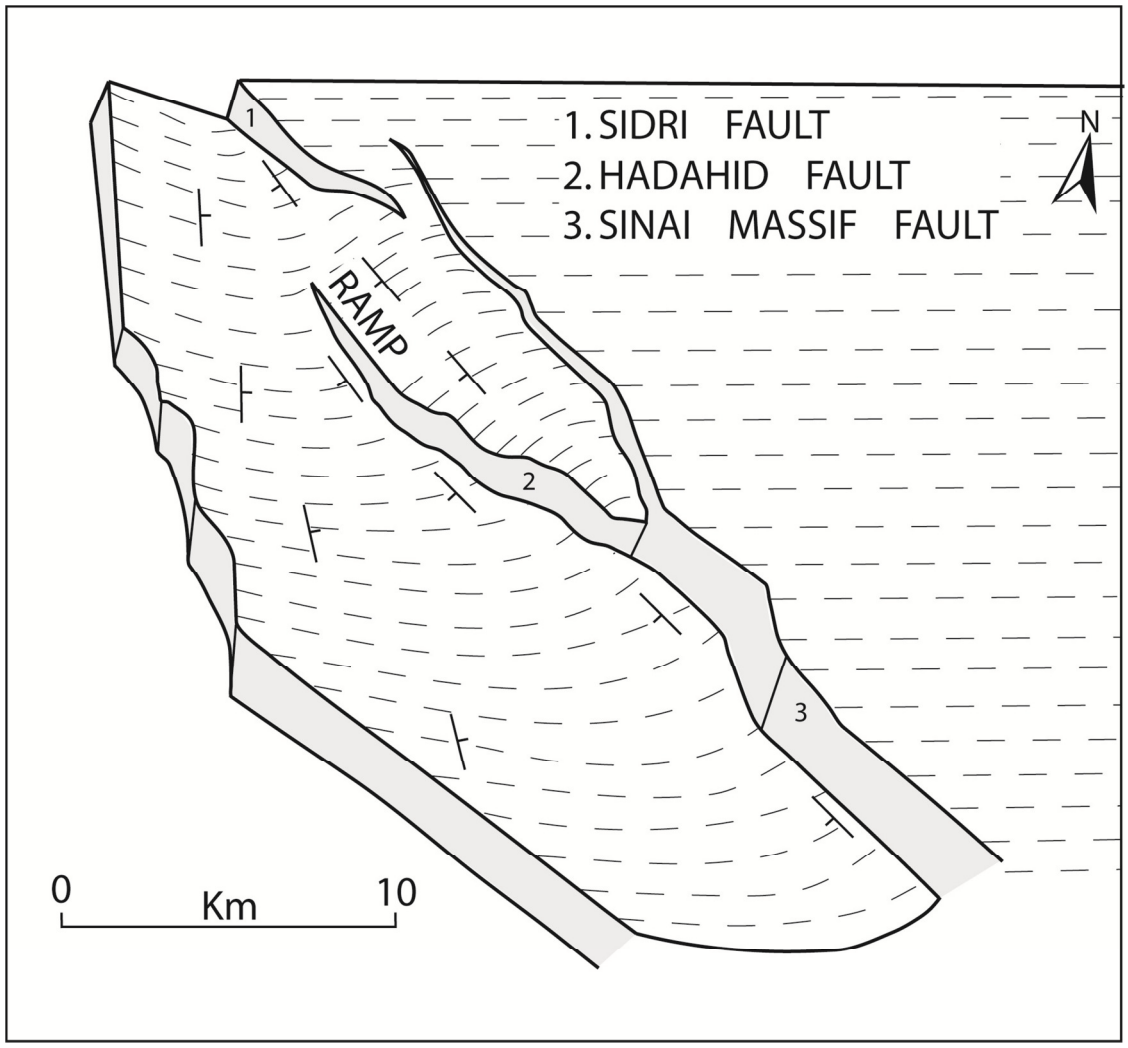

Figure 3.8 Schematic diagram showing extensional fault-propagation (drape) folding along a major fault zone in the east central part of the Gulf of Suez rift. The Sinai Massif fault branches into two splays, the Wadi Sidri and Hadahid faults, near its termination, delineating the boundaries of the drape folding (modified from Moustafa, 2002).

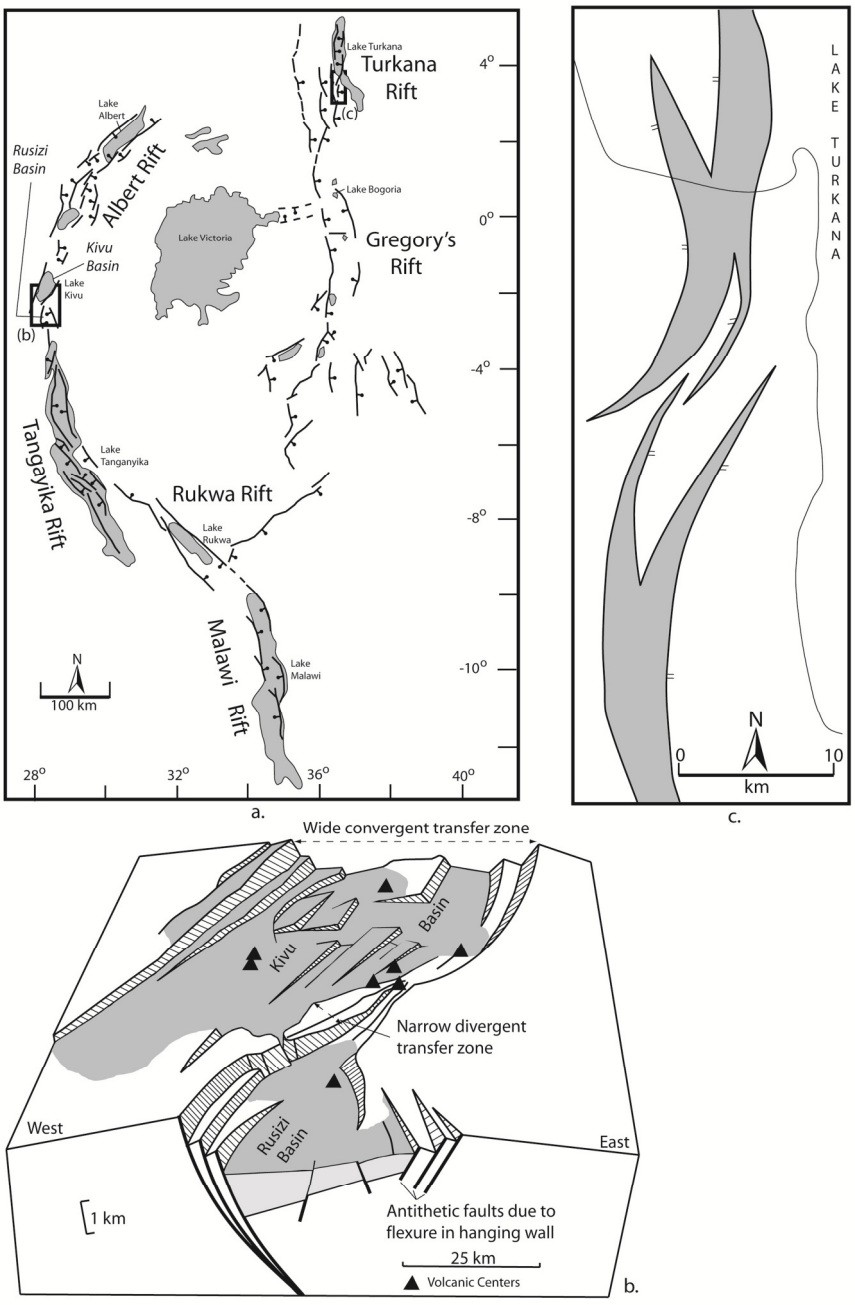

Figure 3.9 a. Map of part of the East African rift system showing a number of transfer zones between mapped faults (modified from Morley et al, 1990). Boxed areas show locations of detailed figures in b and c. b. Schematic diagram (not to scale) showing the formation of synthetic and antithetic faults in a convergent transfer zone in the Rusizi basin (modified from Ebinger, 1989). Note the narrow divergent transfer zone immediately south of the broader convergent transfer zone. c. Complex divergent transfer zone showing the curvature of faults away from each other as they approach (modified from Morley et al, 1990).

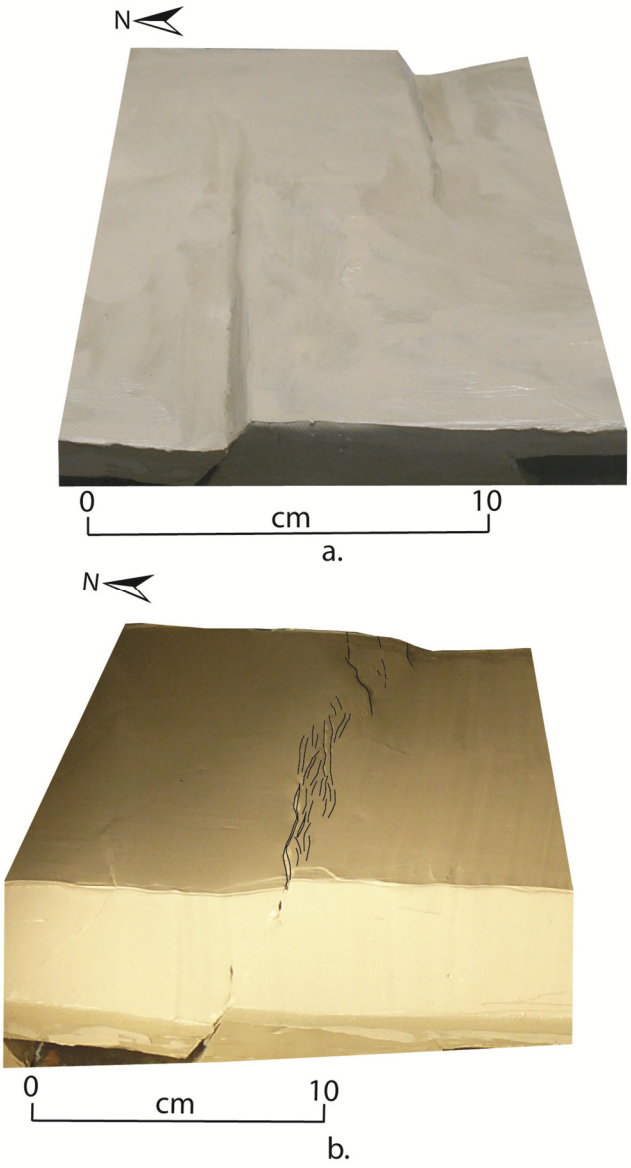

Figure 3.10 Oblique photograph showing the top of the stiff clay for a divergent transfer zone with an initial laterally offset geometry. Photograph taken at end of experiment after removal of soft clay. b. Oblique photograph showing the top of the soft clay for the same experiment showing a narrow transfer zone with a number of en echelon curved faults along the major fault terminations.

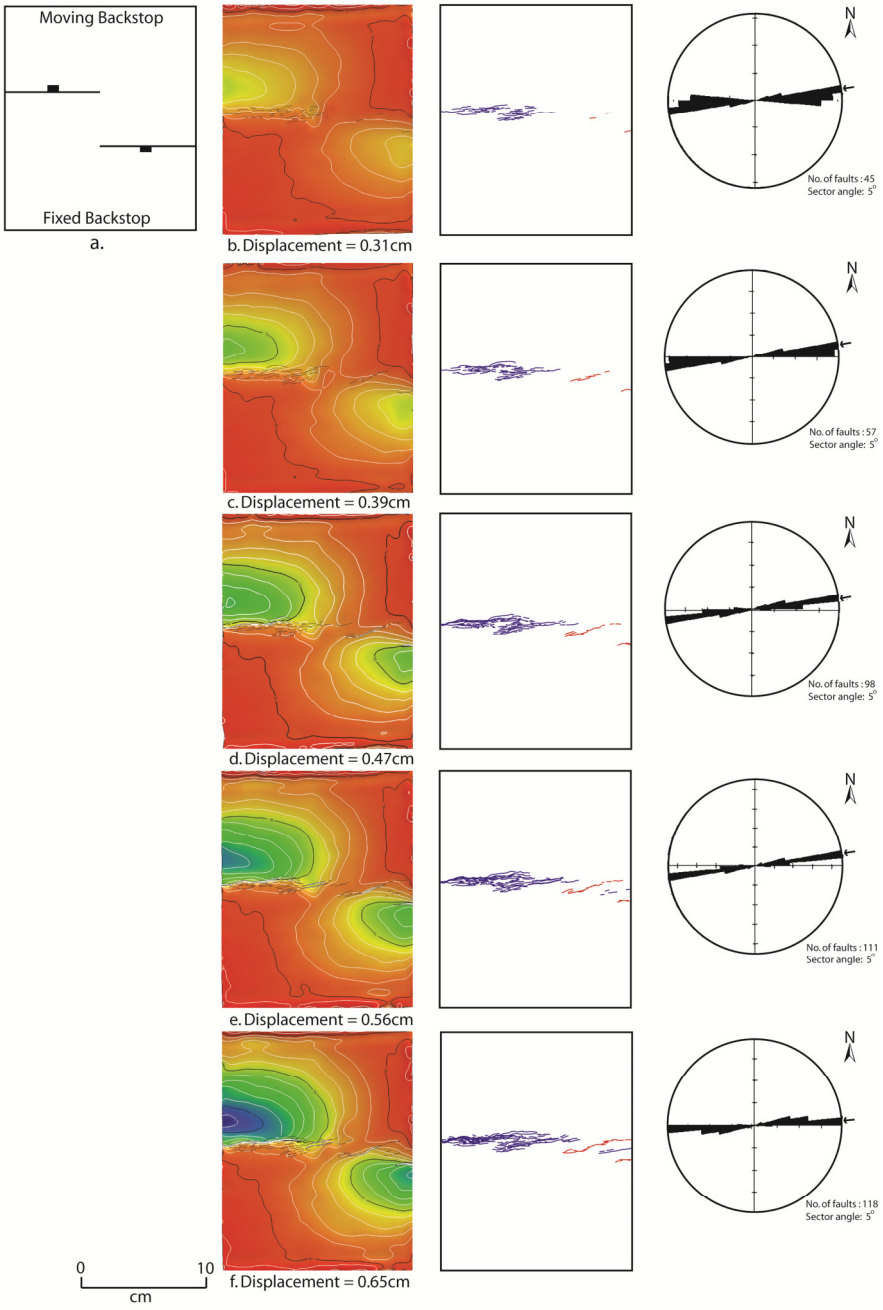

Figure 3.11 Progressive evolution of structural geometries and fault patterns in map view for a divergent transfer zone, with two pre-existing laterally offset faults dipping away from each other. Moving plate is towards the north. a. Initial fault geometry in stiff clay. b-f. Contoured structure map, fault patterns and fault orientations for the top of the soft clay, with progressive evolution. Displacements of moving plate are, 0.31 cm (b), 0.39 cm (c), 0.47 cm (d), and 0.56 cm (e), and 0.65 cm (f). Note the narrow divergent transfer zone at the top of the soft clay compared to the width of the transfer zone at the top of the stiff clay. On the contoured structure map, red and yellow indicate high elevations and blue and green represent low elevations. North dipping faults are shown in blue and south dipping faults are shown in red on the fault map. Rose diagrams show main orientations of faults measured. Bars show percentage of total length of faults for each orientation. An arbitrary North arrow is assigned as a reference to describe orientations of faults.

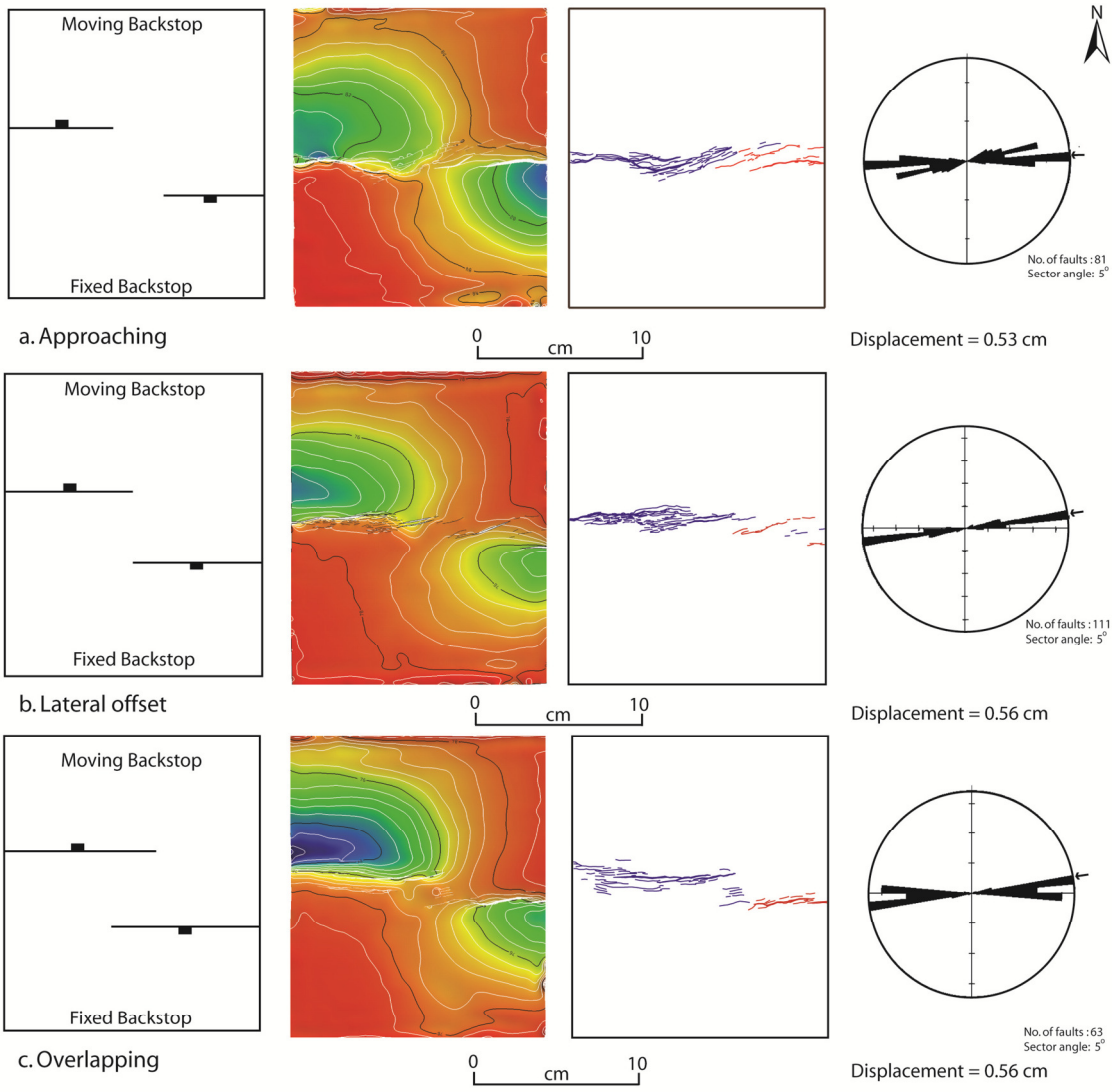

Figure 3.12 Comparison of final structural geometries, fault patterns and fault orientations for the top of the soft clay for divergent transfer zones with initially (a) approaching, (b) laterally offset, and (c) overlapping fault geometries in the stiff clay. The stages of deformation compared all have approximately the same total displacement. On the contoured structure map, red and yellow indicate high elevations and blue and green represent low elevations. North dipping faults are shown in blue and south dipping faults are shown in red on the fault map. Rose diagrams show main orientations of faults measured. Bars show percentage of total length of faults for each orientation. An arbitrary North arrow is assigned as a reference to describe orientations of faults.

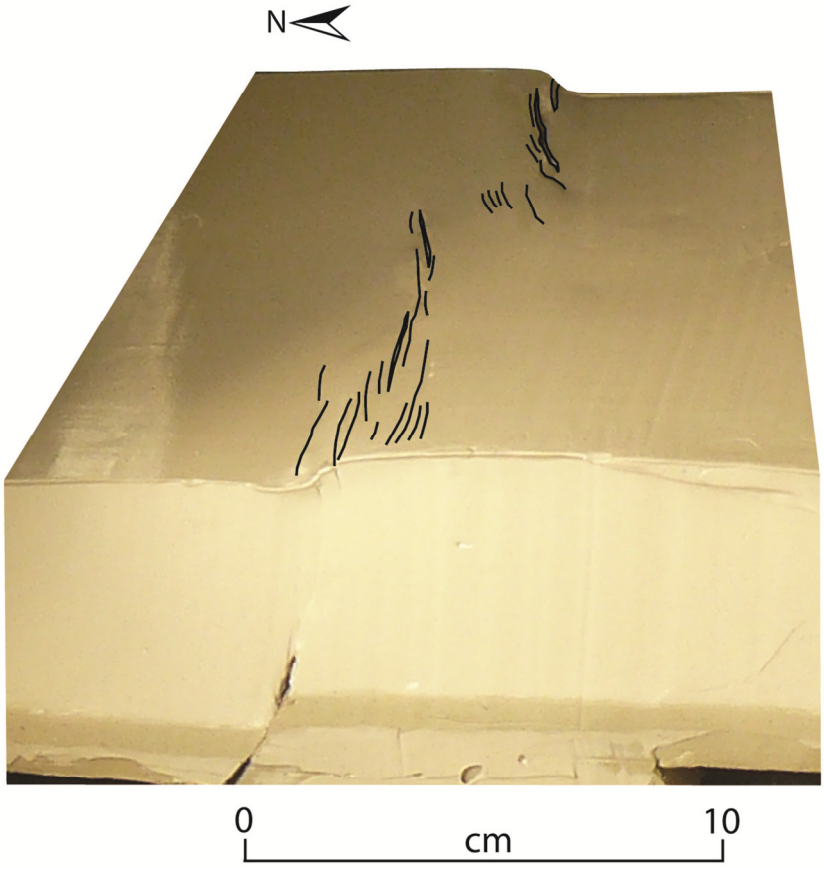

Figure 3.13 Oblique photograph of the top of the soft clay for a divergent transfer zone with initially overlapping faults in the stiff clay. In this case a well-defined ramp separated by linear faults on either side marks the transfer zone (compare with Figure 10b).

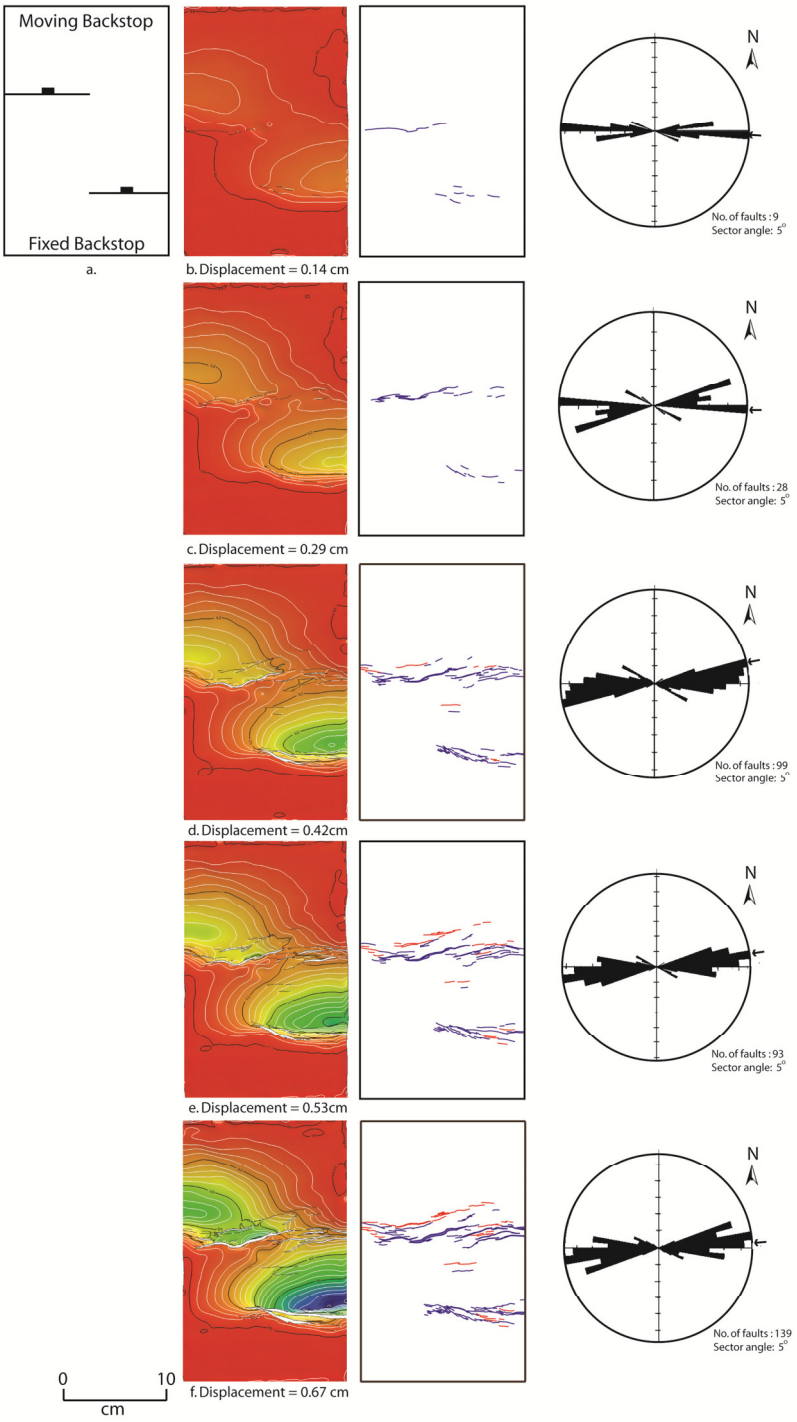

Figure 3.14 Progressive evolution of structural geometries and fault patterns in map view for a synthetic transfer zone, with two pre-existing laterally offset faults dipping in the same direction. Moving plate is towards the north. a. Initial fault geometry in stiff clay. b-f. Contoured structure map, fault patterns and fault orientations for the top of the soft clay, with progressive evolution. Displacements of moving plate are 0.14 cm (b), 0.29 cm (c), 0.42 cm (d), 0.53 cm (e), and 0.67 cm (f). On the contoured structure map, red and yellow indicate high elevations and blue and green represent low elevations. North dipping faults are shown in blue and south dipping faults are shown in red on the fault map. Rose diagrams show main orientations of faults measured.

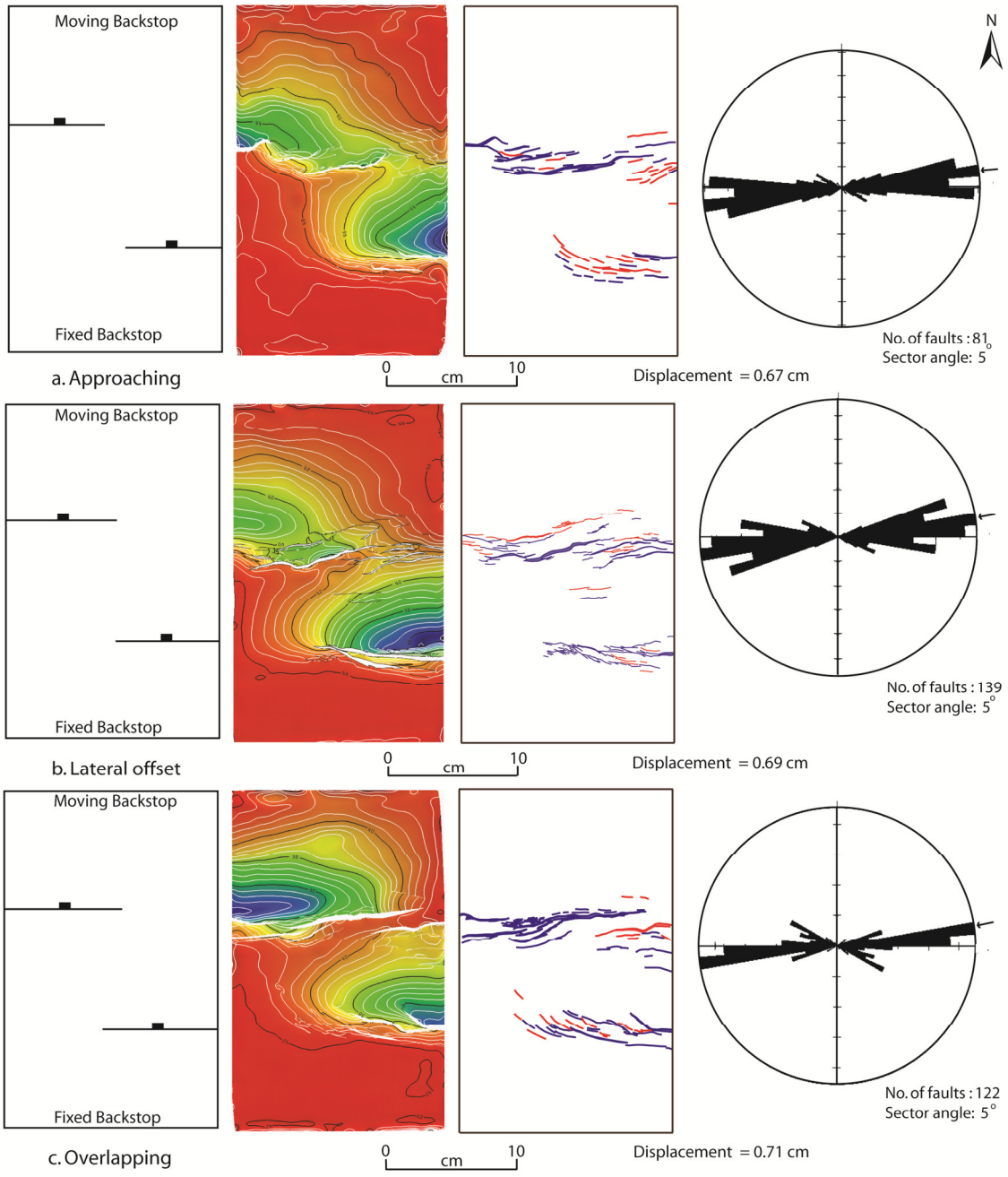

Figure 3.15 Comparison of final structural geometries, fault patterns and fault orientations for the top of the soft clay for synthetic transfer zones, with initially (a) approaching, (b) laterally offset, and (c) overlapping fault geometries in the stiff clay. The stages of deformation compared all have approximately the same total displacement. On the contoured structure map, red and yellow indicate high elevations and blue and green represent low elevations. North dipping faults are shown in blue and south dipping faults are shown in red on the fault map. Rose diagrams show main orientations of faults measured. Bars show percentage of total length of faults for each orientation. An arbitrary North arrow is assigned as a reference to describe orientations of faults.

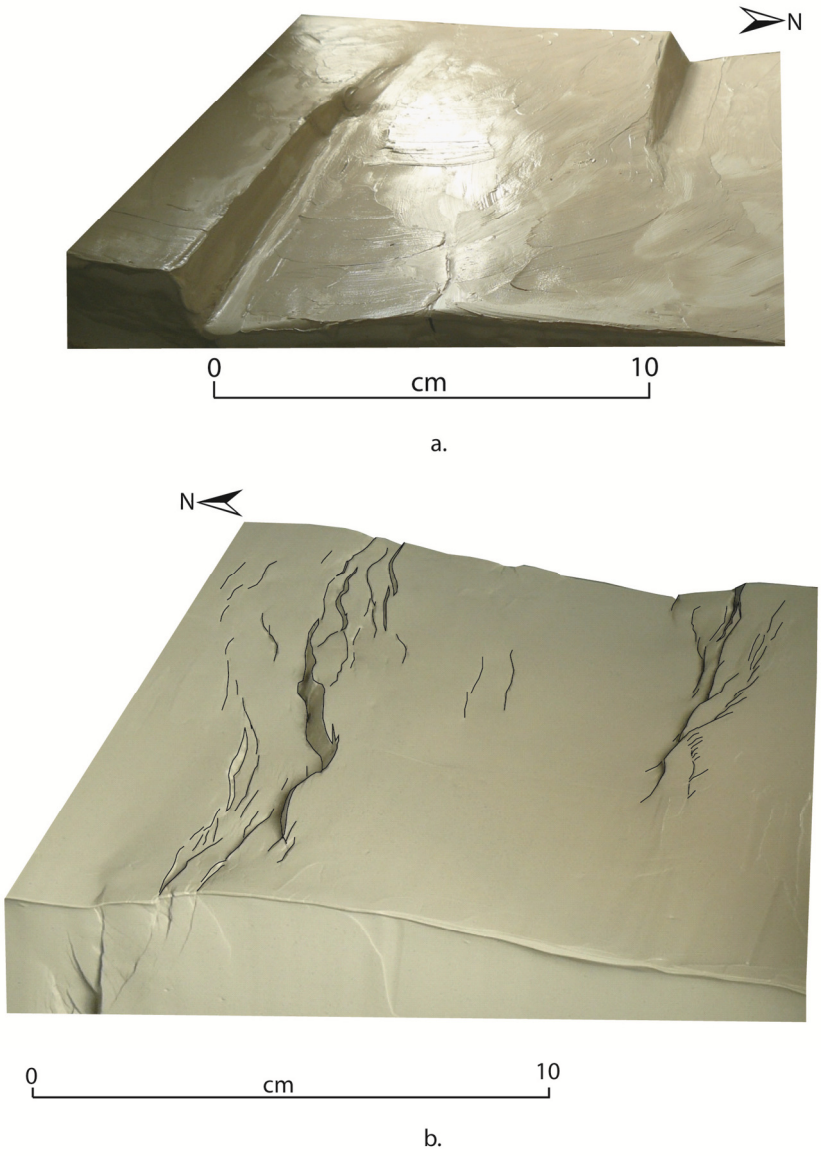

Figure 3.16 Oblique photographs of clay models of synthetic transfer zones for laterally offset pre-existing basement faults. a. Top of stiff clay after removal of soft clay at the end of the experiment, showing two major faults separated by an oblique ramp. View looking west. b. Top of soft clay showing a more subtle oblique ramp separating two fault zones, with associated drape folding. View looking east.

References

Athmer, W. and S. M. Luthi, 2011, The effect of relay ramps on sediment routes and deposition: A review: Sedimentary Geology, v.242, no.1-4, p.1-17, doi:10.1016/j.sedgeo.2011.10.002.

Bose, S., and S. Mitra., 2010, Analog modeling of divergent and convergent transfer zones in listric normal fault systems: AAPG Bulletin, v.94, p.1425-1452.

Childs, C., J. Watterson and J. J. Walsh, 1995, Fault overlap zones within developing normal faults: Journal of the Geological Society, v.152, no.3, p.535-549.

Crider, J. G., 2001, Oblique slip and geometry of normal-fault linkage: mechanics and a case study from the Basin and Range in Oregon: Journal of Structural Geology, v.23, no.12, p.1997-2009.

Crider, J. G., and D. D. Pollard, 1998, Fault linkage: three dimensional mechanical interactions between echelon normal faults: Journal of Geophysical Research, v.103, no.B10, p.24373-24391.

Ebinger, C. J., 1989, Geometric and kinematic development of border faults and accommodation zones, Kivu-Rusizi Rift, Africa: Tectonics, v.8, no.1, p.117-133.

Faulds, J. E. and R. J. Varga, 1998, The role of accommodation zones and transfer zones in the regional segmentation of extended terranes *in* Faulds, J. E. and J. H. Stewart eds., Accommodation zones and transfer zones; the regional segmentation of the Basin and Range Province: Special Paper-Geological Society of America, v.323, p.1-45.

Fossen, H., R. A. Schultz, E. Rundhovde, A. Rotevatn, S. J. Buckley, 2010, Fault linkage and graben stepovers in the Canyonlands (Utah) and the North Sea Viking

Graben, with the implications for hydrocarbon migration and accumulation: AAPG Bulletin, v. 94, no.5, p.597-613, doi:10.1306/10130909088.

Gawthorpe, R. L. and J. M. Hurst, 1993, Transfer zones in extensional basins: their structural style and influence on drainage development and stratigraphy: Journal of the Geological Society, v.150, no.6, p.1137-1152.

Gupta, A. and C. H. Scholz, 2000, A model of normal fault interaction based on observations and theory: Journal of Structural Geology, v.22, no.7, p.865-879.

Gupta, S., P. A. Cowie, N. H. Dawers, and J. R. Underhill, 1998, A mechanism to explain rift basin subsidence and stratigraphic patterns through fault array evolution: Geology, v.26, no.7, p.595-598.

Horsfield, W. T., 1977, An experimental approach to basement-controlled faulting: Geologie en Mijnbouw, v.56, p.363-370.

Huggins, P., J. Waterson, J. J. Walsh, C. Childs, 1995, Relay zone geometry and displacement transfer between normal faults recorded in coal-mine plans: Journal of Structural Geology, v.17, no.12, p.1741-1755.

Jin, G. and R. Groshong, 2006, Trishear kinematic modeling of extensional fault-propagation folding: Journal of Structural Geology, v. 28, p. 170-183.

Larsen, P., 1988, Relay structures in a Lower Permian basement-involved extension system, East Greenland: Journal of Structural Geology, v.10, no.1, p.3-8.

Le Calvez, J. H. and B. C. Vendeville, 2002, Physical modeling of normal faults and graben relays above salt: A qualitative and quantitative analysis *in* Dutton, S. P., S. C. Ruppel and T. F. Hentz eds., Transactions – Gulf Coast Association of Geological Societies, v.52, p.599-606.

McClay, K. R. and M. J. White, 1995, Analogue modeling of orthogonal and oblique rifting: Marine and Petroleum Geology, v.12, no.2, p.137-151.

McClay, K. R., T. Dooley, P. Whitehouse and M. Mills, 2002, 4-D evolution of rift systems: Insights from scaled physical models: AAPG Bulletin, v.86, no.6, p.935-959.

Miller J. F. and S. Mitra, 2011, Deformation and secondary faulting associated with basement-involved compressional and extensional structures: American Association of Petroleum Geologists Bulletin, v. 95. No.4, p. 675-689.

Mitra, S. and D. Paul, 2011, Structural geometry and evolution of releasing and restraining bends: Insights from laser-scanned experimental models: AAPG Bulletin, v. 95, no. 7, p. 1147-1180.

Moore, J. M. and R. A. Schultz, 1999, Process of faulting in jointed rocks of Canyonlands National Park, Utah: GSA Bulletin, v.111, no.6, p.808-822.

Morley, C. K., R. A. Nelson, T. L. Patton and S. G. Munn, 1990, Transfer zones in the east African rift system and their relevance to hydrocarbon exploration in rifts: AAPG Bulletin, v. 74, no.8, p.1274-1253.

Moustafa, A. R., 2002, Controls on the geometry of transfer zones in the Suez Rift and northwest Red Sea: Implications for the structural geometry of the rift systems: AAPG Bulletin, v.86, no.6, p.979-1002.

Nelson, R. A., T. L. Patton, and C. K. Morley, 1992, Rift-segment interaction and its relation to hydrocarbon exploration in continental rift systems: AAPG Bulletin, v.76, no.8, p.1153-1169.

Paul, D. and S. Mitra, 2012, Controls of basement faults on the geometry and evolution of basement-involved compressive structures: AAPG Bulletin, v.96, no.10, p.1899-1930.

Peacock, D.C.P., and D. J. Sanderson, 1991, Displacements, segment linkage and relay ramps in normal fault zones: Journal of Structural Geology, v.13, no.6, p.721-733.

Rosendahl, B. R., 1987, Architecture of continental rifts with special reference to East Africa: Annual Review of Earth and Planetary Sciences, v.15, p.445-503.

Sanford, A. R., 1959, Analytical and experimental study of simple geologic structures: GSA Bulletin, v.70, p.19-52, doi:10.1130/0016-7606(1959)70[19:AAESOS]2.0.CO;2.

Scott, D. L. and B. R. Rosendahl, 1989, North Viking Graben: An east African perspective: AAPG Bulletin, v.73, no.2, p.155-165.

Serra, S. and R. A. Nelson, 1988, Clay modeling of rift asymmetry and associated structures: Tectonophysics, v.153, no.1-4, p.307-312, doi.org/10.1016/0040-1951(88)90023-6.

Schlische, R. W., 1995, Geometry and origin of fault-related faults in extensional settings: AAPG Bulletin, v.79, no.11, p.1661-1678.

Trudgill, B. and J. Cartwright, 1994, Relay ramp forms and normal fault linkages: GSA Bulletin, v.106, no. 9, p.1143-1157.

Withjack, M. O. and W. R. Jamison, 1986, Deformation produced by oblique rifting: Tectonophysics, v.126, no.2-4, p.99-124.

Withjack, M. O., J. Olson and E. Peterson, 1990, Experimental models of extensional forced folds: American Association of Petroleum Geologists Bulletin, v. 74, no. 7, p. 1038-1054.

Withjack, M. O., Q. T. Islam and P. R. La Pointe, 1995, Normal faults and their hanging wall deformation: An experimental study: AAPG Bulletin, v.79, no.1, p.1-18.

Withjack, M. O. and S. Callaway, 2000, Active normal faulting beneath a salt layer: An experimental study of deformation patterns in the cover sequence: American Association of Petroleum Geologists Bulletin, v. 84, no. 5, p. 627-651.

Younes, A. I. and K. McClay, 2002, Development of accommodation zones in the Gulf of Suez-Red Sea rift, Egypt: AAPG Bulletin, v.86, no.6, p.1003-1026.

CHAPTER 4
FAULT EVOLUTION AND ROLE OF SALT IN DECOUPLING EXTENSIONAL DEFORMATION IN THE SMØRBUKK AREA OF THE HALTEN TERRACE, OFFSHORE MID-NORWAY: INSIGHTS FROM 3-D SEISMIC INTERPRETATION AND STRUCTURAL RESTORATION

Abstract

Thick layers of mechanically weak evaporite/anhydrite between basement and cover units are prevalent in many extensional settings that were tectonically active in geologic time. The rheological heterogeneity due to the presence of such layers causes decoupling of the extensional deformation between the shallower and deeper regions. The degree to which the decoupling effect plays a significant role in defining the structural geometry is dependent on the mechanical stratigraphy of the weak layer and it overburden as well as the amount and rate of fault displacement. Even if the mechanical stratigraphy is favorable for decoupling of deformation hard linkage of basement and cover fault can still be achieved by an increase in the amount and rate of fault displacement. In many rift basins the amount and rate of fault displacement, which are indicators of the rift activity, are slow to begin with ('rift initiation') and is followed by a period of increased activity and subsidence ('rift climax'). This study presents a structural analysis of the Smørbukk area of the Halten Terrace, offshore Mid-Norway. The area has a thick sequence of Middle-Late Triassic evaporite interbedded with dolomite and anhydrite rich shale (collectively referred to as 'salt') between the Permo-Triassic sedimentary basement and the Jurassic cover. Seismic interpretation of a 3-D time migrated seismic dataset and structural restorations of depth converted sections provided means to investigate the fault evolution and the role of the salt in decoupling

the shallower deformation from the deeper. The results of the study show that extensional deformation was partitioned above and below the salt layer by the development of major faults that detached at the level of base of salt. The positions of such major basement-detached faults are controlled by basement faults that are blind below the top of salt. Most of the basement faults have a two-phase activation history: first during the earliest phase of 'rift initiation' stage and second during the 'rift climax' stage. Hard linkage of basement and cover faults is achieved at some places only during the 'rift climax' stage. The 'rift climax' stage is accompanied by the development and activity of newer basement-detached faults and the reactivation of some older basement faults which are probably indications of increase in the strain rate.

4.1 Introduction

The presence of thick sequences of mechanically weak units like halite and anhydrite (collectively referred to as salt) play a significant role in influencing the structural geometries of active and passive extensional margins. Salt by virtue of its viscosity is able to flow under low shear stresses, thus acting as layers of detachment in many sedimentary basins. The degree to which a layer of salt may decouple the deformation style above and below it was studied in detail in the North Sea area (Petersen et al., 1992), in the off-shore Mid Norway area (Withjack et al., 1989; Pascoe et al., 1999; Richardson et al., 2005; Marsh et al., 2010) and in the Gulf of Suez area (Brown, 1980; Colleta et al., 1988). Similar studies were carried out in experimental works of Withjack et al. (1990), Koyi et al (1993), Nalpas and Brun (1993), Vendeville et al (1995), Higgins and Harris (1997), Withjack and Callaway (2000) and Dooley et al. (2003).

The most comprehensive discussion is probably done by Withjack and Callaway (2000) who studied the effect of various factors like the thickness of the weak layer and the overburden, cohesive strength of the overburden and the amount and rate of displacement on the preexisting faults beneath the weak layer in decoupling the nature of the deformation (Figure 4.1). In Figure 4.1 note the significant control of the position of the fault below the weak layer in localizing the faults within the overburden. It is also apparent from Figure 4.1 that for a given combination of a strong overburden and an underlying weak unit with sufficient decoupling thickness and viscosity, the only factor that will determine the hard linkage of the faults in the upper and lower sections is the amount and rate of the displacement. In case of many continental rift basins the amount

and rate of displacement or subsidence are initially slow and then they increase rapidly at a later stage. Prosser (1993) refers these two stages as 'rift initiation' and 'rift climax' which are marked by a transition from early fluvial/shallow marine sequence to a deep marine sequence (Lambiase and Bosworth, 1995). Workers like Steckler et al. (1988), Prosser (1993) and ter Voorde et al (1997) have suggested that this transition from 'rift initiation' to 'rift climax' is due to the increase in the rate of extension. Other workers (Gupta et al, 1998; Marsh et al. 2010) have argued that the increase in the rate of subsidence can be achieved even at constant extension rates and can be explained by strain localization and linkage of the most active faults.

In order to investigate the role of a mechanically weak layer of salt in decoupling the extensional deformation it is important to determine with a considerable amount of certainty the relative age of the development of the subsalt and the supra salt faults. The present study focuses on the structural interpretation of a time migrated 3-D seismic dataset from the Smørbukk area of the Halten terrace, offshore Mid-Norway. The goals of this study are to determine a) The relative ages of fault development in a rift system b) The control of any preexisting sub-salt faults in localizing basement-detached faults within the salt and overburden and c) the role of salt in decoupling the extensional deformation and factors promoting the hard linkage of fault above and below the salt layer. This area was chosen because of the relatively good quality of the seismic dataset, the availability of well data with check-shots to calibrate the seismic data and the presence of a relatively stationary salt layer. The salt apparently has not gone through any buoyancy driven halokinetic movements. It is present as a

mechanically weak layer between the sub-salt pre-rift units and the overburden syn-rift and post-rift units thus enabling to study its decoupling effect or hard linkage of faults.

4.2 Tectonic Setting of the study area

There is a presence of large scale sedimentary basins of Jurassic age beneath the shelf and continental slope in the area offshore of the central Norwegian mainland between latitudes 62°N and 69°N. The important physiographic features that are seen in this area (Figure 4.2a) at the level of top of Jurassic are the Trøndelag Platform towards the east, the rhomboidal shaped Halten Terrace in the middle and the deep Cretaceous Vøring Basin and Møre Basin towards the west. The western margins of these Cretaceous Basins are defined by the Late Cretaceous-Early Tertiary volcanic oceanic margin of the Vøring Marginal High and the Møre Marginal High separated by the Jan Mayen Fracture Zone.

The Smørbukk area is located approximately 200 km west of the Norwegian mainland and at approximately 290 m water depth, towards the north-western part of the Halten Terrace. The Halten Terrace is about 80 km wide and 130 km long with an area of approximately 10000 km^2. It is located between 64˚N-65˚25'N and 6˚E-7˚40'E (Figure 4.2a). A complex pattern of normal faults of varying ages affects the entire terrace. There are two dominant trends of these faults – N-S and NNE-SSW which overall defines the rhomboidal shape of the Halten Terrace. The Halten Terrace is bounded by the Bremstein Fault Complex towards the east which separates it from the Trøndelag Platform. The Vingleia Fault Complex defines the southern and the southeastern boundary of the Halten Terrace separating it from the Frøya High. It is bounded by the Klakk Fault Complex towards the west and southwest which separates it from the

deeper Møre Basin and Vøring Basin. Towards the north, the Halten Terrace merges in to the narrower and deeper Dønna Terrace. The Halten terrace thus occupies an intermediate structural level between the structural high of the Trøndelag Platform towards the east and the structural low of the deep Møre Basin and Vøring Basin towards the west. Internally the terrace is divided into approximately two halves by the Grinda Graben and the Kya Fault complex with the Gjæslingan Lineament separating them. The seismic dataset in the Smørbukk area used in this study is located towards the northwest of the Grinda Graben (Figure 4.2b). A series of basement-detached and basement-involved faults are present in this area as shown in Figure 4.3 and Figure 4.11. Major among the basement-involved faults are the NNE-SSW trending Smørbukk, the Trestakk, the eastern E1 and the northern R2 shown in Figure 4.11. The major basement-detached normal faults including the Trestakk Shallow are shown in Figure 4.3. Towards the north this area covers what is believed to be a relay zone between the Smørrbukk Fault and the southernmost part of the major Revfallet Fault zone. The area under the seismic dataset covers two major hydrocarbon fields – Smørrbukk and Smørrbukk Sør. (Forbes et al., 1991; Ehrenberg, 1992; Blystad et al., 1995; Corfield and Sharp, 2000; Klefstad et al., 2005; Marsh et al., 2010).

4.3 Regional Stratigraphy

The sediments contained in all the Mid-Norway basins range in age from late Paleozoic to Cenozoic. The regional stratigraphy of the Haltenbanken area is summarized in Figure 4.4. No Haltenbanken wells have penetrated any pre-Triassic strata. The oldest beds penetrated by a well in this area are of consistent thickness and of Middle Triassic in age. It consists of 220 m of continental shale and sandstone

collectively referred to as the Red beds in Figure 4.4. This interval is considered as the basement by earlier workers like Marsh et al. (2010) and in the present study. The term 'basement' is loosely used in this study to refer to the sub-salt units. The actual mechanical basement comprising of igneous/metamorphic rocks is expected to be at a deeper level beyond the coverage of the seismic data. The Red beds are overlain by two evaporite layers each 500 m thick. The evaporite layers are Middle to Upper Triassic in age and are separated by a 500 m thick dolomite and anhydrite rich shale. The upper and the lower evaporite layers were not seismically resolved separately in this study. For the simplicity of description the three above-mentioned layers are collectively referred to as 'Salt' in Figure 4.4 keeping in mind the stratigraphic heterogeneity of the interval. They are overlain by a layer of Red/Gray beds of variable thickness (150m-500m) and on these sits the approximately 500 m thick Åre Formation of Upper Triassic to Lower Jurassic age. The presence of the thick salt layer introduces a significant variability in the stratigraphic rheology. The Åre Formation is comprised of sandstone, shale and coal and is probably a reflection of a deltaic environment. The coal is considered as a potential source rock. The sandstones commonly show fining upward trends and probably are derived from point bar and crevasse splay deposits. In the study area the lower Åre Formation show significant growth along the hanging walls of few of the major large displacement basement-detached listric faults.

The Åre Formation is overlain by a 112-150 m thick tidally influenced near-shore marine sandstone of the Tilje Formation. The Tilje Formation contains thin zones of offshore shale and bioturbated siltstone within it. It underlies the Ror Formation believed to be deposited from a major marine transgression in the Halten Terrace area.

It consists of an upward coarsening sequence of marine shales. The 0-84m thick Tofte Formation comprised of coarse grained poorly sorted cross bedded sand occurs in between upper and lower Ror Formation of 55-75m and 0-20m thickness respectively. The transgressive deposits of the Ror formation are overlain by the beds of the Middle Jurassic Fangst Group believed to be deposited during a marine regression. The Fangst Group is comprised of three formations: the lower 60-80 m thick nearshore marine sand and bioturbated shale deposits of the Ile Formation, the middle 25-35 m thick marine shelf deposit of the Not Formation, and the upper 40-45 m thick sandstone deposition of the Garn Formation. The Garn Formation is overlain by 115-280m thick shale and siltstone deposits of the Melke Formation and 10-70 m thick deep marine shale deposits of the Spekk Formation. The entire upper Jurassic in the Smørbukk area underwent significant erosion and in most of the study area the upper Spekk Formation is bounded by the regional Base of Cretaceous Unconformity (BCU).

The BCU is overlain by the thick Cretaceous shale and occasional turbiditic sandstone deposits of the Cromer Knoll and Shetland Groups of 660-750 m and 850-900 m thickness respectively. In the study area these units are mostly unfaulted but show noticeable thickness changes above the major underlying buried faults suggesting extensional reactivation on the underlying faults. There is a regional Upper Cretaceous unconformity which underlies the Tertiary deposition of the Tang Formation (50-100 m thick), the Tare Formation (70-100 m thick), the Brygge Formation (150-350 m thick) and 300-450 m of the Kai Formation from bottom to top. All these are overlain by the Pliocene Naust Formation and Quaternary sequence of alternating gray shale and poorly sorted sand (Ehrenberg, 1992; Marsh et al. 2010).

4.4 Geologic and Tectonic history of the study area

The tectonic evolution of the Halten Terrace area and the overall North Atlantic rifting has been studied by several authors in the past (Buckovics and Ziegler, 1985; Ziegler and Hoorn, 1989; Withjack et al, 1989; Ehrenberg, 1992; Blystad et al., 1995; Dore et al., 1997 and 2008; Marsh et al., 2010). The earliest deformation phase at the Norwegian margin is recorded during the Silurian-Early Devonian time when the Caledonian Orogeny developed by the collision of Fennoscandian Russian plate and Laurentian Greenland plate through roughly 500-420 Ma time period. By Mid-Devonian to Late Carboniferous times this area was subjected to major sinistral movements which gave rise to subsidence and basin development. In this study this event is referred to as the HT1 phase. This was accompanied by transpressional deformation and volcanic and intrusive igneous activity. Crustal extension in the Norwegian margin probably commenced from Late Carboniferous time (450 Ma) onwards and continued till early Eocene (50 Ma) with volcanic activity and opening of the North East Atlantic Ocean. The rifting continued through this time span of approximately 350 Ma in different phases. After the Late Carboniferous rift initiation the second major rifting event was during the late Permian-Early Triassic time during which the subsidence center shifted westwards within the Trøndelag Platform. In this study this event is referred to as the HT2 phase. The rift axis propagated further southwards into the North Sea. Extension picked up again during a third major phase of rifting (referred to as HT3 in this study) initiating during Late Triassic to Early Jurassic time ('HT3 rift initiation') and continued through Jurassic reaching the 'HT3 rift climax' stage during middle-early to late Jurassic time. There was a period of tectonic

quiescence between the time of cessation of HT2 activity and initiation of HT3 from Middle to Late Triassic. The bulk of the salt layer on the Trøndelag Platform and Halten Terrace is believed to have been deposited during this post-HT2 and pre-HT3 rift phase. The terms like pre-rift, syn-rift, 'rift initiation', 'rift climax' and post-rift used in this study refer to the HT3 phase of rifting. The HT3 phase resulted in significant rollover and growth on the hanging wall of both the basement-detached and basement-involved major normal faults. The HT3 rifting event is recorded in most of the areas within the Halten Terrace. Throughout the time span of the HT3 phase the rift axis gradually shifted towards the west. By early Cretaceous extension started to die out in the Smørbukk area so that very few faults actually displaced the BCU horizon. The fourth phase of rifting (referred to as the HT4 phase in this study) spanning a time from Early to Late Cretaceous was focused more on the western side in the Vøring Basin area developing very deep Cretaceous Basins. The remnant extension in the Smørbukk area of the Halten Terrace still managed to keep the earlier soft and hard linked faults active thus promoting the development of extensional fault propagation fold on the BCU horizon and within the Lower Cretaceous units of the Cromer Knoll and Shetland groups. By Paleocene-Eocene time the Halten Terrace experienced the very last phase of extension recorded by the forced folds on the Top of upper Cretaceous Lange Formation in some parts of the study area. During the same time the crustal separation was achieved further west and the North Atlantic Ocean opened up accompanied by volcanism.

4.5 Dataset and Methodology

A 3-D time migrated seismic dataset was used to derive the results and conclusions of the present study. The seismic data have a line spacing of 12.5 m and covers an area of about 2720 km^2. The seismic data is zero phase, the seismic wavelet having a symmetric shape around zero time. A peak represents an increase in acoustic impedance. The vertical resolution is approximately 30 m. Interpretations of key horizons and faults were made for every 40 in-lines and 40 cross-lines. The data quality is generally good above the Top Salt reflector. It gradually gets poor beneath this horizon. There are twenty-six wells in the area of the dataset out of which data was available for sixteen wells. Checkshot data available from six of these wells (see Addendums) were used to constrain the stratigraphic ages of the horizons picked. None of the wells go any deeper than the top of the Åre Formation. There is some degree of uncertainty in projecting the horizon picks through the fault blocks that did not have any well control especially for those horizons deeper than the Åre Formation. The reasoning and criteria for picking the key horizons are discussed below in detail.

4.5.1 Criteria for interpreting key horizons

Five time horizons were picked manually throughout the seismic survey to constrain the age of the faults. Faults were defined manually by outlining the fault gaps on each horizon. These horizons from bottom to top are:

***Base of Salt**:* The Base of Salt horizon is considered as the top of basement in this study. Movement on basement-involved faults under extension develops broad warps within the cover units. As discussed in Chapter 2 (Figure 2.1) these warps are called extensional fault propagation folds or drape folds. Drape folds are observed in the

central part of the study area (Figure 4.8) where the Base of Salt horizon shows more faulted and the Triassic salt layer and the Jurassic overburden is more folded. Note that because of the sedimentary nature of the basement some degree of drape folding can be expected at the level of Base of Salt horizon (Figure 4.8). These faults probably originate at a much deeper level, either in a shear zone within the hard rock (igneous/metamorphic) basement or at the brittle-ductile transition zone (Skogseid et al., 1992). The Base of Salt horizon was interpreted in detail to compare the nature of faulting in the basement to that in the salt and the cover sequence. The seismic data is noisy at this level mainly because of a) attenuation of seismic signal by the salt layer on the top and b) interference of the seismic signals with migration related artifacts. The approximate time-level of this horizon is determined from the existing publications (Marsh et al., 2010). The tectonic model of this area suggests that the salt was deposited during a period of relative quiescence and does not have significant stratigraphic thickness variation (Ehrenberg, 1992; Marsh et al., 2010). Based on this the Base of salt is picked at a constant time-thickness from the Top of Salt horizon wherever the dataset is extremely noisy at this level and it is assumed that the salt did not undergo any flow related thickness change.

Top of Salt*:* The regional tectonic model suggests that the Top of Salt horizon separates the pre-rift and syn-rift units for the third major HT3 phase of rifting initiating during Early Jurassic time. Also, the thick layer of salt introduces a major rheological variation in the mechanical stratigraphy. Thus the Top of Salt horizon is important to constrain the age of the faults and to study the degree to which the salt decouples the nature of deformation above and below it. The approximate time-level of the Top of Salt is again

determined from published data (Marsh et al., 2010). The presence of the Red/Grey beds on the top of the salt results in a considerable contrast in the acoustic impedance. The noisiness of the seismic data increases drastically beneath this horizon in a number of areas. Due to these reasons the Top of Salt horizon can be tracked through the survey with greater amount of confidence.

***Top of Åre**:* The Top of Åre is the most prominent horizon in the syn-rift (HT3) package. It is an approximate boundary between the 'rift initiation' and 'rift climax' stages of the HT3 phase of rifting. In the study area a major basement-detached fault (referred to as the Trestakk Shallow in this study) shows significant growth within the syn-Åre and post- Åre units as shown by the diverging nature of the reflectors in Figures 4.6 and 4.7. Other basement-detached faults of lesser displacements also show subtle amount of growth within the Åre interval (Figures 4.6 and 4.9). On the other hand, the hard linked major Smørbukk fault shows majority of growth only in the Post-Åre units (Figures 4.6,4.7 and 4.8). Thus the Top of Åre horizon is important to constrain the age of these two different sets of faults of different ages. The time-level of this horizon is determined from the depth of well tops converted to two-way travel time using checkshot velocities. The contrast in acoustic impedance of the Åre Formation with the overlying Tilje Formation is significant and the Top of Åre horizon can be confidently tracked even within fault blocks with no well data.

***BCU**:* The BCU horizon represents a major unconformity throughout the offshore mid Norway area. The tectonic history of this area suggests that this horizon marks a temporary pause in the extension between the HT3 and the HT4 major phase of the rifting event. Most of the areas in the Halten Terrace have undergone the largest amount

of extension only during the HT3 phase of rifting and by HT4 phase the rift axis shifted further west towards the deeper Vøring Basin. The BCU horizon therefore represents the boundary between the syn-rift units and the post rift units in the Smørbukk area. Well tie with the seismic dataset suggests a negative amplitude for the BCU. The seismic signal for BCU is very strong within the dataset and can confidently be mapped throughout.

***Top of Lange**:* In the study area the Late Cretaceous Lange Formation was deposited during the end of the regional HT4 major phase of rifting which marginally affected the structural styles in the Smørbukk area and the Halten Terrace as a whole. The top of Lange is therefore an important horizon that represents the near end of extension. It is a prominent positive-amplitude reflector as suggested from the well ties and can confidently be mapped throughout the study area.

4.5.2 Depth conversion of time horizons and selected time sections:

The 3-D seismic dataset used to make structural interpretations in this study is a time migrated volume. A depth conversion of the above mentioned time horizons and representative structural cross sections in the study area is required to investigate the true to scale structural geometries. Within the study area six wells with checkshot data (see Addendums) were available. The plot of average P-wave velocity derived from the checkshot data versus depth shows an overall linear trend (see Addendums). A linear function was used to make a velocity model of average P-wave velocity for each time horizon for the entire span of the study area. Using these velocity models the time horizons were converted to depth horizons. Local adjustments to the depth horizons were made to fit the well tops.

The representative cross sections were chosen as near as possible to a well with checkshot data. The checkshot data were used to determine the average P-wave velocity and the two-way travel time for a given measured depth of a stratigraphic marker. These were used to calculate the interval velocity between two stratigraphic markers using Dix's Equation (Dix, 1955) (see Addendums). In some areas there is a considerable lateral variation in P-wave velocity within an interval across a major fault. The average time-depth scatter was plotted combining the data from both the wells. The regression equation for a best linear fit across such a scatter was determined and was used as the velocity function for that particular section. Eventually adjustments to velocities were made after initial depth conversion of sections in order to fit well tops.

4.5.3 Isochore Maps

Vertical thicknesses between the depth horizons are calculated and plotted as isochore maps in this study. Changes in the vertical thickness adjacent to the faults in the hanging wall are indicative of growth in between the bounding horizons along the faults. The offset in the positions of a fault polygon between the upper and the lower horizon poses a problem in determining the vertical thickness between the horizons. For this reason while calculating the vertical thickness, the depth horizons which did not have the fault polygons defined on them were used. This method still has a geometric limitation as shown in Figure 4.5a. Near the middle of the fault where the top and the bottom of an interval are closer, the vertical thickness has its minimum value. The areas on the fault surface away from this middle part will still show lower thickness values because parts of the fault surface are considered as the top or bottom of the interval. Thus the entire fault would show as a zone of anomalously low vertical thickness on the

map. Therefore variations in thickness are only studied away from the fault zone. It should also be noted that vertical thickness is a good approximation of true thickness only for shallow dipping intervals. For steeply dipping intervals vertical thickness is always higher than the true thickness. The objective of this study is to determine the changes in thickness and not the absolute value of the thickness. Thus the difference between the vertical thickness and the true thickness does not limit the understanding of the structure even for steeply dipping intervals.

In some scenarios the interval of interest is not displaced by an underlying blind fault but is still affected by drape folding associated with the fault. The upward widening drape fold develops a syncline towards the hanging wall of the blind fault. The syncline act as a local depocenter and its position is offset from the underlying blind fault as shown in Figure 4.5b.

4.5.4 Structural Restoration

The representative time sections converted to depth were restored in order to study the validity of the interpretation and to investigate the structural geometry and amount of extension during the syn-rift and post-rift stages. All sections are oriented perpendicular to the dominant NNE-SSW trend of the structural grain. Parameters to be considered for balancing cross-sections in extensional terrains are discussed in detail by Gibbs (1983). An important step in the restoration process is decompaction, since all the syn-sedimentary units undergo a substantial amount of thickness change during the evolution of the structure and later by the burial under thick overburden (Rowan, 1993). For each section the entire interval from Top of Lange to Base of Salt was decompacted by backstripping the thick Tertiary overburden layers using solidity parameters shown

in the Addendums. An iteration of restoration and decompaction was then repeated for the post-rift Lange Formation and each Jurassic syn-rift unit. Almost all the faults are concave up in shape and restoration was done using a 25˚ antithetic shear angle. In case of faults having convex bends, the portion of the section affected by the convex up bend was restored by 25˚ synthetic shear. Wherever the relief on the BCU is not structurally controlled, underlying units were projected across the BCU to determine their uneroded geometries. The presence of the ductile salt layer in all these sections offers an additional challenge for restoration due to its ability to flow in and out of the section. In the study area, buoyancy driven halokinetic movement or extension driven reactive diapirism is absent within the salt. The salt acts as a detachment layer separating the nature of deformation above and below it. To account for this decoupled style of deformation the post-salt and pre-salt units were restored separately for the restoration of all basement-detached faults. The assumption for this method is that the sectional areas of all the intervals including the salt remain conserved during each step of the restoration; however the thickness of the salt can change locally near the major faults. The change of sectional geometry of a fault due to the synchronous movement on another fault towards the footwall side of the former was taken into consideration while restoring the sections.

4.6 Results: Structural geometry and fault evolution

The structural analysis was done for four major intervals representing the rifting event from Early Jurassic to Late Cretaceous in the Smørbukk area: Base of Salt to Top of Salt, Top of Salt to Top of Åre, Top of Åre to BCU and BCU to Top of Lange.

Results are discussed separately for the seismic interpretation and structural restoration parts of the study.

4.6.1 Results from seismic interpretation

Four time sections and their depth converted versions from across the study area, five depth-structure maps and four isochore maps were chosen to describe the structural style and geometry of the faults and growth units.

Structural geometry and fault evolution in the Base of Salt to Top of Salt Interval: This interval was deposited during a stage of tectonic inactivity spanning from Middle to Late Triassic and represents the pre-rift interval for the HT3 rift phase in the Halten Terrace. The Base of Salt horizon (Figure 4.11) is characterized by an overall relief drop in the middle of the study area and high relief on the western and eastern margins. The horizon is displaced by at least eight major faults. Faults with longest surface traces are the Smørbukk fault towards the NW and the Trestakk fault towards the SE. Both the faults show a gradual strike curvature which may be due to a) connection of each fault segment by oblique ramps during an earlier stage of lateral propagation of the fault and/or b) due to deformation in a 3-D strain field explained by Reches (1983). Synclines related to extensional fault propagation folding is present on this horizon for most part of the Smørbukk fault and the northern part of the Trestakk fault. The Trestakk fault loses its displacement on this horizon from south to north and eventually dies out. The R1 and R2 faults towards the north are believed to be the southernmost part of the major Revfallet Fault system (Pascoe et al., 1999). The displacement on these faults increases towards the north. Majority of faults on this surface have an

approximate NE-SW trend and dip towards NW except for the extreme eastern fault which is SE dipping (Figure 4.12).

Towards its northern end the Smørbukk fault shows an offset relation with a smaller basement-involved fault of similar trend and is connected to it by an oblique fault. The Smørbukk fault shows a gradual decrease in slip towards the north while the offset basement fault shows a local increase in slip towards the north before eventually losing its displacement. From this geometric relation and from the observations of experimental models in Chapter 3 (Section 3.5.3) it can be inferred that the Smørbukk fault and the right stepping offset fault establishes a synthetic transfer zone. Fault slip is probably transferred by the oblique fault connecting them. Earlier workers like Corfield and Sharp (2000) and Dooley et al. (2003) suggested that this area with oblique faulting is a part of the Smørbukk-Revfallet Transfer System. At their intersection (at an angle of approximately 120°) the footwall of the Smørbukk fault and the oblique transfer fault shows an area of triangular high which is more prominent on the structure maps of the tops of younger units (Figures 4.12, 4.13 and 4.14). The structure between these two faults thus presents a trapdoor geometry as observed from the results of the experimental models discussed in section 2.6.1 of Chapter 2.

On the Top of Salt horizon the Trestakk fault is absent (Figure 4.12). This fault is replaced by a major basement-detached listric fault described as the Trestakk Shallow fault in this study. The location of this fault is constrained by the position of the basement-involved Trestakk fault below as is observed in the time sections in Figures 4.6 and 4.7. Basement-detached faults of relatively smaller displacement are present on the Top of Salt horizon towards the SW and NE. The locations of these faults are

apparently unconstrained by a major basement fault below (Figures 4.6 and 4.9). All the basement-detached faults across the entire study area detach on the Base of Salt horizon.

The isochore map of the salt interval is shown in Figure 4.16a. The structural geometry in the time sections (Figures 4.6, 4.7 and 4.9) suggests that the major thickness change of this interval is associated with the flow of salt near the basement-detached listric faults. There is no significant growth-induced change in stratigraphic thickness along any of the major faults that displaces the Top of Salt Horizon. This is in agreement with the regional tectonic history of the study area according to which the salt layer was deposited in a period of relative quiescence before the initiation of the third major phase of the rifting event (Buckovics and Ziegler, 1985; Ehrenberg, 1992; Marsh et al., 2010). A zone of low salt thickness towards the west is seen on the isochore map. This is attributed to the flow of salt towards the lower relief of the Smørbukk hanging wall (Figures 4.7 and 4.8).

Structural geometry and fault evolution in the Top of Salt to Top of Åre Interval:

This interval represents the syn-rift deposition during the 'rift initiation' stages (Late Triassic to Middle-Early Jurassic) of the HT3 rifting phase in the Halten Terrace area. The structural relief of the upper bounding surface of this interval, the Top of *Åre* horizon has an overall drop from east to west (Figure 4.13). The synclines on the Top of Åre are related to the extensional fault propagation folding associated with movement on faults that either displace the horizon or are buried below it. The basement-involved faults that displace this horizon are the Smørbukk fault and to some extent the oblique faults of the Smørbukk-Revfallet transfer system. Among the basement-detached listric

faults displacing this horizon the Trestakk Shallow fault has the maximum displacement. Along a linear stretch towards the south as shown in Figure 4.13 the Trestakk Shallow fault comes very close to the Smørbukk fault. Footwall erosion of the Smørbukk fault results in the lower Cretaceous erosional level reaching up to the top of Are in this linear stretch (Zone marked as 'Erosion' in Figure 4.13). Most of the other basement-detached faults that displace the Top of Salt Horizon (Figure 4.12) also displace the Top of Åre horizon with decreasing amount of displacement. Towards west the Top of Åre map shows two highly oblique NW-SE trending normal faults that detach on the top of salt (Figure 4.10). They are believed to have been developed from gravity driven movements of the salt induced by sufficient change in dip of the underlying faulted basement (Marsh et al, 2010)

The Trestakk Shallow fault has the maximum growth in this interval as shown in the isochore map in Figure 4.16b. On all the time sections shown in Figures 4.6, 4.7, 4.8 and 4.9 an Intra- Åre horizon was picked to study the growth history of different faults during the deposition of the Åre interval. Growth during the deposition of the Åre interval was always observed to be more on the basement-detached faults (highest being on the Trestakk Shallow fault) than on the basement-involved faults. All these indicate that the basement-detached faults were more active than the basement-involved faults during the 'rift initiation' stage of the HT3 phase (syn Åre).

Structural geometry and fault evolution in the Top of Åre to BCU interval:

This interval correlates to the 'rift climax' stage (Prosser, 1993) of the syn-HT3 phase of rifting event in the Halten Terrace. The top bounding surface of this interval, the BCU, has an overall drop in structural relief from east to west (Figure 4.14). The

basement-involved faults that displace the BCU horizon are the northern part of the Smørbukk fault and the eastern (E1 and E2) faults. Among the basement-detached faults the Trestakk Shallow fault towards the south and the western and northern oblique fault pairs partly displace the BCU horizon. The Smørbukk fault loses displacement towards both north and south and eventually dies out in both directions on the BCU horizon. Synclinal axes on BCU that line up with the major faults on the Top of Åre horizon suggest that those faults were active at least till the end of the 'rift climax' stage.

Most of the basement-involved (except R1 and R2 towards the north) and basement-detached faults show growth in this interval. This is evident from the diverging geometry of the reflectors in the hanging wall and synclines associated with these faults (Figures 4.6, 4.8 and 4.9). The thickness variation is reflected by the curvilinear zones of higher thickness values on the isochore map of this interval in Figure 4.16c. It should be noted here that the synclinal depocentres associated with the late movement on the blind basement faults are always offset from fault strike due to the drape folding in the salt and the cover units (Figure 4.5b). The majority of the growth on the western oblique faults (related to salt movement) is observed in post-Top of Not units. The basement-involved Trestakk and the basement-detached Trestakk Shallow fault above it show an interesting relation in terms of their position and age of growth units. The shallower Trestakk Shallow fault shows growth in the syn Åre and post Åre units. As a major fault it shows activity only in the southern side and dies out towards the central part of the study area. The deeper Trestakk fault underlying it shows indications of post Åre activity in terms of axial thickening and diverging geometry of reflectors in the

syncline associated to it only towards the immediate north of the tip of the Trestakk Shallow fault. This syncline related to drape folding above the Trestakk fault is absent towards the south where the Trestakk Shallow fault is active. These observations lead to the conclusion that the Trestakk Fault was probably active in two stages: a) First, during a pre- Åre time and b) Second, during a post- Åre time synchronous with the deposition of the uppermost Jurassic-lower Cretaceous units. From the above discussion about the relative age of fault development it is apparent that major activity along most of the basement-involved and the basement-detached faults are restricted during the deposition of Top of Åre to BCU interval which represents the 'rift climax' of the HT3 phase. It is probably an indication of significant escalation of tectonic activity during this time and may suggest an increase in the rate of extensional deformation in the Halten Terrace area.

Structural geometry and fault evolution in the BCU to Top of Lange interval: This interval correlates to the post-rift stage of the HT3 rifting phase in the Halten terrace during early to late Cretaceous. During this time the rift axis shifted towards the west so that activity was more concentrated along the faults in the Vøring Basin. None of the faults discussed in the previous sections intersect the Top of Lange horizon (Figure 4. 15). However the structural geometry of the hanging wall synclines on this surface suggests the remnant activity of the basement-involved Smørbukk, Trestakk, and Eastern E1 faults and the basement-detached Trestakk Shallow fault and the southwestern and northeastern listric faults.

Growth in this interval is restricted mostly within the units of the Cromer Knoll and Shetland Group deposited in the synclines of the forced folds associated with the major

faults. This is evident from the thickening and thinning of units near the synclinal axes and flanks respectively within the lower part of this interval (Figures 4.6, 4.7, 4.8 and 4.9). The thickness variation is reflected on the isochore map of this interval as shown in Figure 4.16d. It is interesting to note that even though this interval is displaced by fewer faults there is noticeable growth related thickness variation of the post BCU units on the hanging wall synclines offset from the major underlying blind faults.

4.6.2 Results from structural restoration

Structural restoration of selected depth sections is done on six key horizons to study the fault evolution through the post-rift, late syn-rift ('rift climax'), early syn-rift ('rift initiation'), and pre-rift stages of the HT3 rifting phase in the Smørbukk area of the Halten Terrace. Restoration on the Top of Lange and BCU yields the extensional deformation during the late and early post-rift stages respectively. A regional drop of 1° towards WNW was considered for the top of Lange and BCU horizons since the Cretaceous units show a gradual thickening towards the west. Restoration on the Top of Åre shows the extension during the 'rift climax' stage. Restoration on the Intra Åre and Top of Salt horizons shows the extension during 'rift initiation' stage and restoration on the Base of Salt horizon yields the pre-rift extension during the earlier pre-salt (Late Permian-Early Triassic) HT2 phase of rifting.

In all the depth sections, decompaction for a particular interval always results in the increase of thickness and the structural amplitude of the intervals below it. As discussed in a previous section the restoration was done separately for units above and below the salt layer. The implication of this method is that a basement-involved fault that is blind and inactive below a basement-detached fault was restored only after the restoration of

the basement-detached fault above it. The amount of extension involved in each step of restoration is measured both on the Top of Salt and the Base of Salt horizon in order to study the decoupling effect of the salt. It should be noted however that the total amount of extension measured on the Top of Salt horizon in each stage includes the activity of both the hard linked basement-involved faults and the basement-detached faults displacing the post salt units.

Restoration on the Top of Lange horizon shows negligible amount of extension for all the sections. This reflects the lack of tectonic activity during the late post-rift stages of the HT3 phase. For the restoration on the BCU the undeformed BCU horizon is not always considered to be uniformly flat especially in those areas where the structural controls on the relief of this horizon is not apparent. BCU being a major unconformity associated with significant erosion and non-deposition, supports the idea. There is always a degree of uncertainty in determining the exact structural geometry of the undeformed BCU. Wherever truncated by the BCU, the faults and the pre-BCU horizons were projected maintaining the uniformity of their structural trends to determine their uneroded geometries. In all the depth sections restoration on the Top of Åre (or Top of Not in case of Inline 1820) always shows the maximum amount of extension involved as expected during the 'rift climax' stage.

Inline 1820: Figure 4.17 shows a 23.8 km long depth converted section for inline 1820. Due to a significant amount of growth of the post Åre units on the Trestakk Shallow fault in this area two additional horizons, Lower Cretaceous and Top of Not was introduced in this section in order to better constrain the steps of restoration. Step 1 through Step 3 shows the restoration on the Top of Lange, the Lower Cretaceous

horizon and the BCU. Restoration on these horizons yields low amount extension due to post rift drape folding on major faults. In Step 3 the BCU was considered to have a scarp on the footwall of the Smørbukk fault. In Step 4 units affected by the BCU erosional unconformity were reconstructed to their true stratigraphic thickness in order to restore on an uneroded horizon. The assumption for this reconstruction is that after the deposition of the upper Jurassic (BCU to Top of Not) interval there was a period of activity on the basement-involved Smørbukk fault that was associated with little or no sedimentation thus exposing a fault scarp. Step 5 through Step 10 shows the restoration on the Jurassic horizons including salt and the Permo-Triassic basement. Most of the extensional activity is restricted within the interval between Top of Åre to BCU which corresponds to the 'rift climax' stage and is contributed mainly by the large displacement basement-detached Trestakk Shallow fault. Since this fault detaches towards the footwall side of the basement-involved Smørbukk fault, the shallower part of the Smørbukk fault was considered to have a curved geometry in Step 6 in order to address area problems. In step 7 of Figure 4.17 the shallower part of the Smørbukk fault and its antithetic fault loses their displacements. This validates the notion from seismic interpretation that majority of the post-salt activity of the basement-involved Smørbukk fault was restricted during the post Åre time. Step 7 and Step 8 show that during the syn Åre time ('rift initiation') only the shallow listric faults were active which indicates that the salt was effectively decoupling the extensional deformation at this time.

It is interesting to note that The Smørbukk fault does not die out totally on the Base of Salt horizon at Step 7. This may suggest two different scenarios: 1) The Smørbukk fault was active during the pre-salt HT2 phase of extension (Late Permian-Early Triassic)

and presented a faulted topography for the later salt deposition. There was no movement on the fault during the HT3 phase until the post- Åre time ('rift climax') during which it was reactivated. 2) The entire movement history of the Smørbukk fault is restricted within the HT3 phase. The first stage of activation of the Smørbukk fault was post-salt but pre- Åre corresponding to the earliest phases of the HT3 'rift initiation' stage; the second stage of activation was during HT3 'rift climax' (post- Åre) time. It should be noted that Scenario 2 does not rule out the initiation of the Smørbukk fault from a pre-existing basement weakness zone developed during the earlier HT2 phase. The same scenarios also hold true for the other major basement-involved Trestakk fault which shows larger displacement on the Base of Salt horizon than the Smørbukk fault. The evidence for its reactivation is however present in the form of synclinal growth of post-Åre units associated to the forced fold towards the north where the Trestakk Shallow fault dies out (as discussed in an earlier section) (Figure 4.8). Though both the scenarios are credible Scenario 2 seems to provide a better explanation for the driving force (movement on subsalt faults during earliest phases of HT3 'rift initiation') required to initiate the large scale basement-detached Trestakk Shallow fault. Plausibility of Scenario 2 comes with the assumption that the early movement on the subsalt faults (especially that on the Trestakk fault) was enough to initiate the Trestakk Shallow fault within the salt but not sufficient to keep pace with the rate of sedimentation to record any growth wedges within the lower or upper Åre interval. On the other hand if Scenario 1 were to be true, one would have to assume that the driving force for the initiation of the Trestakk Shallow fault is just passive flow of salt on an initially faulted topography thus requiring no regional extension which is unlikely in this tectonically

active area. Irrespective of which scenario is true, the results from the seismic interpretation from the supra-salt section and structural restoration in this study strongly indicate at least two stages of activity of the basement faults.

Inline 3180: Figure 4.18. shows a 21.6 km long depth converted section for Inline 3180. The structural geometry of the faults and horizons in this depth converted section does not differ significantly from that in inline 1820. The Trestakk Shallow fault is the single major listric fault in this section. The other faults in this section are the hard linked Smørbukk fault and the blind Trestakk fault. The salt layer thins out towards the WNW end of the section and suggests salt withdrawal from the west and flow of salt towards the hanging wall of the Smørbukk fault. The timing of the salt movement is however unclear in this section since noticeable thickness differences of supra salt stratigraphic units associated to salt movement were not observed.

The results of restoring this section are similar to the ones obtained from restoring Inline 1820 as discussed in the previous section. Most of the extensional activity is noted during the deposition of the Top of Åre to BCU interval corresponding to the 'rift climax' stage (Step 3 in Figure 4.18). Similar to Inline 1820, the Smørbukk fault dies out in the post salt units after restoring on the Top of Åre horizon (Step 3 in Figure 4.18). At this step (as in Inline 1820) the Trestakk Shallow is the single major fault with significant displacement and growth within the Åre interval. All these suggest that throughout the southern part of the study area the salt acted as an agent for decoupling the extensional deformation especially during the 'rift initiation' stage. Basement faults were not hard linked till the 'rift climax' stage which was probably accompanied by an increase in overall extensional activity in the whole Halten Terrace area.

Inline 4100: Figure 4.19. shows a 36km long depth converted section for inline 4100. In this section all the active faults are basement-involved and only the Smørbukk fault is hard linked through the salt interval. The other basement faults are blind below the level of Top of Salt and show drape folding of salt and supra salt units above them. The absence of shallow faults detaching at the Base of Salt horizon points to the fact that in this area the salt did not act as an agent for decoupling the extensional deformation above and below it. Extension was thus measured only on the Base of Salt horizon. The thickness difference of the salt unit towards the western end of the section is probably due to the flow of salt as a response to the movement on the hard linked Smørbukk fault.

Step 1 and Step 2 show the post rift (HT3) activity during the deposition of the Cretaceous units. Among the Jurassic supra-salt horizons restoration on the Top of Åre yields the maximum extension (Step 3 in Figure 4.19) involved during the deposition of the Top of Åre to BCU interval. The very low amount of extension when restored on the top of Intra Åre (Step 4 in Figure 4.19) or the Top of Salt horizon (Step 5 in Figure 4.19) validates the notion from seismic interpretation that most of the basement-involved faults in this area remained almost inactive during the deposition of the Åre interval ('rift initiation' stage of HT3 phase). The 867m of extension when restored on the Base of Salt horizon in Step 6 is probably related to the early movements on the basement-involved faults (Scenario 1 or Scenario 2 from a previous discussion).

Inline 5820: Figure 4.20. shows a 16.7km long depth converted section for inline 5820. The structural style in this section is different from that in Inline 1820 and Inline 3180. The basement-detached faults dip towards SE unlike the NW dipping basement-

detached faults in Inline 1820 and Inline 3180. Basement-involved faults are hard to detect in this area. The basement-detached listric fault in the middle of the section shows drape folding of the Cretaceous units. The listric fault towards the SE end of the section detaches at a level higher than the Base of Salt (probably at the top of the lower salt interval in the stratigraphic column in Figure 4.4). Extension was however measured only on the Top of Salt horizon and contribution by individual listric fault was not determined.

Step 1 and Step 2 in Figure 4.20 show the amount of extension involved during the drape folding of the Cretaceous units above the listric fault in the middle of the section. Similar to restoration of the previous sections, highest amount of extension was involved when restored on the Top of Åre (Step 3 in Figure 4.20). Thus the notion that the activity of the faults was maximum during the deposition Top of Åre to BCU interval ('rift climax' of the HT3 phase) still holds true in this northern part of the study area. Step 4 and Step 5 shows the amount of extension involved during the deposition of the Åre interval. These values are still less than those in Inline 1820 (Step 8 and Step 9 of Figure 4.17) and Inline 3180 (Step 4 and Step 5 of Figure 4.18) where the majority of the extension during the deposition of Åre is on the Trestakk Shallow listric fault. This observation probably suggests that the degree to which the salt decoupled the extensional deformation was more in the southern side during the 'rift initiation' stage.

4.7 Discussion

4.7.1 Relative ages of fault development

Based on the results from the seismic interpretation and structural restoration the major basement-involved and basement-detached faults present a complex episodic

history of activity in the study area. Table 4.1 summarizes the relative ages of activity of the major faults. The subsalt basement faults (Smørbukk , Trestakk, eastern E1) were probably the earliest active faults in this area during the early 'rift initiation' stage (Late Triassic) (Figure 4.21b; Considering Scenario 2 to be more plausible than Scenario 1 as discussed in an earlier section). However their activity was restricted to a post salt but pre Åre period. Indications of their syn- Åre activity in terms of growth is not observed. These subsalt faults probably provided the driving force for the initiation of shallower large displacement basement-detached faults like Trestakk Shallow. After this, during the majority of the 'rift initiation' stage (Latest Triassic to Early Jurassic) corresponding to the bulk of deposition of the Åre interval the Trestakk Shallow fault had the maximum amount of extension and thus maximum activity associated to it. The activity of the other basement-detached faults in terms of thickness of growth units was less compared to that on the Trestakk Shallow (Figure 4.21c). Later during the 'rift climax' stage (middle-early to late Jurassic) most of the faults were active. The hanging walls and the synclinal axes related to these faults record the activity in terms of growth induced thickness difference and diverging reflectors (Figure 4.21d). During a later part of this stage (post-Top of Ror; Middle Jurassic) a gentle southward tilting of the entire terrace probably initiated the gravity induced salt movement that resulted in the WNW-ESE trending oblique faults towards the western part of the study area (Marsh et al, 2010). Most of these faults discussed above were active through Early Cretaceous during the post-rift stage of the HT3 rifting phase in the study area.

4.7.2 Controls of subsalt fault in localizing the shallow basement-detached faults

The results of the present study show that the relationship of the basement-involved Trestakk fault and the large displacement basement-detached Trestakk Shallow fault above it is complex in terms of their position and the age of growth units. The relatively smaller displacement basement-detached faults do not seem to have any noticeable basement control. Previous studies of this area (Marsh et al., 2010) have interpreted the Trestakk fault as one single fault displacing horizons from Base of Salt level to BCU. There are places within the study area where the Trestakk and the Trestakk Shallow do seem to be a single fault but in other places these faults can be clearly identified separately (Figure 4.7). In order to have these faults interpreted as a single fault the sectional geometry of that single fault would have to have a sharp convex bend which does not seem likely from the geometry of the horizons in most of the southern part of the study area where the Trestakk Shallow is active. Furthermore, growth is observed in different intervals for these two faults. The Trestakk Shallow fault has rollover and growth on its hanging wall throughout the deposition of syn- Åre and post- Åre intervals (Figures 4.6 and 4.7). On the other hand, growth on the Trestakk fault is restricted only to the post- Åre units in the hanging wall syncline of the drape fold associated to it Figure 4.8). These observations lead to invoke a two-stage activation hypothesis for the deeper Trestakk fault. Initial movement of the Trestakk fault during the earliest 'rift initiation' stage (pre- Åre) probably helped to initiate and localize the Trestakk Shallow fault above it. During most of the 'rift initiation' stage and later during the 'rift climax' stage a significant portion of the tectonic activity was taken up by the Trestakk Shallow fault towards the southern side of the study area. The

Trestakk fault is active in response to the extension during 'rift climax' stage towards the central part of the study area where the Trestakk Shallow fault is absent.

4.7.3 Role of salt in decoupling the extensional deformation

The nature of the seismic data has led to the interpretation of most of the large displacement faults as soft linked basement-detached faults, which has interesting implications on the regional tectonic model. The factors related to mechanical stratigraphy that determine whether or not the faults in the basement and in the cover units would be hard or soft linked are the relative thickness and ductility/viscosity of the salt layer and cover units. Apart from this the structural factors are the amount and rate of displacement on the faults. The degree to which these factors might be active in salt related extensional systems has been studied in detail by Withjack et al, 1989, Davy et al (1995), Pascoe et al (1999), Dooley et al (2003), Withjack and Callaway (2000) and Richardson et al (2005) both in analog models and in the Halten Terrace area and the areas just north of it. The studies by these authors have shown that partitioning of extensional deformation between basement and cover units would occur wherever the mechanical stratigraphy consists of a salt layer of sufficiently low viscosity overlain by a thinner overburden with high cohesive strength. However, even if the mechanical stratigraphy is favorable for a soft linkage of the basement and cover faults, hard linkage can still be attained if the amount or rate of displacement on the fault increases. The amount of activity on a fault is again dependent to some extent on the stage of rifting it belongs to. The role of salt as a regional décollement in the Halten Terrace area thus has to be considered in terms of the above mentioned factors.

The large displacement basement-detached listric faults are active towards the southern and northern part of the present study area (Figures 4.6, 4.7 and 4.9) and are absent in the central part (Figure 4.8). The presence of the listric faults detaching at the base of salt (or within the salt) probably infers that the salt has effectively decoupled the extensional deformation between the basement and the cover units in the northern and the southern parts.

In the southern area of study the time during which salt was the only defining factor in partitioning the extensional deformation was probably during the 'rift initiation' stage (syn Åre) when all the active faults were listric (Step 8 and Step 9 of Figure 4.17 and Step 4 and Step 5 of Figure 4.18). The 'rift initiation' stage is supposedly accompanied by lower rates of extension (Prosser, 1991). During the 'rift climax' stage (post Åre) extensional activity was however shared between both the basement-detached faults and the reactivated basement-involved Smørbukk fault (Step 5 through Step 7 in Figure 4.17 and Step 3 in Figure 4.18). The 'rift climax' stage had also seen the reactivation of the basement-involved Trestakk fault and the eastern E1 fault in the central part (Step 2 in Figure 4.19) and an increase in the activity of the basement-detached faults towards the northern part of the study area as well (Step 3 in Figure 4.20). All these might suggest that there was an overall increase in the rate of extension during the 'rift climax' stage of the HT3 phase of rifting. This increase in the rate of extension may have become the defining factor for the hard linkage of the Smørbukk fault in the southern part of the study area where the overall mechanical stratigraphy was still favorable for decoupling of extensional deformation in the basement and the cover units.

4.8 Conclusions

Two dominant structural styles were observed in the Smørbukk area of the Halten Terrace – basement-involved faulting and basement-detached listric faulting. The basement-detached faults detach at the level of Base of Salt horizon and are present in the northern and southern part of the study area; they are absent in the central part of the study area.

The Smørbukk area of the Halten Terrace has recorded a complex history of fault activity. The basement-involved faults show at least two stages of activity whereas the basement-detached faults show a single stage of activity. Earliest activity of the basement faults can be pre-salt or post-salt (but pre Åre). A post-salt (pre Åre; Late Triassic earliest 'rift initiation' stage) initial activity model for the basement faults is favorable to explain the driving force for the development of the overlying major basement-detached faults. The second stage of activity of the basement-involved faults was during a post Åre time corresponding to the 'rift climax' stage (Middle to Late Jurassic) and their activity continued through the post HT3 rift phase (Early Cretaceous). Most of the basement-detached faults were active through the later 'rift initiation' (syn Åre; Latest Triassic to Early Jurassic) and 'rift climax' stages, majority of the activity being during the 'rift climax' stage as recorded by the greater thickness of the growth units. The activity of some of these basement-detached faults continued through the post HT3 rift phase.

Among the basement-detached faults the Trestakk Shallow shows the highest amount of extensional activity in terms of growth and its position is controlled by the underlying basement-involved blind Trestakk fault. The Trestakk Shallow fault is active only in the

southern part of the study area. Reactivation of the deeper Trestakk fault is seen in terms of growth in the hanging wall synclines of broad drape folds towards the central part of the study area where the Trestakk Shallow fault has died out.

The role of salt as a regional décollement varies both spatially and temporally in the study area. It decouples the extensional deformation above and below it towards the northern and southern part of the study area where the basement and the cover faults are soft linked. During the 'rift climax' stage there was probably an overall increase in the rate of extension in the Halten Terrace area. This caused the basement-involved Smørbukk fault to be hard linked during a post Åre time even towards the southern part of the study area where the mechanical stratigraphy was still favorable for soft linkage of basement and cover faults.

Figures and tables

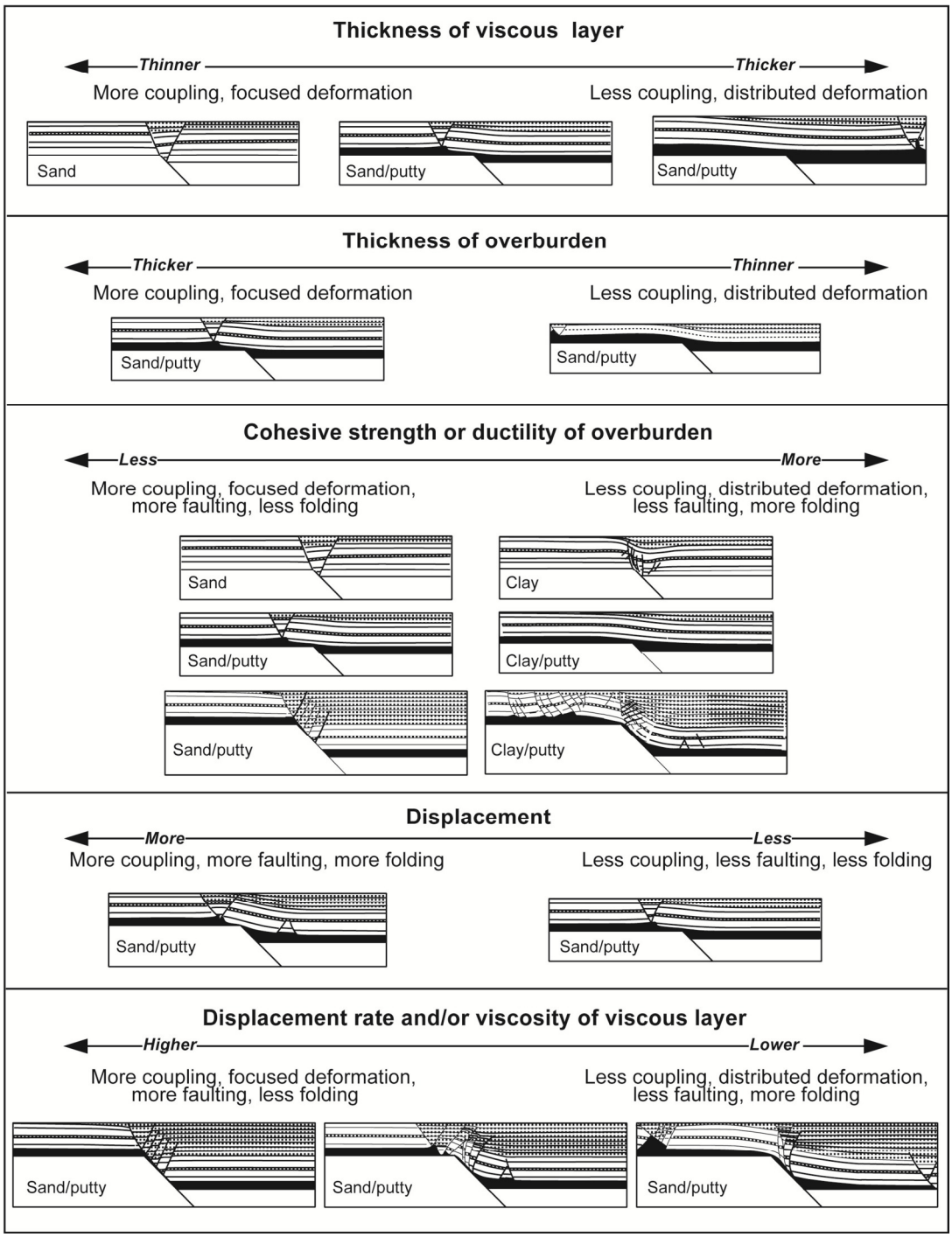

Figure 4.1 Summary of results from extensional analog modeling using rigid basement and ductile cover with an intermediate viscous layer (from Withjack and Callaway, 2000). The top three panels show the variation of the sectional geometry of the structure resulting from difference in thickness and cohesive strength of the cover and the thickness of the viscous layer under a uniform rate of displacement. The two bottom panels show the effect of change of viscosity of the weak layer and of the amount and rate of displacement.

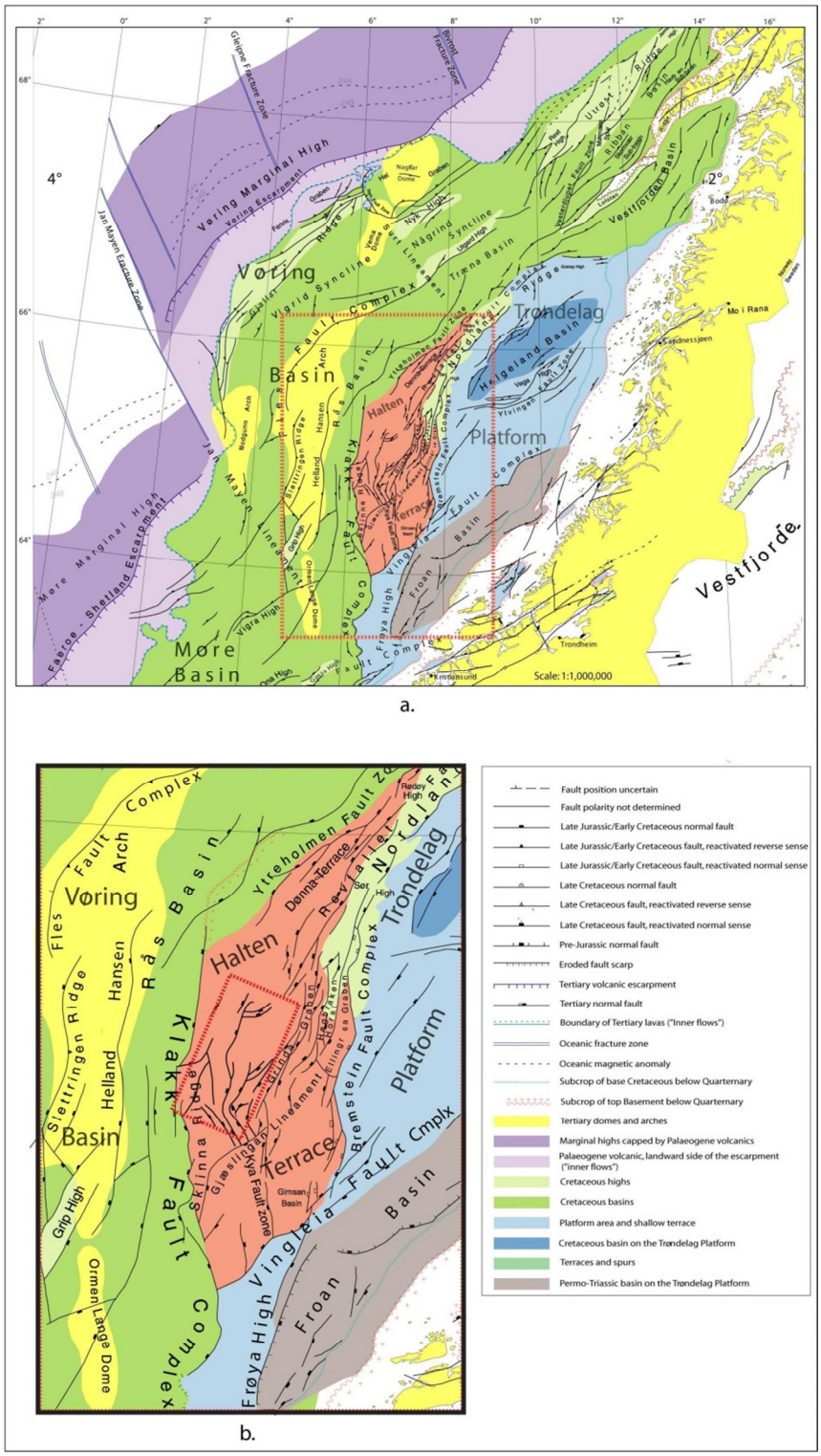

Figure 4.2 a. Regional structural map of the offshore Mid-Norway region showing the location of the Halten Terrace with respect to the major structural zones and basins. Red dotted box outlines the area shown in (b). b. Enlarged structural map of the Halten Terrace with the key bounding regional fault zones and in the study area. The red dotted box outlines the 3-D seismic survey area. Redrawn and modified from Blystad et al. (1995).

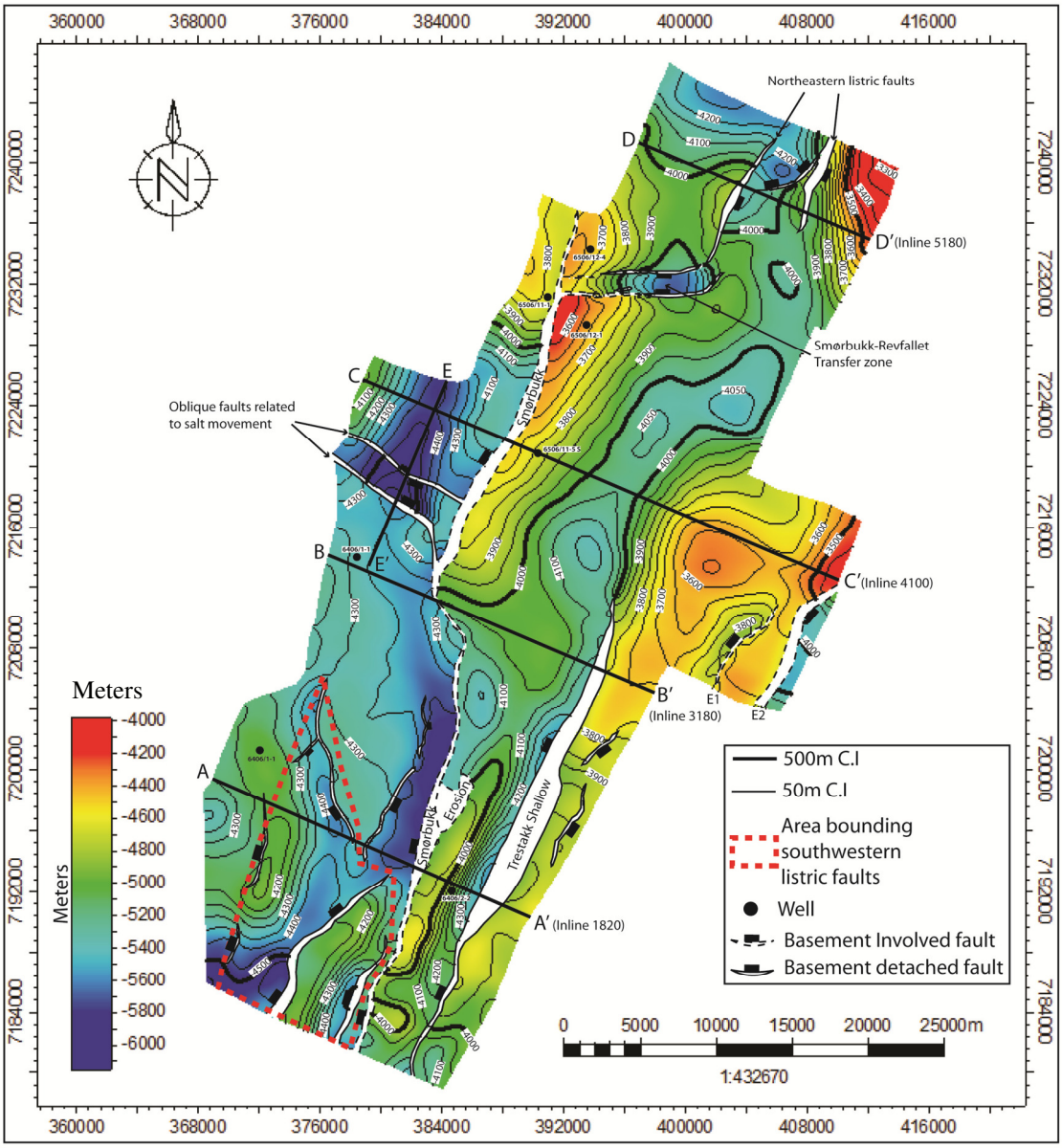

Figure 4.3 Sub-regional index map of the study area showing the location of the wells and major normal faults. Fault polygons and color and line contours are drawn on the depth-top of the Early Jurassic Åre Formation. The positions of the cross sections shown in subsequent figures are marked by thick black lines. For the locations of the other major basement-involved faults, refer to Figure 4.11.

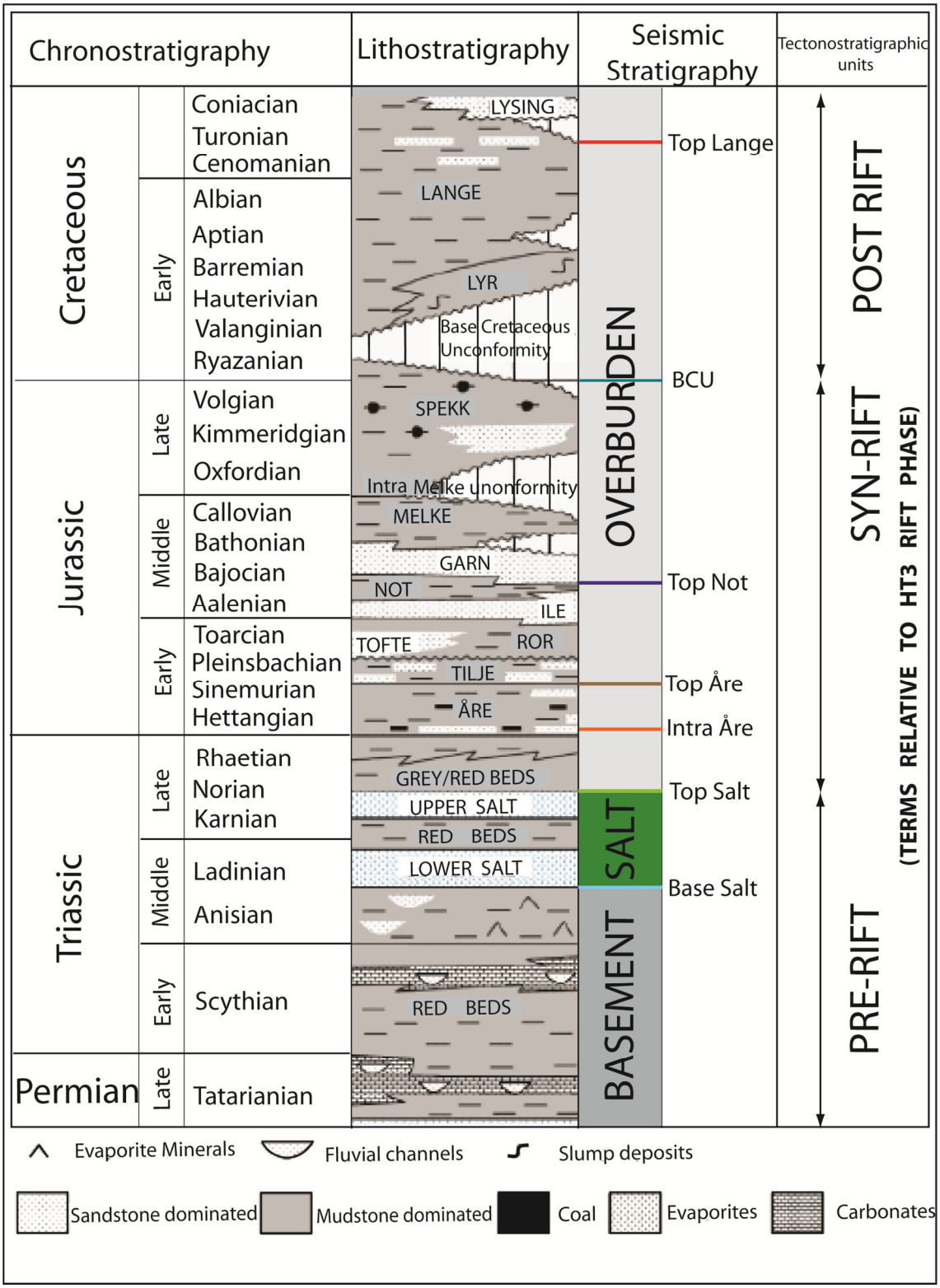

Figure 4.4 Regional stratigraphic framework showing the representative lithologies and the ages of the formations in the Halten Terrace area (Modified from Marsh et al., 2010). Interpretation of the main tectonostratigraphic units in the area is shown in the right column. Colored and highlighted lines represent the seismic marker horizons interpreted in the present study.

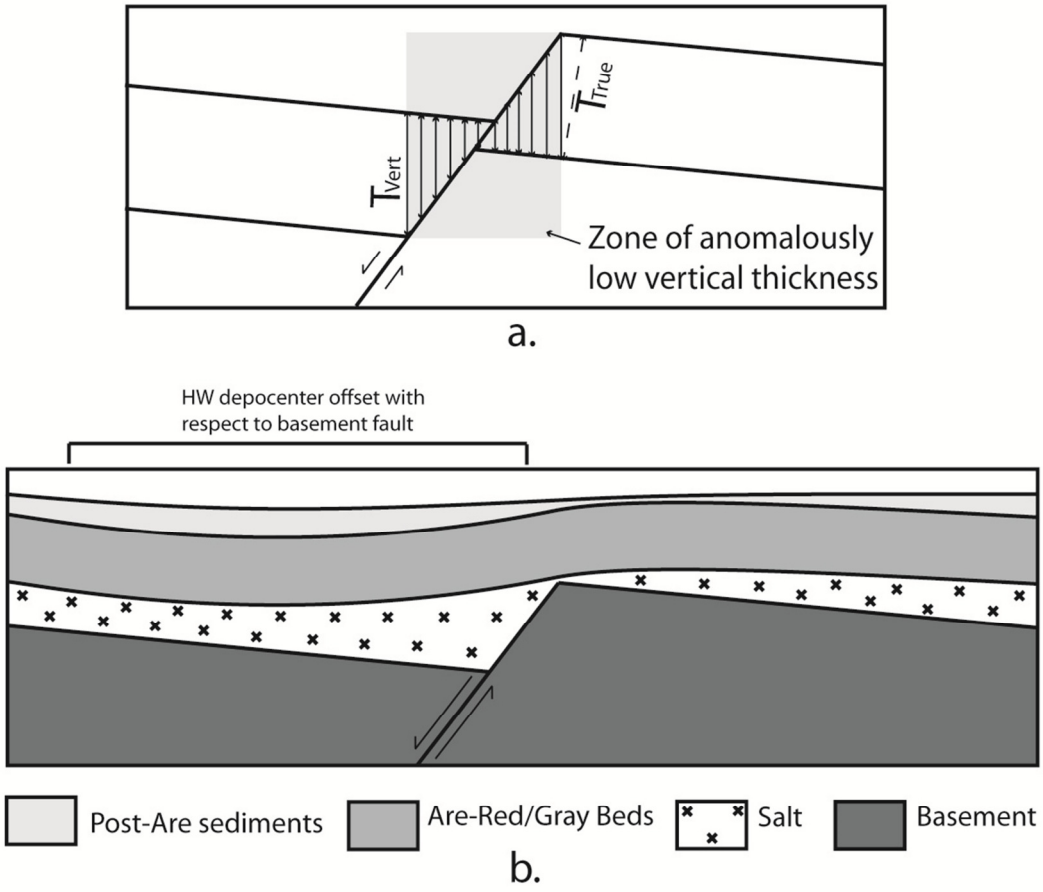

Figure 4.5 a. Schematic cross section of units adjacent to a fault showing the limitation of determining vertical thickness on a fault. Note the zone of anomalously low vertical thickness on the fault. Also note that for most dipping horizons vertical thickness is always higher than true thickness ($T_{vert}>T_{true}$). b. Schematic cross section showing the offset relation of the basement fault and the hanging wall depo-center associated with it.

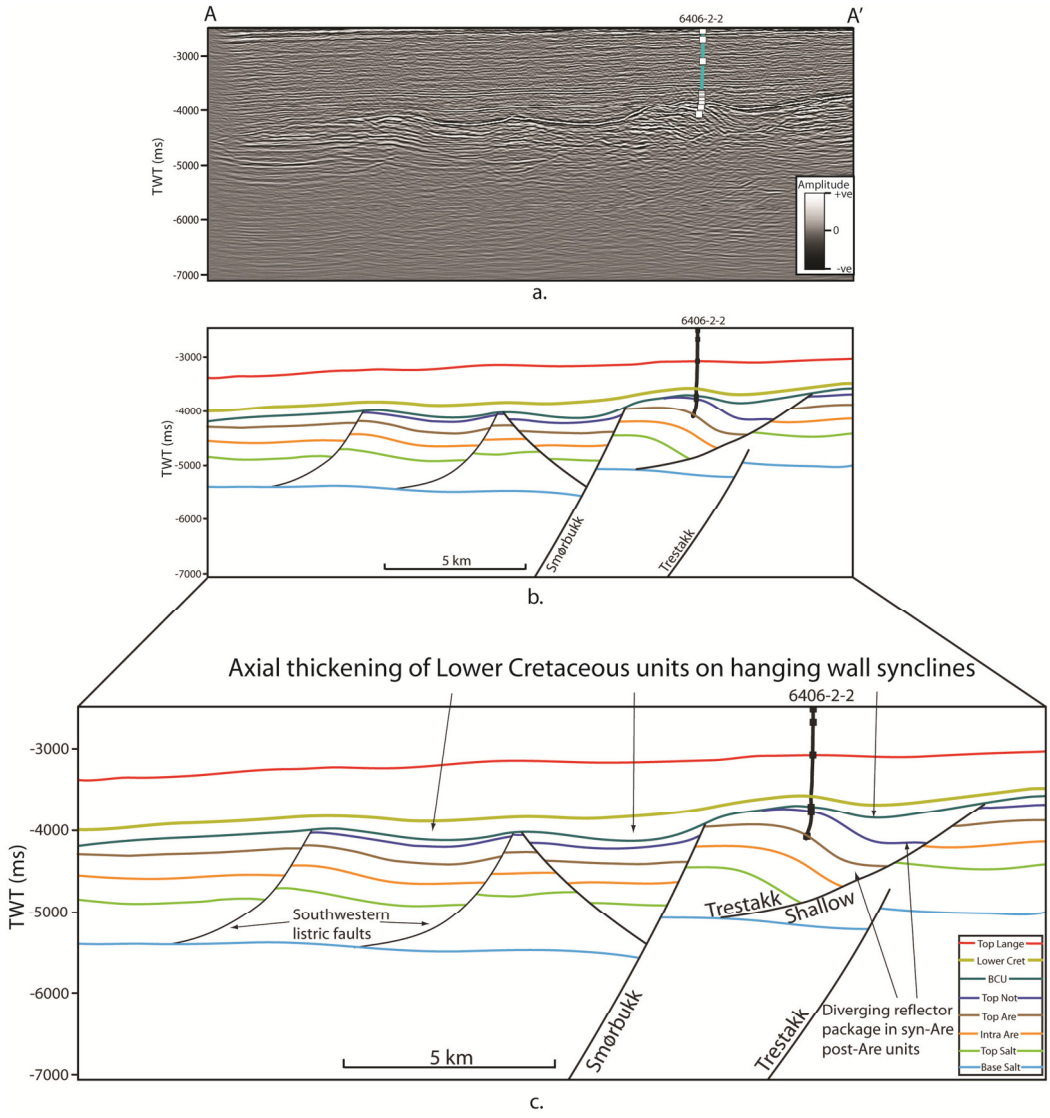

Figure 4.6 Uninterpreted (a) and interpreted (b and c) time section showing the structural geometry of the faults and key marker horizons along Inline 1820 towards the southern part of the study area (Refer to Figure 4.3 for location). Note (in the blown out interpreted section in c) that growth related thickness variation is more prominent to the post- Åre units for most of the faults. Growth geometry within syn- Åre units is observed only along the Trestakk Shallow fault. Axial thickening of the Lower Cretaceous units on the hanging wall synclines of the major faults is related to the late movement of the faults during the post-rift (HT3) phase.

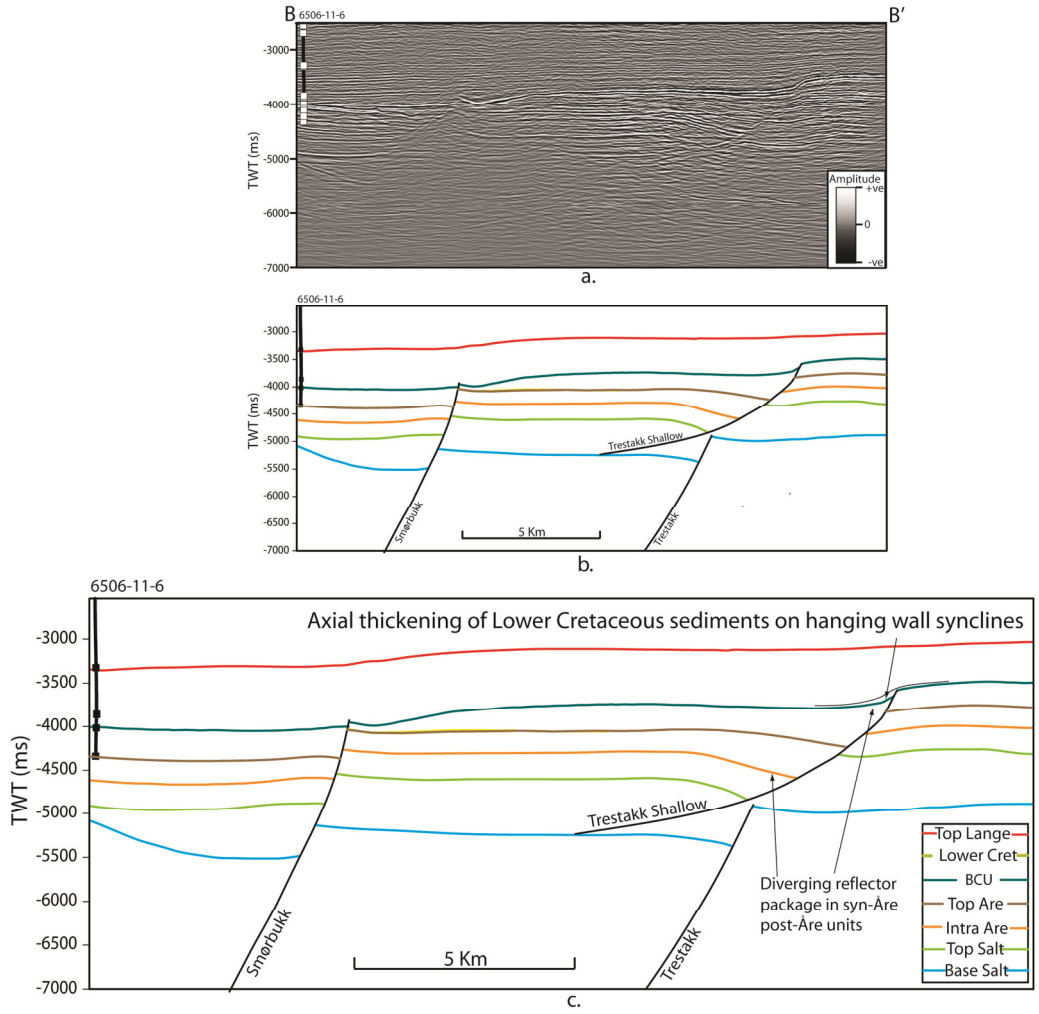

Figure 4.7 Uninterpreted (a) and interpreted (b and c) time section showing the structural geometry of the faults and key marker horizons along Inline 3180 towards the south-central part of the study area (Refer to Figure 4.3 for location). In the blown out interpreted section in c. note the truncation of the Top of Salt horizon against the Base of Salt horizon probably due to salt withdrawal and flow into the Smørbukk hanging wall. The Trestakk Shallow is the single fault in this section that shows majority of growth within Åre to immediate post-BCU interval.

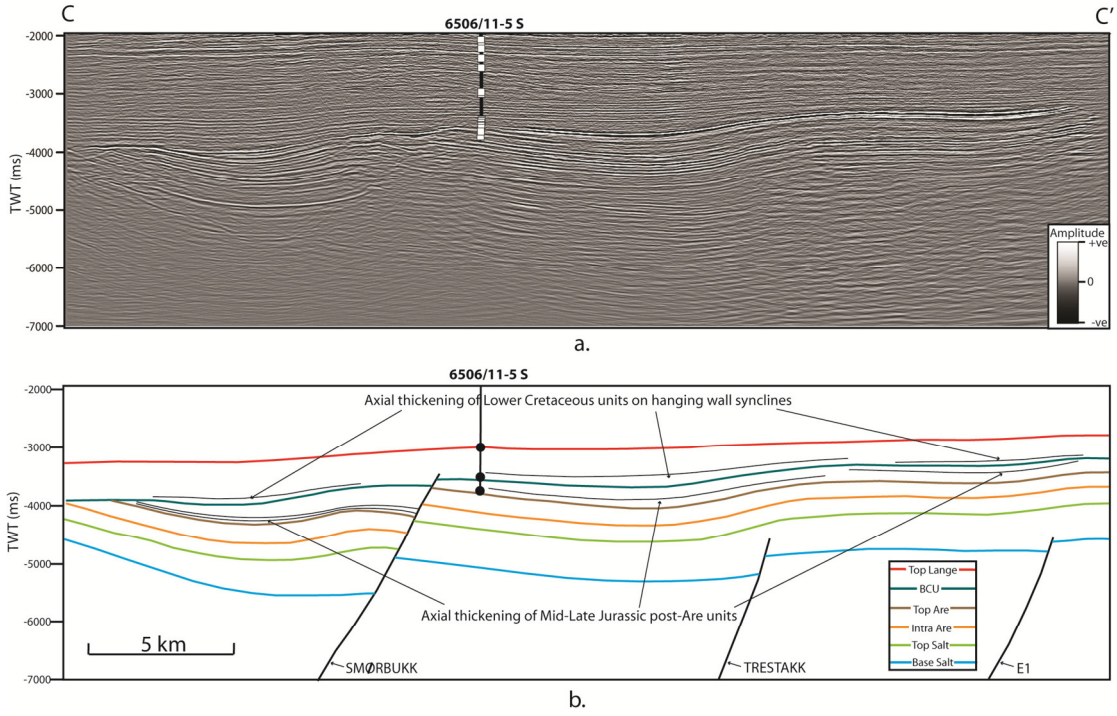

Figure 4.8 Uninterpreted (a) and interpreted (b) time section showing the structural geometry of the faults and key marker horizons along Inline 4100 towards the north-central part of the study area (Refer to Figure 4.3 for location). In b. note the absence of any basement-detached faults in this section. The thickness difference in the salt unit towards the western side of the section is attributed to the flow of salt probably in response to the movement on the hard linked Smørbukk fault. Towards the central and eastern part of the section synclinal depocenters within the post- Åre units are related to the late movement on the buried Trestakk and E1 faults.

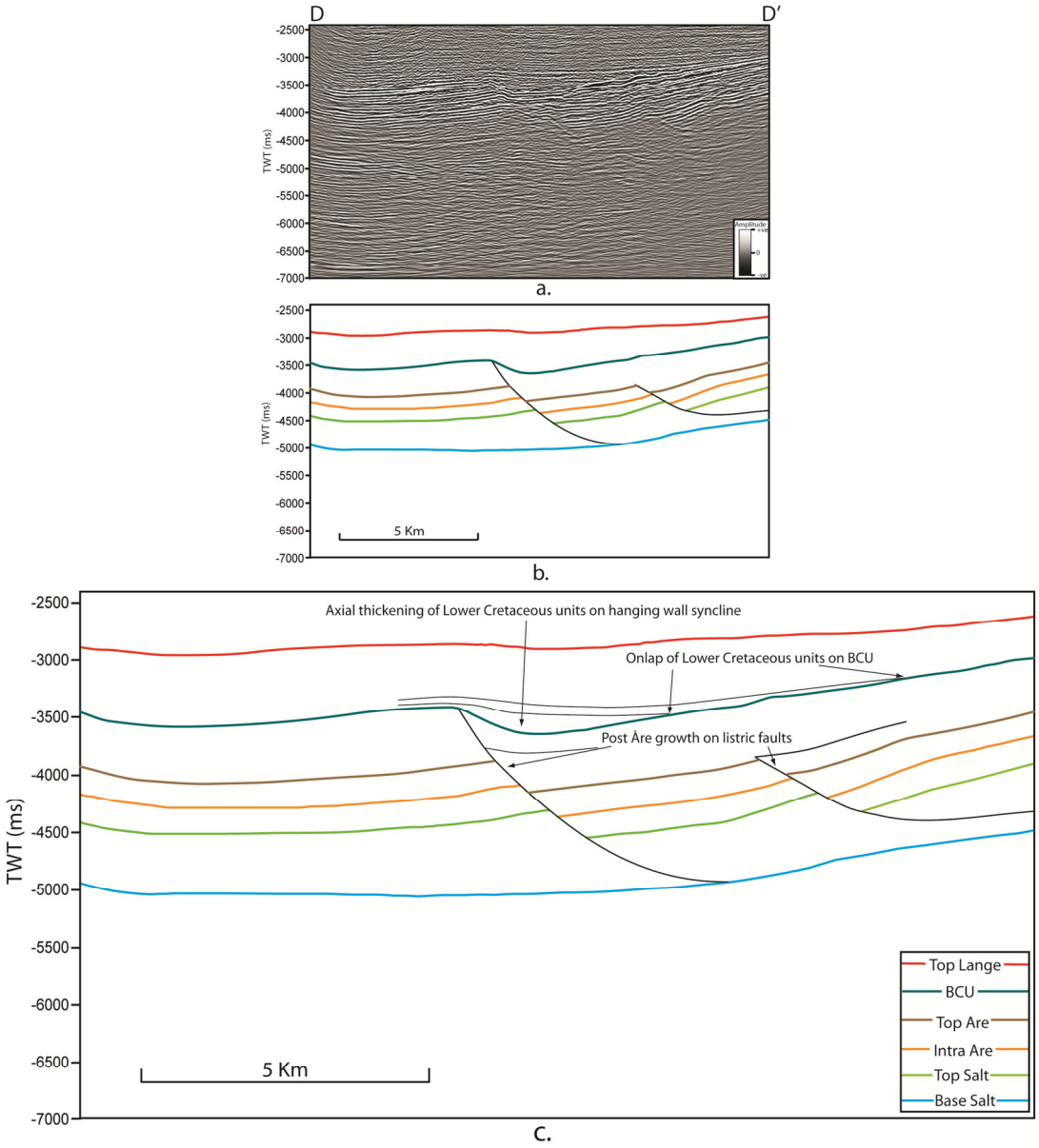

Figure 4.9 Uninterpreted (a) and interpreted (b and c) time section showing the structural geometry of the faults and key marker horizons along Inline 5820 towards the northern part of the study area (Refer to Figure 4.3 for location). In the blown out interpreted section in c note the change in polarity of the basement-detached faults in this section. Growth related thickness change within the Jurassic interval is more for the post- Åre units. Axial thickening of the lower Cretaceous units on the hanging wall syncline of the central listric fault and the onlap of the reflectors against the BCU horizon suggest episodic movement on this fault.

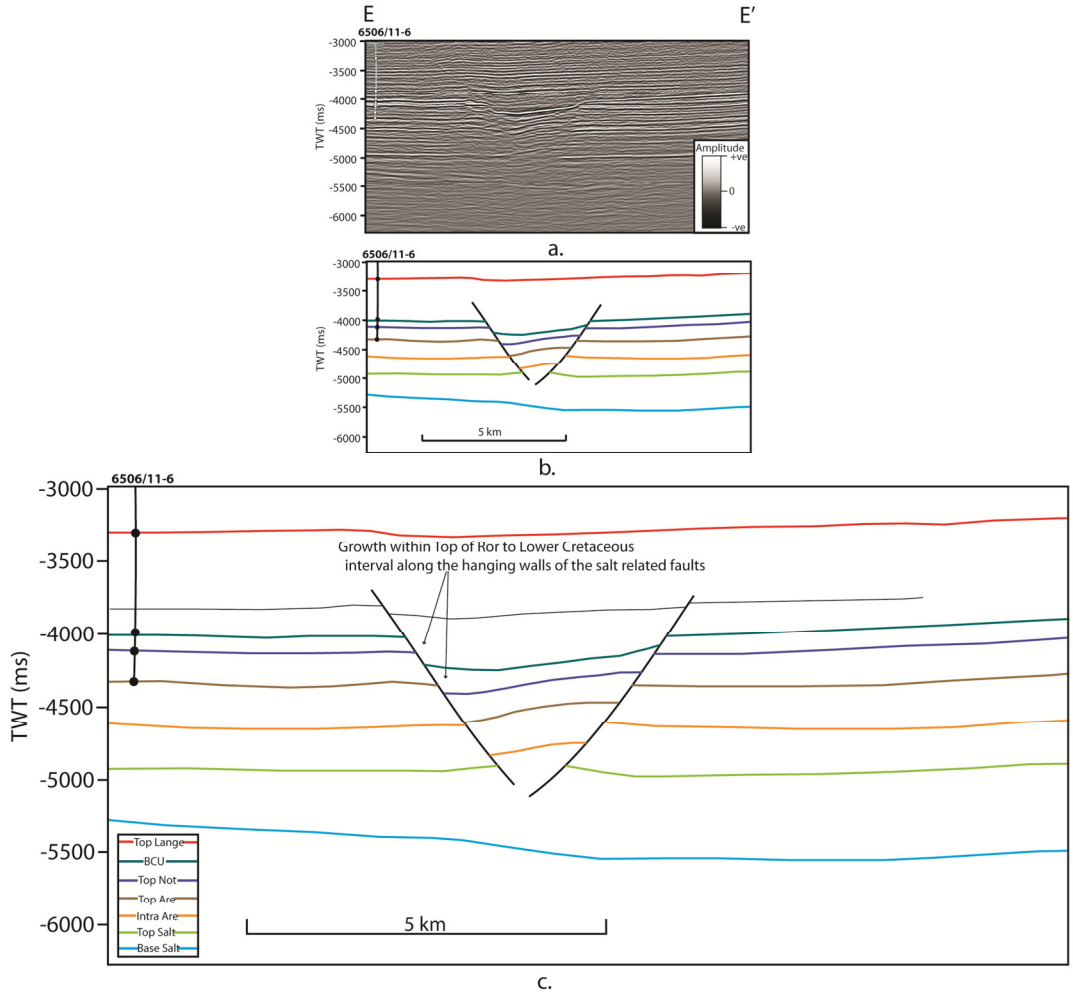

Figure 4.10 Uninterpreted (a.) and interpreted (b and c) time section showing the structural geometry of the faults and key marker horizons along the strike line EE' towards the western part of the study area (Refer to Figure 4.3 for location). In the blown out interpreted section in c the conjugate faults that detach within the salt unit are interpreted to have originated from gravity driven flow of salt triggered by the tilting of basement (Marsh et al., 2010). Growth geometries associated with these faults are restricted to the post-Top of Not units.

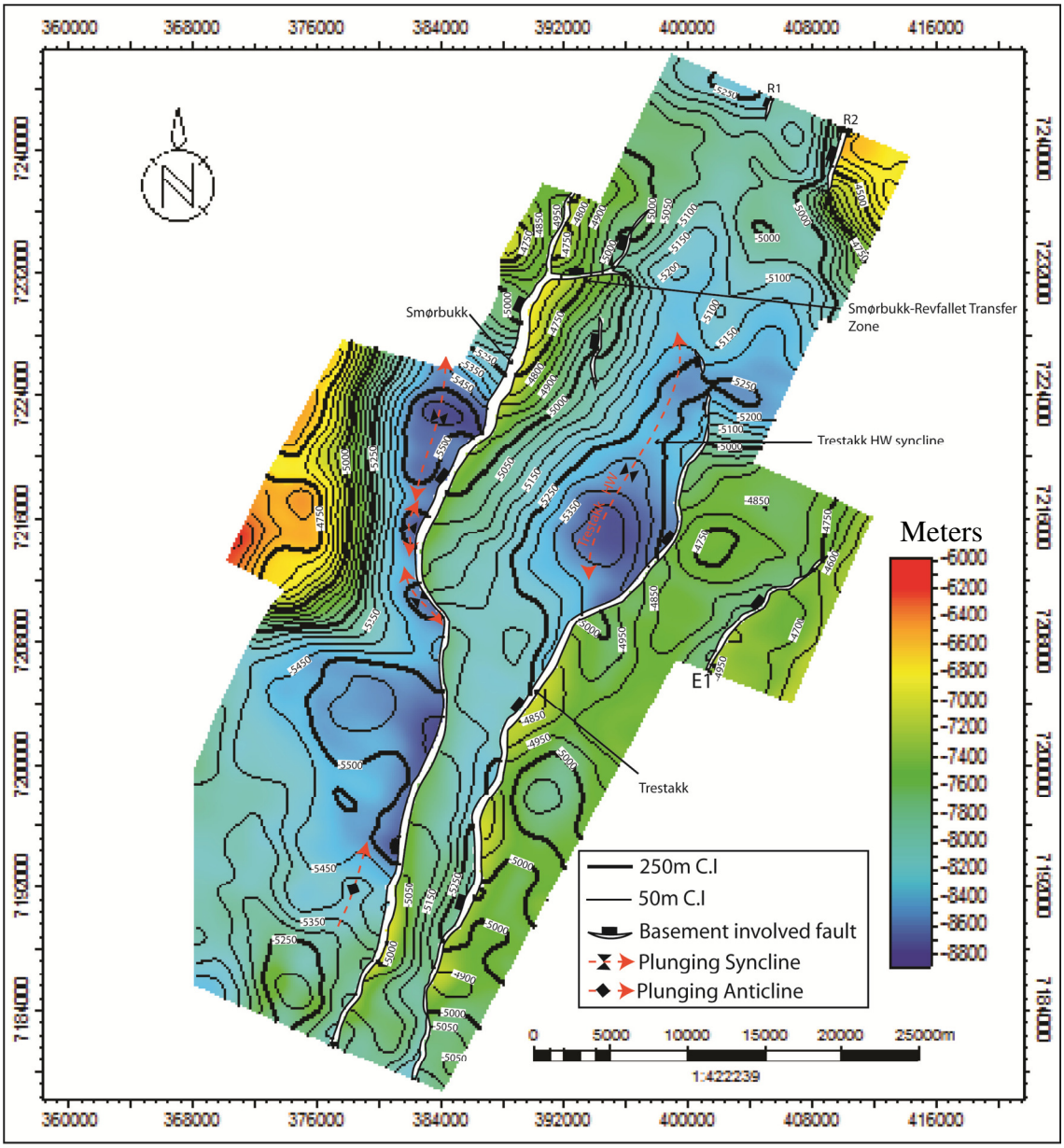

Figure 4.11 Depth structure map of the Middle Triassic Base of Salt horizon showing the major basement-involved faults and the structures associated to them. The presence of the hanging wall synclines related to these faults attests to the sedimentary nature of the basement. Note in this figure and in the three subsequent figures the oblique geometry of the Smørbukk-Revfallet transfer system.

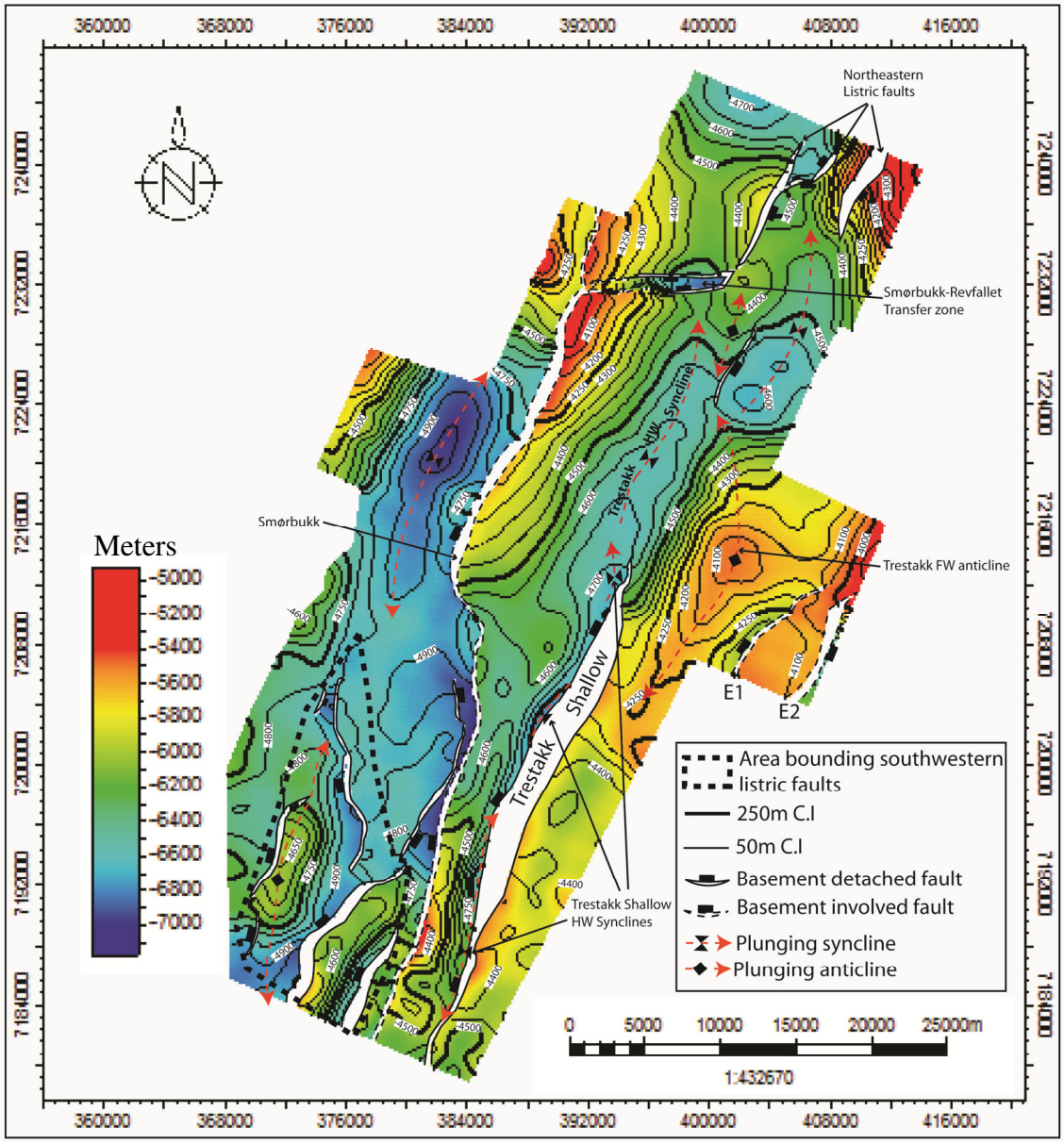

Figure 4.12 Depth structure map of the Late Triassic Top of Salt horizon showing the major faults that displace it and the structures associated with them. Fault polygons for the basement-involved faults are marked with dashed lines and those for the basement-detached faults are marked with solid lines. The strike variation of the faults ranges from NNE-SSW to NNW-SSE. Note the presence of a separate Trestakk hanging wall syncline in the north central part of the study area where the Trestakk Shallow fault is absent.

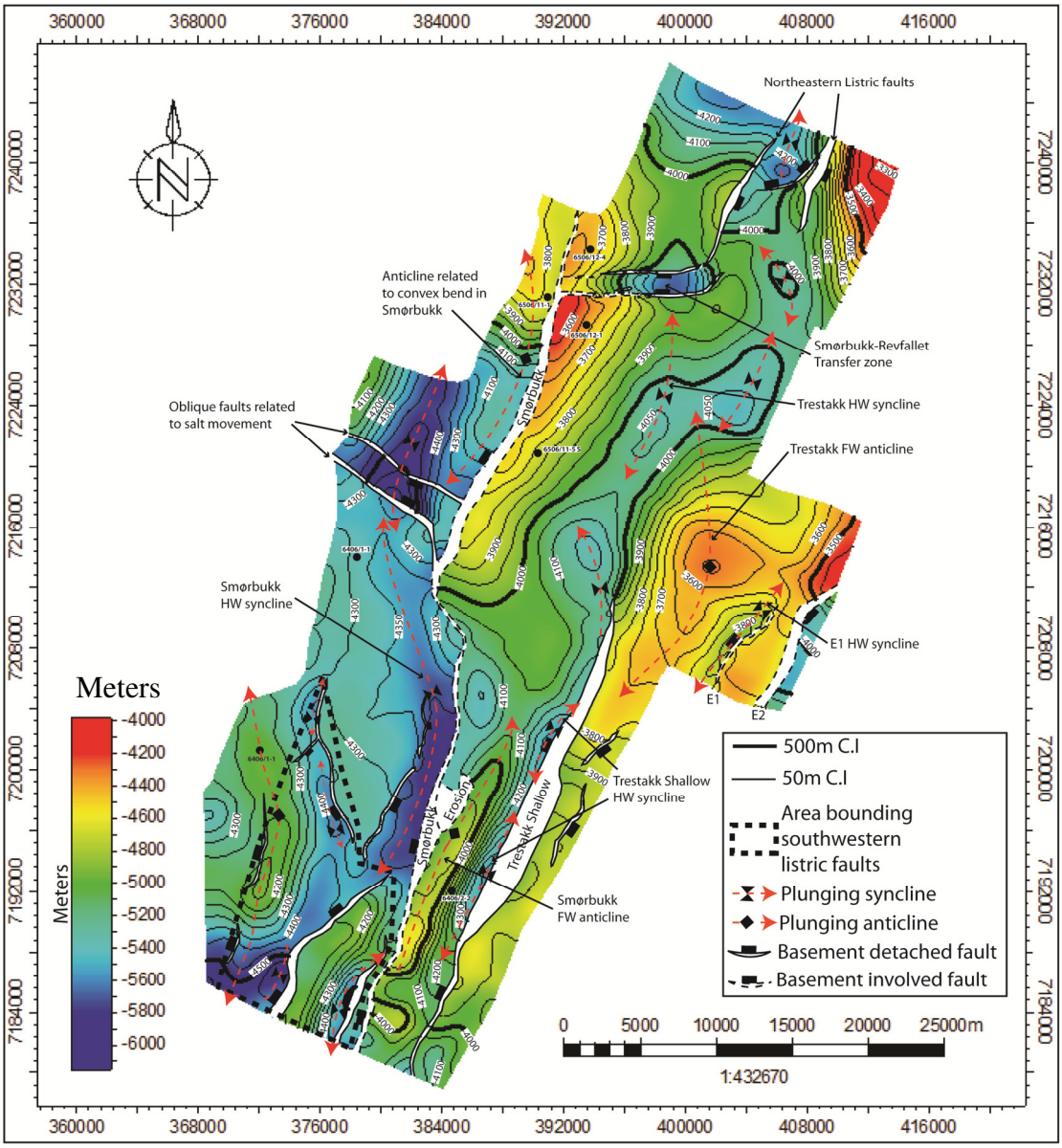

Figure 4.13 Depth structure map of the Early Jurassic Top of Åre horizon showing the major faults that displace it and the structures associated with them. Fault polygons for the basement-involved faults are marked with dashed lines and those for the basement-detached faults are marked with solid lines. Note the difference in trend between the Trestakk Shallow hanging wall syncline in the central part and the Trestakk hanging wall syncline in the north-central part of the study area. But for the addition of the two oblique salt related faults towards the west the overall strike variation of the faults still varies from NNE-SSW to NNW-SSE.

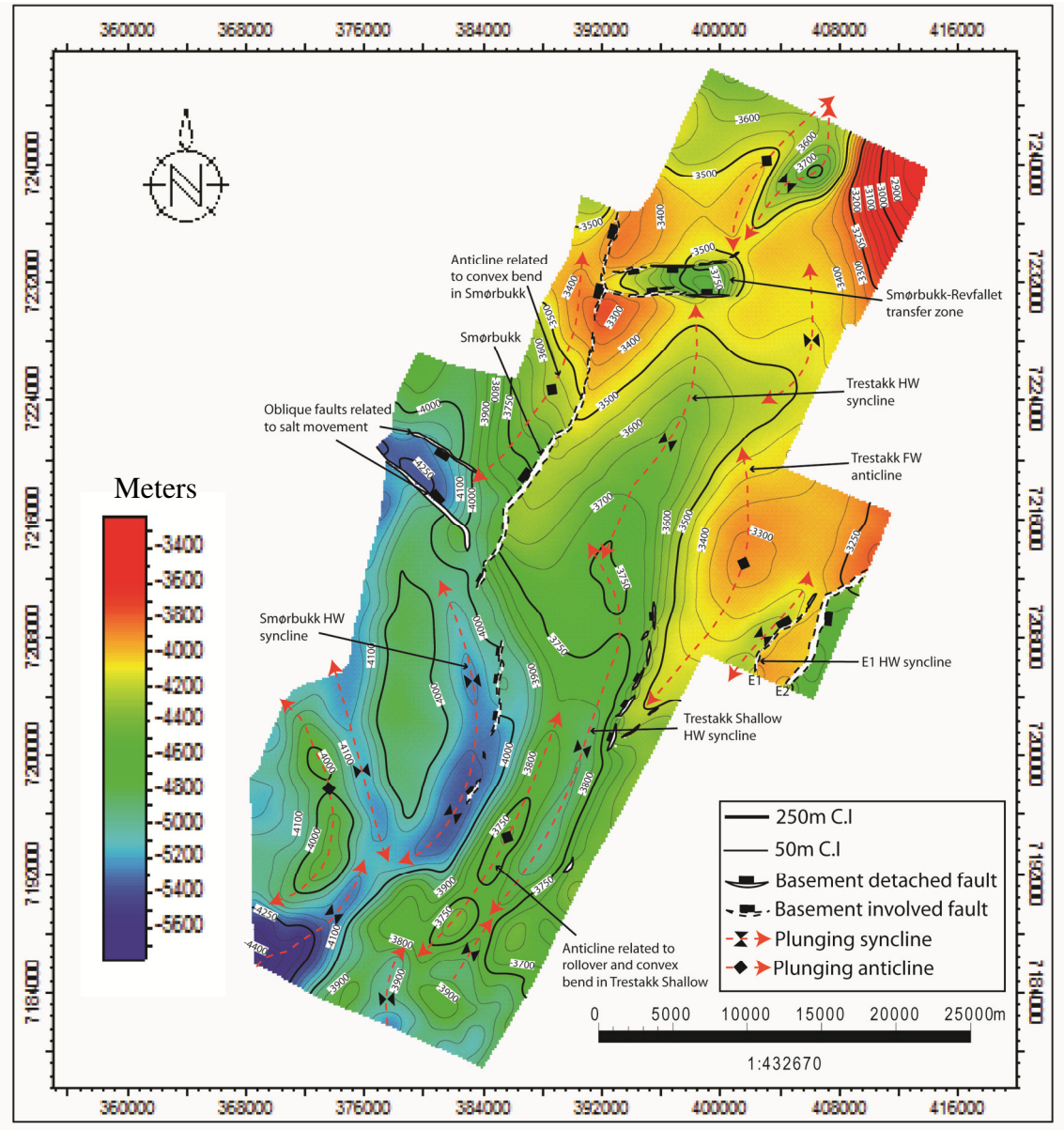

Figure 4.14 Depth structure map of the BCU (Base of Cretaceous Unconformity) horizon showing the major faults that displace it and the structures associated with them. Fault polygons for the basement-involved faults are marked with dashed lines and those for the basement-detached faults are marked with solid lines. The structural orientation of the faults and related folds remain similar to those mapped on the Top of Åre horizon in Figure 4.13. The overall lack in the number of faults displacing this horizon and the discontinuous geometry of the faults that actually displaces it points to the decrease in extensional activity during the lower Cretaceous time.

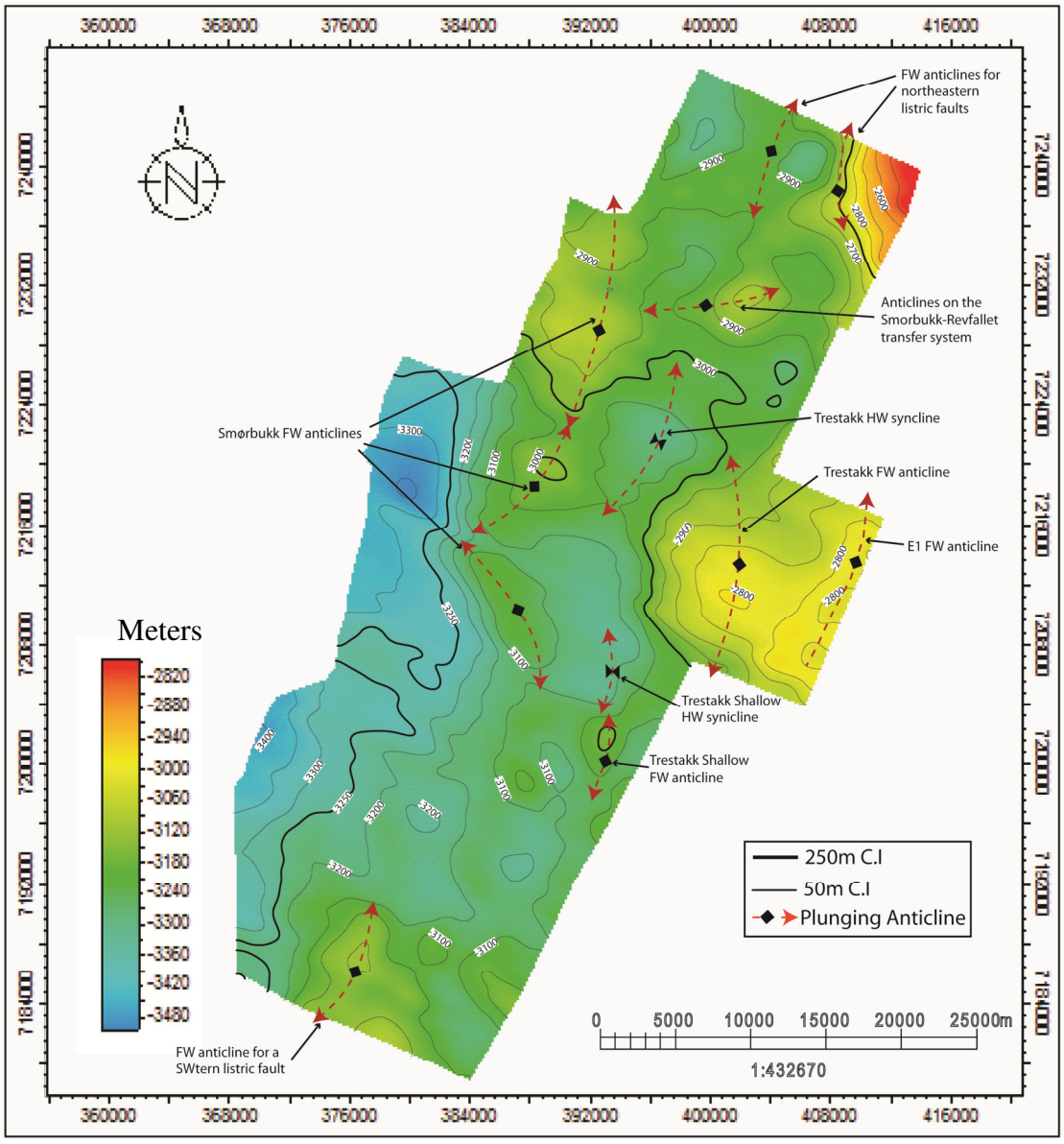

Figure 4.15 Depth structure map of the Lower Cretaceous Top of Lange horizon. Note that this this horizon is not displaced by any faults and represents a late post-rift (HT3) stage. The approximate positions of the anticlines and synclines related to the blind faults partially active below this horizon are shown by red dashed lines. The overall trend of these structures is similar to those mapped on the horizons below it (Figures 4.12, 4.13 and 4.14).

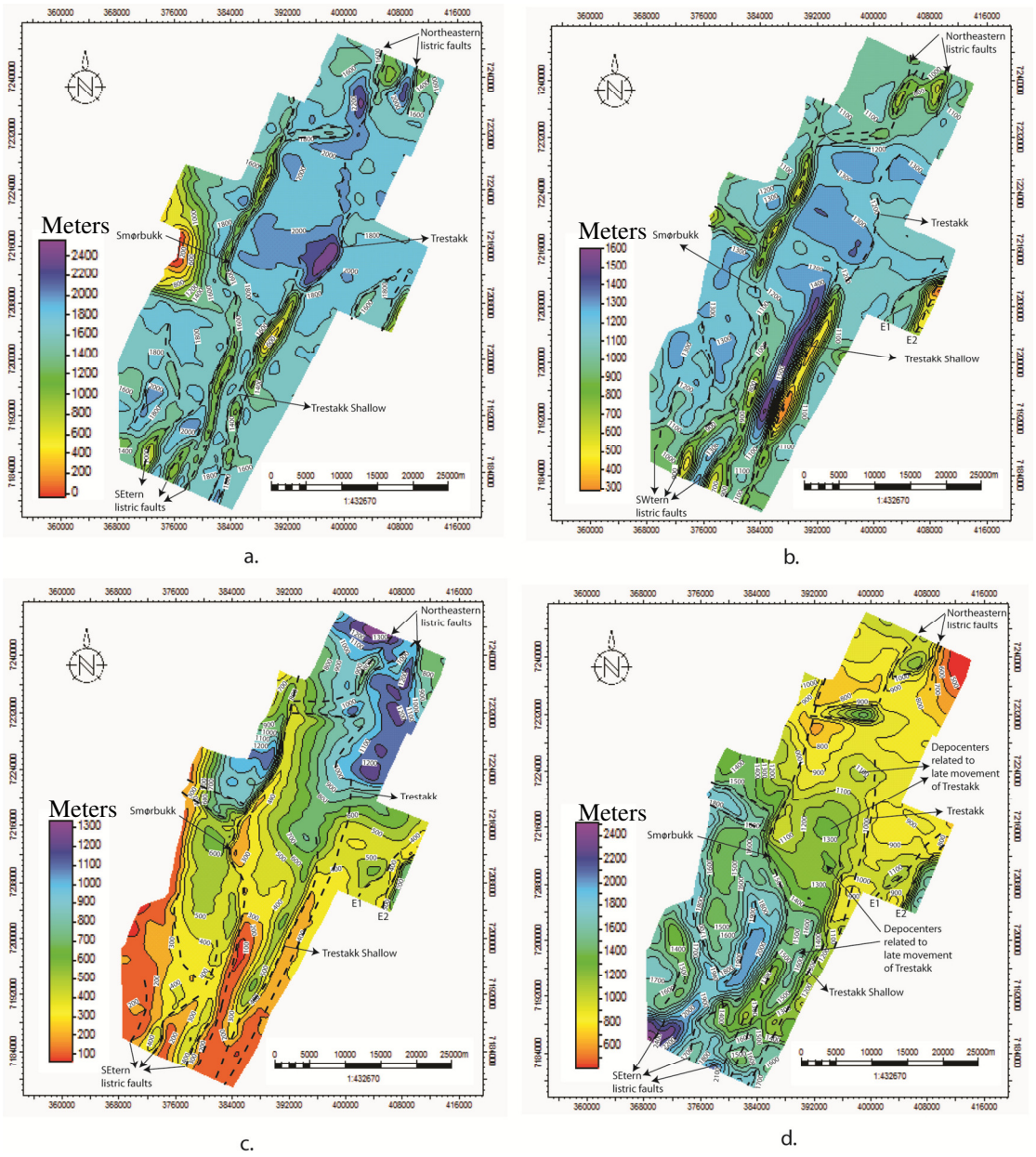

Figure 4.16 Isochore maps between different intervals. Increase in vertical thickness is interpreted to be related to growth along faults. The curvilinear zones of anomalously low vertical thickness correspond to the position of the faults (refer to Figure 4.5 for the origin of the low vertical thickness zones). The approximate positions of the faults are shown in black dashed lines. a. Isochore map between Base of Salt and Top of Salt horizons. Zones of high vertical thickness right adjacent to the major faults are attributed to the flow of salt. b. Isochore map between the Top of Salt and the Top of Åre horizons. Note the curvilinear zone of growth related high vertical thickness right adjacent to the Trestakk Shallow fault. c. Isochore map between the Top of Åre and BCU horizons. Highest vertical thickness is still in the hanging wall depo-centers related to the Trestakk Shallow fault. However increase in vertical thickness along the hanging walls of the other faults is more prominent in this map than in b. Note the separate depo-centers for the Trestakk Shallow and the Trestakk faults. d. Isochore between BCU and the Top of Lange horizons. Fault related depo-centers are still prominent in this Lower Cretaceous interval.

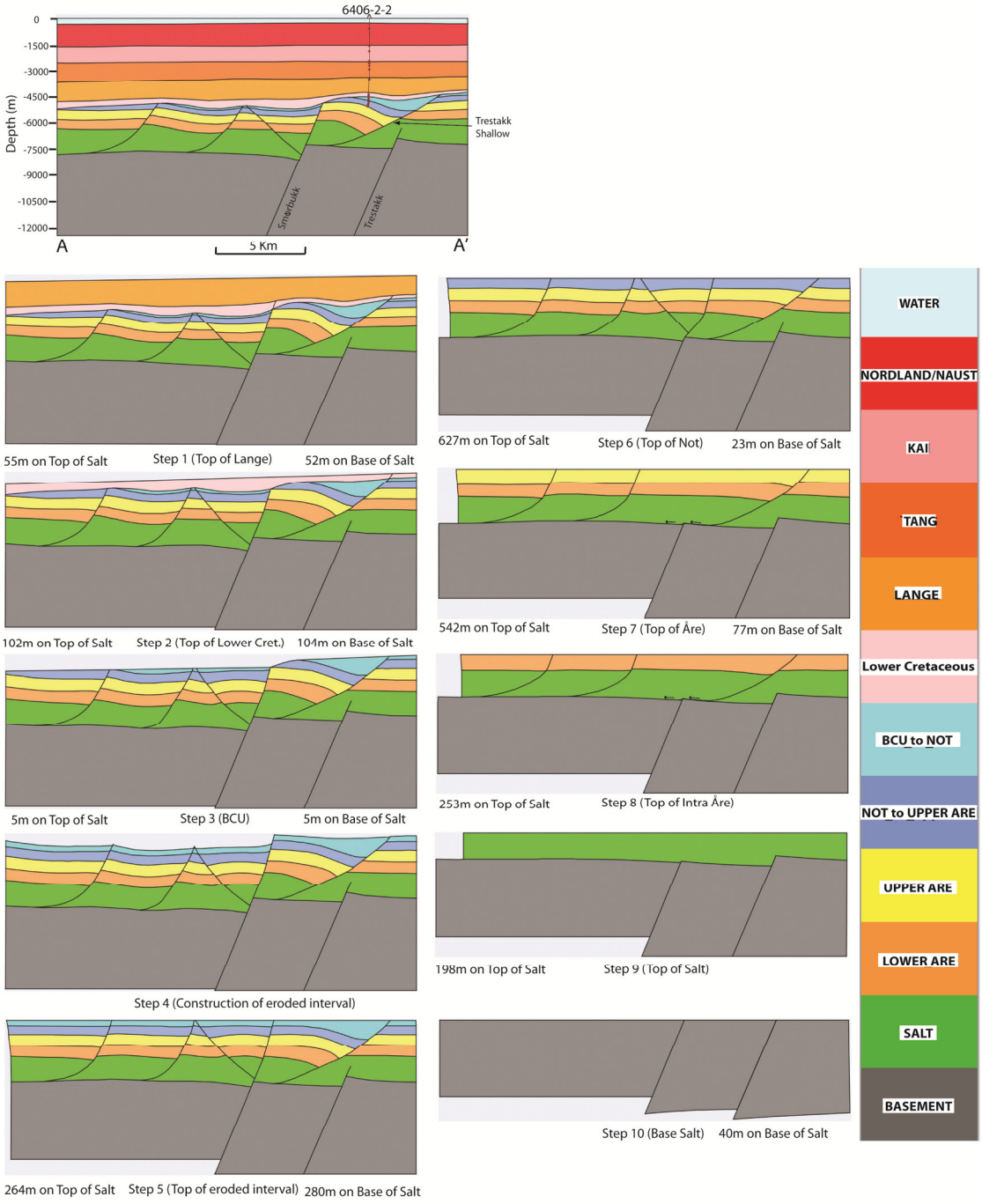

Figure 4.17 Depth section along AA' (Inline 1820; see Figure 4.3 for location) and stepwise iteration of decompaction and structural restoration. The amount of extension yielded from each step is measured on the Top of Salt and on the Bottom of Salt horizons and is shown at the bottom of each step. The stratigraphic column used for the restoration is shown on the right. See text for detailed explanation of each step.

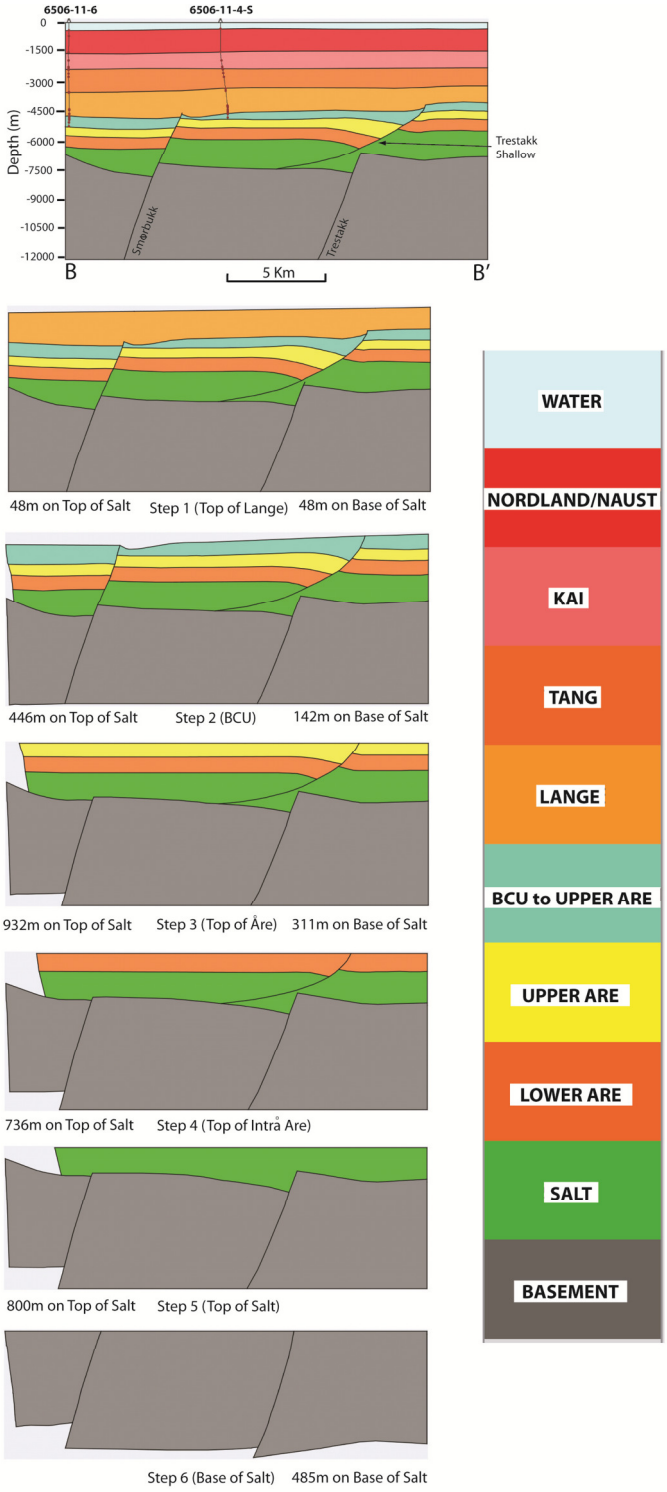

Figure 4.18 Depth section along BB' (Inline 3180; see Figure 4.3 for location) and stepwise iteration of decompaction and structural restoration. The amount of extension yielded from each step is measured on the Top of Salt and on the Bottom of Salt horizons and is shown at the bottom of each step. The stratigraphic column used for the restoration is shown on the right. See text for detailed explanation of each step.

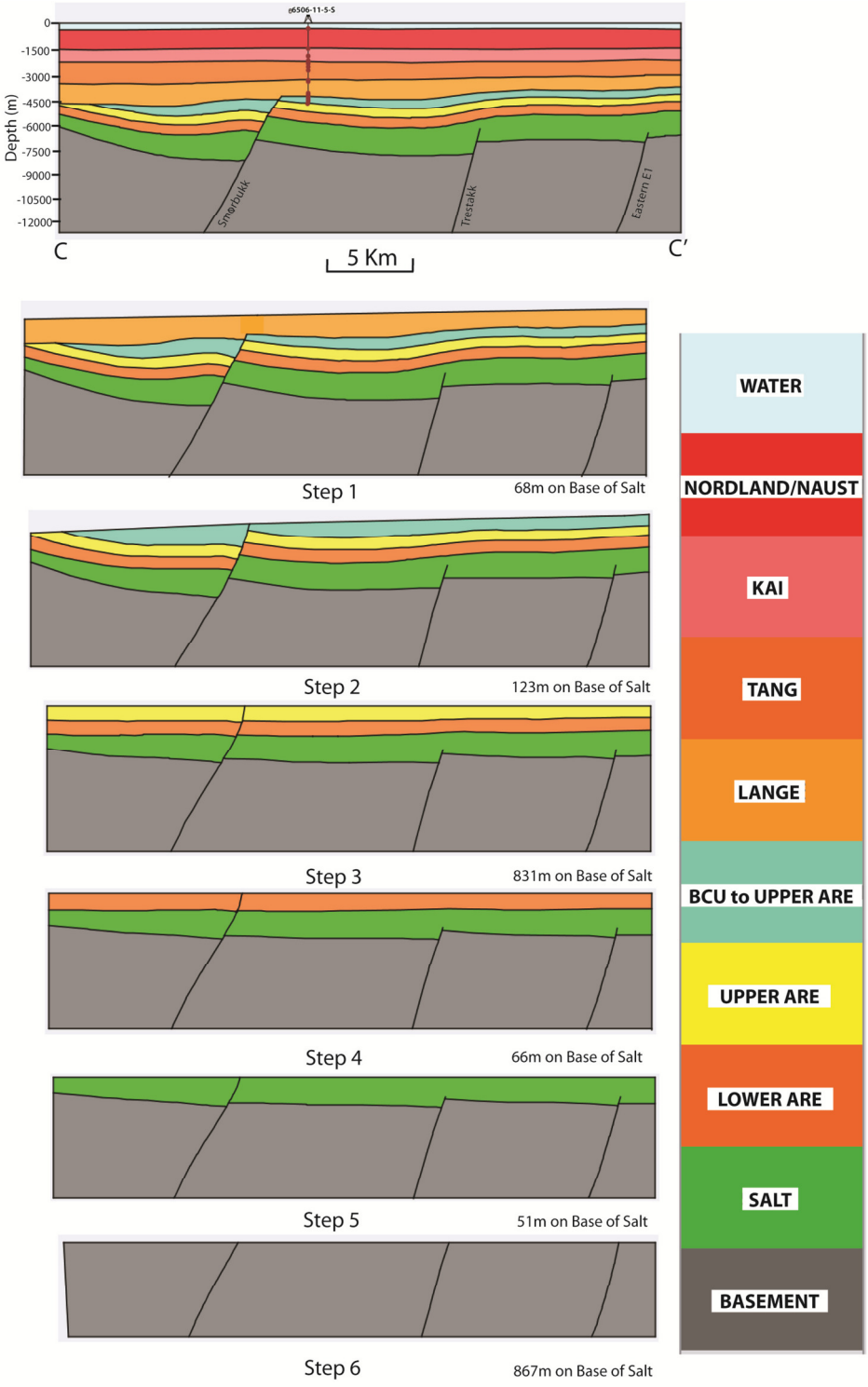

Figure 4.19 Depth section along CC' (Inline 4100; see Figure 4.3 for location) and stepwise iteration of decompaction and structural restoration. The amount of extension yielded from each step is measured only on the Bottom of Salt horizon and is shown at the bottom of each step. The stratigraphic column used for the restoration is shown on the right. See text for detailed explanation of each step.

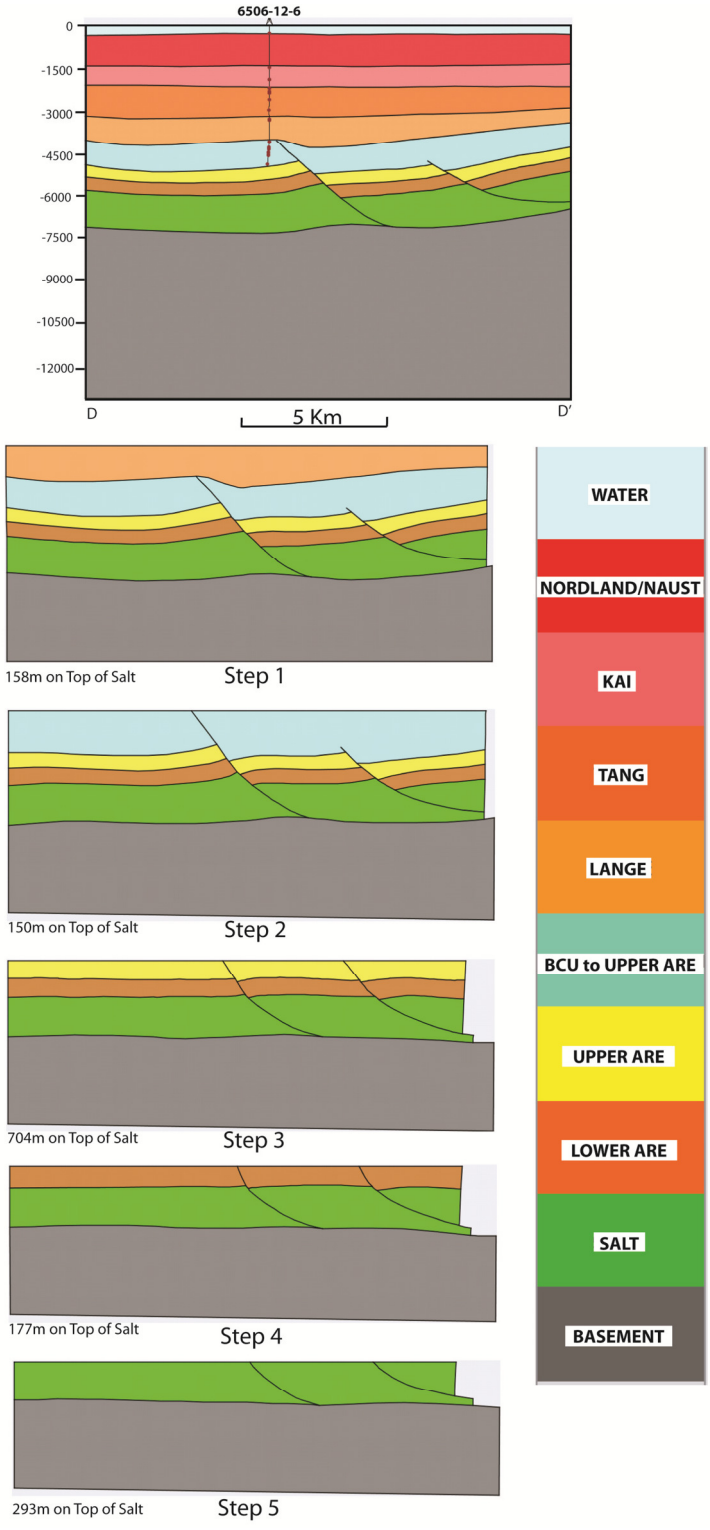

Figure 4.20 Depth section along DD' (Inline 5820; see Figure 4.3 for location) and stepwise iteration of decompaction and structural restoration. The amount of extension yielded from each step is measured on the Top of Salt and on the Bottom of Salt horizons and is shown at the bottom of each step. The stratigraphic column used for the restoration is shown on the right. See text for detailed explanation of each step.

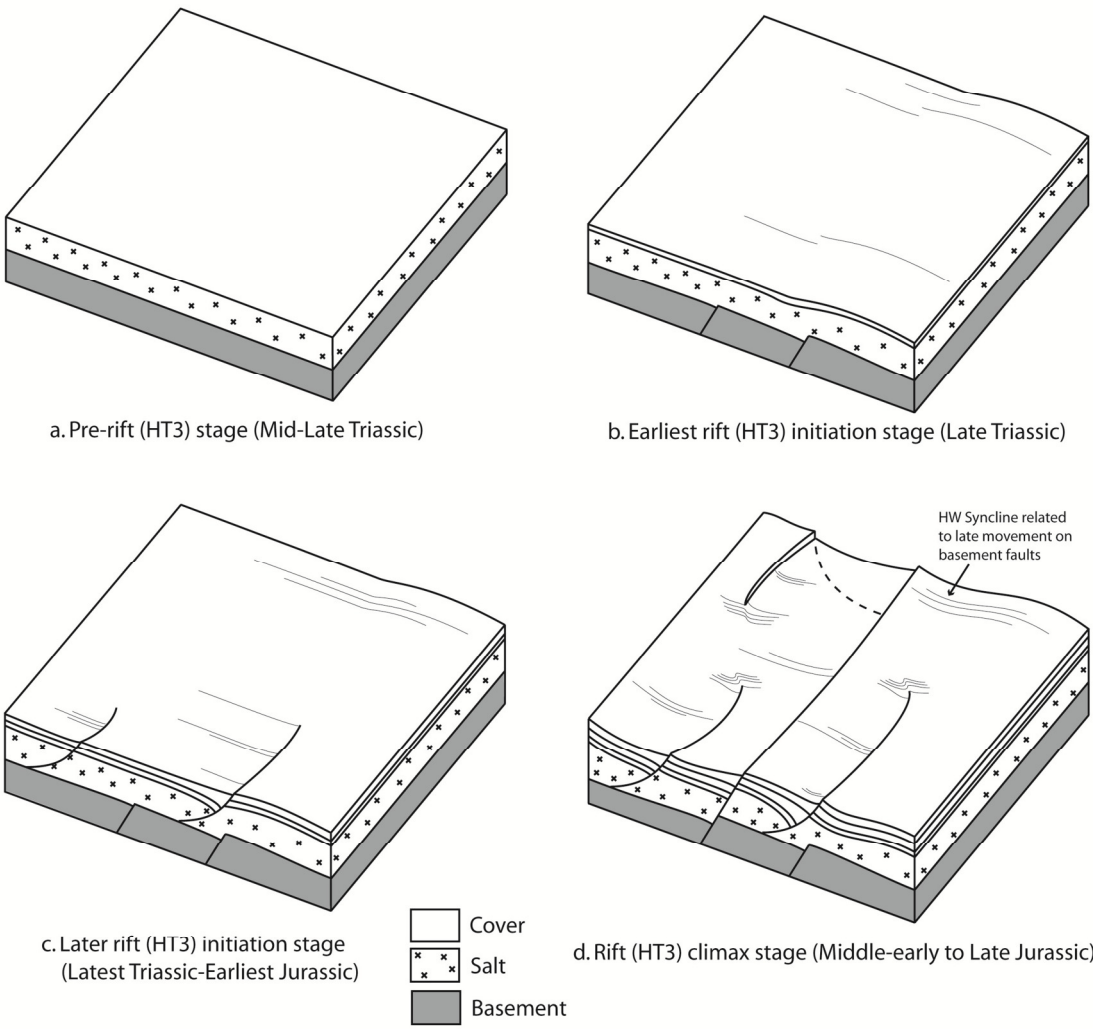

Figure 4.21 Schematic block diagrams showing the progressive evolution of the basement-involved and the basement-detached faults over time in the study area. a. Initial layer parallel geometry during the pre-rift (HT3) stage. b. Earliest rift initiation stage during late Triassic time resulting in the first phase of activity of the basement faults. c. Development of basement-detached faults during the later major part of the rift initiation stage. The position of the basement-detached fault with higher displacement is somewhat constrained by the blind basement faults below it. The position of the smaller basement fault is unconstrained by any basement fault below it. d. Further growth of existing faults, hard linking of basement fault and development of new basement-detached faults during the rift climax stage. Note the difference in the trends of the hanging wall synclines for the basement-detached faults and the blind basement fault active in this stage.

Faults	Activity	
Basement Involved	No. of phases	Time of Activity
Smørbukk (hardlinked)	2	1. Late Triassic 2. Early Jurassic to Early Cretaceous
Trestakk	2	1. Late Triassic 2. Early Jurassic to Early Cretaceous
Eastern E1 (hardlinked)	2	1. Late Triassic 2. Early Jurassic to Early Cretaceous
Northern R1	1	1. Late Triassic
Northern R2	2	1. Late Triassic 2. Late Jurassic to Early Cretaceous
Smørbukk-Revfallet Transfer Zone	1 (uncertain)	1. Late Jurassic to Early Cretaceous (uncertain)
Basement Detached		
Trestakk Shallow	1	1. Latest Triassic to Lower Cretaceous
SWtern listric faults	1	1. Early Jurassic to Lower Cretaceous
Western oblique listric faults	1	1. Mid Jurassic to Lower Cretaceous
Listric faults above R1 and R2	1	1. Early Jurassic to Lower Cretaceous
Listric faults on Smørbukk-Revfallet Transfer Zone	1	1. Early Jurassic to Lower Cretaceous (uncertain)

Table 4.1 Summary of activity of the basement-involved and the basement-detached faults in the study area.

Addendums

Dix (1955) Equation: Given V_{RMS} and T_0 for the top and bottom of the k[th] layer in a stack of layers within the earth's surface as shown below

The interval velocity is obtained from the Dix Equation:

$$V_k = \sqrt{\frac{V_{RMS,k+1}^2 T_{0,k+1} - V_{RMS,k}^2 T_{0,k}}{T_{0,k+1} - T_{0,k}}}$$

Wells with checkshot data:

Well	Latitude	Longitude	KB (m)	TD (m)
6406-1-1	64°54'34.3"N	6°17'40.8"E	24	5057
6406-3-2	64°51'52.5"N	6°49'51"E	22	4513
6406-3-4	64°53'05.9"N	6°50'47.6"E	29	4380
6506-11-1	65°11'10.3"N	6°39'53"E	29	4657
6506-12-1	65°10'13.4"N	6°43'43.1"E	22	4939
6506-12-4	65°12'52.8"N	6°43'29.4"E	25	4437

Summary of Interval Velocities:

Profile	Formation	Interval Vel(m/s)	**Solidity**
Inline 1820	Water	1475	Water
Inline 1820	Nordland/Naust	2170	Sand50/Shale50
Inline 1820	Kai	2138	Sand
Inline 1820	Tang	2386	Shale
Inline 1820	Lange	3584	Shale
Inline 1820	BCU to Not	3605	Shale
Inline 1820	Not to Upper Are	2607	Sand50/Shale50
Inline 1820	Upper Are	3588	Shale33/Sand33/Carbonate33
Inline 1820	Lower Are	4077	Shale33/Sand33/Carbonate34
Inline 1820	Salt	4600	Salt
Inline 1820	Basement	5800	Solid
Inline 3180	Water	1475	Water
Inline 3180	Nordland/Naust	2173	Sand50/Shale50
Inline 3180	Kai	2136	Sand
Inline 3180	Tang	2381	Shale
Inline 3180	Lange	3589	Shale
Inline 3180	BCU to Upper Are	3029	Shale
Inline 3180	Upper Are	3593	Shale33/Sand33/Carbonate33
Inline 3180	Lower Are	4071	Shale33/Sand33/Carbonate34
Inline 3180	Salt	4600	Salt
Inline 3180	Basement	5800	Solid
Inline 5820	Water	1475	Water
Inline 5820	Nordland/Naust	2221	Sand50/Shale50
Inline 5820	Kai	2172	Sand
Inline 5820	Tang	2422	Shale
Inline 5820	Lange	2884	Shale
Inline 5820	BCU to Upper Are	3639	Shale
Inline 5820	Upper Are	3743	Shale33/Sand33/Carbonate33
Inline 5820	Lower Are	3838	Shale33/Sand33/Carbonate33
Inline 5820	Salt	4600	Salt
Inline 5820	Basement	5800	Solid

Seismic velocities for the basement were obtained from Breivik et al., 2009.

Average Velocity vs. Depth plots for checkshot wells:

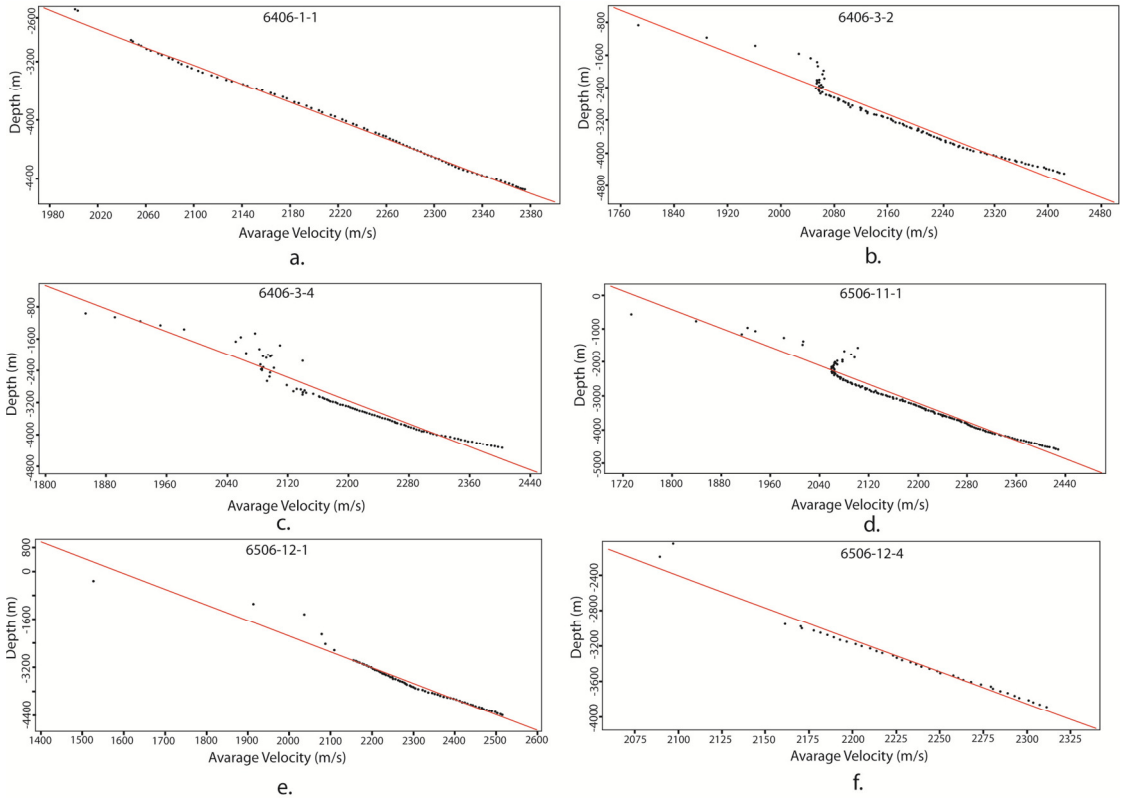

References

Blystad, P., H. Brekke, R. Faerseth, B.T. Larsen, J. Skogseid and B. Torudbaken, 1995, Structural elements of the Norwegian Continental Shelf, Part II: The Norwegian Sea Region: Norwegian Petroleum Directorate Bulletin, v.8, 45p.

Brown, R. N., 1980, History of exploration and discovery of Morgan, Ramadan, and July oilfields, Gulf of Suez, Egypt, *in*, A. D. Miall, ed., Facts and principles of world petroleum occurrence: Canadian Society of Petroleum Geologists, Memoir 6, p. 733-764.

Breivik, A.J., Faleide, J.I., Mjelde, R., and Flueh, E.R. (2009) Magma Productivity and Early Seafloor Spreding Rate Correlation on the Northern Vøring Margin, Norway – Constraints on Mantle Melting: *Tectonophysics*, v. 468, p. 206-223.

Buckovics, C. and P.A. Ziegler, 1985, Tectonic development of the Mid-Norway continental margin: Marine and Petroleum Geology, v.2, p.2-22.

Colleta, B., P. Le Quellec, J. Letouzey, and Moretti, 1988, Longitudinal evolution of the Suez rift structure (Egypt): Tectonophysics, v. 153, p. 221-233.

Corfield, S. and I. R. Sharp, 2000, Structural style and stratigraphic architecture of fault propagation folding in extensional settings: a seismic example from the Smørbukk area, Halten Terrace, Mid-Norway: Basin research, v.12, p.329-341.

Davy, P., A. Hansen, E. Bonnet and Shou-Zhu Zhang, Localization and fault growth in layered brittle-ductile systems: Implications for deformations of the continental lithosphere: Journal of Geophysical Research, v.100, no.B4, p.6281-6294.

Dix, C.H., 1955, Seismic velocities from surface measurements: Geophysics, v.20, p.68-86.

Dooley, T., K. R. McClay and R. Pascoe, 2003, 3d analogue models of variable displacement extensional faults: applications to the Revfallet Fault system, offshore mid-Norway *in* Nieuwland, D. A. eds. New Insights into Structural Interpretation and Modeling: Geological Society, London, Special Publications, v.212, p.151-167.

Dore, A.G., E.R. Lundin, Ø. Birkeland, P.E. Eliassen and L.N. Jensen, 1997, The NE Atlantic Margin: implications of late Mesozoic and Cenozoic events for hydrocarbon prospectivity: Petroleum Geoscience, v.3, p.117-131.

Forbes, P.L., P.M Ungerer, A.B. Kuhfuss, F. Rills and S. Eggen, 1991, Compositional modeling of petroleum generation and expulsion: trial application to a Local Mass Balance in the Smørbukk Sør Field, Haltenbanken Area, Norway: AAPG Bulletin, v.75, no.5, p. 873-893.

Ehrenberg, S.N., H.M. Gjerstad and F. Hadler-Jacobsen, 1992, Smørbukk Field: A gas condensate fault trap in the Haltenbanken Province, Offshore Mid-Norway *in* M.T. Halbouty eds. Giant oil and gas fields of the decade 1978-1988: AAPG Memoir, v.54, p. 471-481.

Gibbs, A.D., 1983, Balanced cross-section construction from seismic sections in areas of extensional tectonics: Journal of Structural Geology, v.5, p.153-160.

Gupta, S., P. Cowie, N. Dawers and J.R. Underhill, 1998, A mechanism to explain rift-basin subsidence and stratigraphic patterns through fault-array evolution: Geology, v.26, p.595-598.

Higgins, R. I. and L. B. Harris, 1997, The effect of cover composition on extensional faulting above re-activated basement faults: results from analogue modeling: Journal of Structural Geology, v.19, no.1, p.89-98.

Klefstad, L., S. Kvarsvik, J.E. Ringas, J.J. Stene and O. Sundsby, 2005,Characterization of deeply buried heterolithic tidal reservoirs in the Smørbukk Field using inverted post-stack seismic acoustic impedance: Petroleum Geoscience, v.11, p.47-56.

Koyi, H., M. K. Jenyon and K. Petersen, 1993, The effect of basement faulting on diapirism: Journal of Petroleum Geology, v.16(3), p.285-312.

Marsh, N., J. Imber, R. E. Holdsworth, P. Brockbank and P. Ringrose, 2010, The structural evolution of the Halten Terrace, offshore Mid-Norway: extensional fault growth and strain localization in a multi-layer brittle-ductile system: Basin Research, v.22, p.195-214, doi: 10.1111/j.1365-2117.2009.00404.x

Nalpas, T. and J. P. Brun,1993, Salt flow and diapirism related to extension at crustal scale: Tectonophysics, v.228,p.349-362.

Pascoe, R., R. Hooper, K. Storhaug and H. Harper, 1999, Evolution of extensional styles at the southern termination of the Nordland Ridge, Mid-Norway: a response to variations in coupling above Triassic salt, *in* Fleet, A. J. and S. A. R. Boldy eds. Petroleum Geology of Northwestern Europe: Proceedings of the 5th Conference, v.5, p.83-90.

Petersen, K., O. R. Clausen and J. A. Korstgard, 1992, Evolution of a salt-related listric growth fault near the D-1 well, block 5605, Danish North Sea: displacement history and salt kinematics: Journal of Structural Geology, v. 14, no.5, p. 565-577.

Prosser, S., 1993, Rift-related linked depositional systems and their seismic expressions, *in* Williams G. and A. Dobb eds. Tectonics and Seismic Sequence Stratigraphy: Geological Society, London, Special Publications, v.71, p.35-66.

Richardson, N. J., J. R. Underhill and G. Lewis,2005, The role of evaporite mobility in modifying subsidence patterns during normal fault growth and linkage, Halten Terrace, Mid-Norway: Basin Research, v.17, p.203-223.

Rowan, M.G., 1993, A systematic technique for the sequential restoration of salt structures: Tectonophysics, v.228, p.331-348.

Skogseid, J. T. Pedersen and V.B. Larsen, 1992, Vøring Basin: subsidence and tectonic evolution *in* R.M. Larsen, H. Brekke, B.T. Larsen and E. Telleraas eds. Structural and tectonic modeling and its application to petroleum geology, NPF Special Publication 1, p.55-82.

ter Voorde, M., R. Ravnås, R. Færseth and S. Cloetingh, 1997, Tectonic modeling of the Middle Jurassic synrift stratigraphy in the Oseberg-Brage area, northern Viking Graben: Basin Research, v.9, p.133-150.

Vendeville, B. C., G. Hongxing and M. P. A. Jackson, 1995, Scale models of salt tectonics during basement-involved extension: Petroleum Geoscience, v.1, p.179-183.

Withjack, M. O., K. E. Meisling, L. R. Russel, 1989, Forced folding and basement-detached normal faulting in the Haltenbanken area, offshore Norway: AAPG Memoir, v.46, p.567-575.

Withjack, M. O., J. Olson, and E. Peterson, 1990, Experimental models of extensional forced folds: AAPG Bulletin, v.74, no.7, p.1038-1054.

Withjack, M. O. and S. Callaway, 2000, Active normal faulting beneath a salt layer: An experimental study of deformation patterns in the cover sequence: AAPG Bulletin, v.84, no.5, p.627-651.

Ziegler, P.A. and B. Van Hoorn, 1990, Evolution of the Northe Sea rift system, *in* A. J. Tankard and H.R. Balkwill eds. Extensional Tectonics and Stratigraphy of the North Atlantic Margins: AAPG Memoir 46, p.471-500.

CHAPTER 5
CONCLUSIONS

The experimental models have helped to understand the map patterns of the deformation zones and secondary faults in the cover units associated with the normal movement on basement faults in rift settings. The effect of obliquity of the basement fault with respect to the direction of extension was also studied in detail. The choice of stiff clay over steel ramps in the two layered experimental models helped to understand the extensional deformation both in the basement and in the cover units and also study the effect of lateral propagation and different degrees of interaction of the basement fault.

The overall trend of the deformation zone in the cover unit broadly mimics the trend of the basement fault and its width increases with increasing extension. The secondary faults within the deformation zone have a complex pattern depending on the degree of lateral propagation and obliquity of the basement fault with respect to the direction of extension. For throughgoing faults, fault densities show an initial sharp increase with the initiation of extension and then remain approximately constant or even decrease with further extension. In case of initially terminating faults propagating laterally under extension, fault densities show discrete highs with increasing extension. For multiple basement faults complex structures develop at the areas of interaction of the deformation zones within the cover units. For trapdoor structures involving two connected or approaching basement faults both oblique to the direction of extension, the area of intersection of the associated oblique deformation zones is marked by development of secondary faults trending approximately normal to the direction of

extension. In other cases of basement fault interactions where both the faults are orthogonal to the direction of extension and offset with respect to each other, the interaction of the deformation zones results in an oblique saddle shaped high with the development of oblique secondary faults. The width of the deformation zones (drape folds) restricts the width of the oblique saddle shaped high (the transfer zone), a scenario not considered in the existing conceptual or physical models of transfer zones.

In the case study from offshore Mid-Norway some of the structures modeled experimentally like trapdoor structures, synthetic transfer zones and extensional fault propagation folding have been documented. The study has also shown the role of salt in the partitioning of extensional deformation in the basement and the cover units. During the initial stages of rifting when the rate of extension was presumably low the salt layer decoupled the extension above and below it. An earlier phase of movement on the basement-involved faults helped to localize the large displacement basement-detached listric faults. During a later stage of rifting when the rate of extension was high, the role of salt as an agent for partitioning the extensional was undermined. Faults in the basement were connected to the faults in the cover units under higher amount and rate of displacement of the basement faults in this stage.